Spring 1-1-2016

Investigation of Quasi-Static Electric Fields and Coupled Plasma Populations in the Inner Magnetosphere

Sam Tindal Califf
University of Colorado at Boulder, califf@colorado.edu

Recommended Citation

Califf, Sam Tindal, "Investigation of Quasi-Static Electric Fields and Coupled Plasma Populations in the Inner Magnetosphere" (2016). *Aerospace Engineering Sciences Graduate Theses & Dissertations*. 153.
https://scholar.colorado.edu/asen_gradetds/153

Investigation of Quasi-static Electric Fields and Coupled Plasma Populations in the Inner Magnetosphere

by

Samuel Tindal Califf

B.S., University of Colorado, 2005

M.S., University of Colorado, 2008

A thesis submitted to the
Faculty of the Graduate School of the
University of Colorado in partial fulfillment
of the requirement for the degree of
Doctor of Philosophy
Department of Aerospace Engineering Sciences
2016

This thesis entitled:

Investigation of Quasi-static Electric Fields and Coupled Plasma Populations in the Inner Magnetosphere
written by Samuel Tindal Califf

has been approved for the Department of Aerospace Engineering Sciences

Prof. Xinlin Li

Prof. Robert Ergun

Prof. Howard Singer

Dr. David Malaspina

Prof. Zoltan Sternovsky

Date: November 7, 2016

The final copy of this thesis has been examined by the signatories, and we
find that both the content and the form meet acceptable presentation standards
of scholarly work in the above mentioned discipline.

Califf, Samuel Tindal (Ph.D. Aerospace Engineering Sciences)

Investigation of Quasi-static Electric Fields and Coupled Plasma Populations in the Inner Magnetosphere

Thesis directed by Professor Xinlin Li

Electric fields are a critical component to understanding the dynamics of plasma in the Earth's magnetosphere – large-scale electric fields control the shape of the low-energy (~1 eV) plasmasphere, they are responsible for transporting plasma sheet particles (~keV) into the inner magnetosphere, forming much of the trapped energetic particle population, and they affect the high-energy radiation belts (100s keV to MeV) both directly and through coupled interactions with the lower-energy populations. This dissertation focuses on in situ electric field measurements and particle dynamics in the inner magnetosphere with an emphasis on the most inner region below ~4 R_E in the equatorial plane, where extensive particle and fields observations have only recently been available through the Time History of Events and Macroscale Interactions during Substorms (THEMIS) and the Van Allen Probes missions. We address the measurement of electric fields using double-probe instruments onboard spacecraft, including some of the unique challenges for making accurate measurements in the inner magnetosphere. Next, we explore the average structure of the quasi-static electric field in the inner magnetosphere using many years of in situ measurements near the equatorial plane from THEMIS. These results reveal a spatially structured electric field with stronger electric fields in the dusk sector, which we connect to a magnetopshere-iononsphere coupling mechanism through a detailed event study. Finally, we relate electric field measurements deep within the inner magnetosphere to 100s keV electron enhancements in the slot region.

Dedication

This dissertation is dedicated to Tindal and June.

Acknowledgements

I would like to thank my advisor Xinlin Li for encouraging me to pursue a PhD over 10 years ago when I was an undergraduate, and for supporting me when I decided to come back to graduate school many years later. He has provided just enough direction to initiate my work, and then has given me complete freedom to follow my interests. I would also like to thank the many graduate students, postdocs, and early career scientists for helping shape my understanding of the field through engaging discussions, and for their camaraderie through the struggles and joys of graduate school and scientific research. Specifically, Lauren Blum, Quintin Schiller and Hong Zhao have been excellent academic colleagues, and have paved the path for me to succeed. Finally, I want to thank my wife, China, for sticking with me through the processes, and my children, Tindal and June, for making every day exciting.

Table of Contents

List of Figures

Chapter 1: Introduction

The Earth's magnetosphere is a highly dynamic environment that is driven by solar activity. Charged particles trapped within the magnetosphere respond to variations in the electric and magnetic fields over a wide range of spatial and temporal scales, creating a complex system response that is not fully understood. Modern society is increasingly dependent on space-based technologies for navigation, communication, and security, and these assets can be adversely affected, or even disabled, by energetic particles in the magnetosphere. The impact of geomagnetic activity extends far beyond spacecraft – changes in ionospheric conductivity can affect communication for commercial flights over the poles and navigation for modern farming equipment, and geomagnetically induced currents can damage the power grid, potentially causing blackouts for millions of people. Understanding and ultimately predicting the behavior of the magnetosphere has practical applications today, and it will only become more important in the future.

There are many unanswered questions surrounding the dynamics of energetic particles, the mechanisms that energize them, and even the basic structure and evolution of electric and magnetic fields in the magnetosphere. This thesis focuses on electric fields in the inner magnetosphere and their influence on a range of particle populations. Electric fields allow particles trapped in the Earth's magnetic field to move across magnetic field lines, and they are necessary for energizing charged particles in the magnetosphere. Recent measurements by Time History of Events and Macroscale Interactions during Substorms (THEMIS) and the Van Allen Probes have enabled us to explore the inner magnetosphere at an unprecedented level of detail through advances in instrumentation and extended sampling across all local times.

In Chapter 2, we review the relevant regions of the inner magnetosphere and the basic processes that govern the dynamics. We discuss coupling between the plasmasphere, plasma sheet, ring current and radiation belts that creates complex behavior during periods of geomagnetic activity. The basic types of motion for charged particles under the influence of electric and magnetic fields are introduced, including the guiding-center approximation and particle tracing simulations. Finally, we cover the types of transport, source and loss mechanisms that control the radiation belts.

Chapter 3 focuses on measuring electric fields with double-probe instruments onboard spacecraft. There are several types of uncertainties that cause accurate measurement of DC electric fields to be very challenging, especially in the inner magnetosphere. The boom-shorting factor, coupled with the subtraction of large induced electric fields created by spacecraft motion in the Earth's magnetic field, presents one of the most significant sources of error in the innermost region of the magnetosphere. We estimate the shorting factor for the THEMIS double probe using an empirical technique and compare the results to several analytical and computer-based modeling approaches, revealing a significant discrepancy between the expected and actual behavior of the instrument.

In Chapter 4 we cover the average characteristics of the large-scale electric field in the inner magnetosphere. The Combined Release and Radiation Effects Satellite (CRRES) mission showed that the large-scale electric field is enhanced inside 3-4 R_E during active times, in contrast to the conventional picture that the convection electric field is shielded in the inner magnetosphere. CRRES had limited local time coverage and mostly sampled the dusk side, so we revisit these results using multiple years of THEMIS data that span all local times. The in situ measurements near the equatorial plane from THEMIS reveal that the electric field in the inner magnetosphere is spatially structured, with stronger electric fields in the dusk sector. The THEMIS data also provide further evidence of enhanced electric fields near Earth during geomagnetic storms, indicating that the innermost region of the magnetosphere is more dynamic than conventional models suggest.

We investigate the cause of strong electric fields near dusk in Chapter 5. Particle and fields measurements from the Van Allen Probes demonstrate that the separation between plasma sheet ions and electrons can lead to enhanced electric fields through a coupling mechanism between the magnetosphere and the ionosphere. Low-altitude, high-inclination measurements from DMSP show similar particle boundaries and field-aligned current structures as those observed by the Van Allen Probes near the equatorial plane, highlighting the connection between these vastly separated regions in space.

In Chapter 6, we connect electric field measurements to 100s keV electron enhancements deep within the inner magnetosphere. We model the electron phase space density evolution under the influence of a uniform convection electric field with magnitudes similar to the in situ measurements near 3 R_E in the equatorial plane. This study shows that 100s keV electron enhancements in the slot region can be explained by radial transport, and it provides direct evidence of the electric fields required transport the electrons.

Finally, we summarize this work and offer ideas for future research in Chapter 7.

Chapter 2: Background

2.1 Magnetosphere Overview

The Earth's magnetosphere occupies the region in space defined by the approximately dipolar magnetic field originating from inside the Earth. The solar wind compresses the magnetic field on the dayside, and stretches it into a tail-like configuration on the night side. Magnetic field lines near the Earth's poles are "open" and connected to the solar wind, and at lower latitudes the field lines are "closed", meaning that each end of the field line can be traced to a point on the surface of the Earth. The term "L shell" will be used throughout this work to describe the radial distance in Earth radii (R_E) to a magnetic field line at the magnetic equator. This dissertation focuses on electric fields and particle dynamics in the inner magnetosphere, which encompasses the region of closed magnetic field lines at radial distances of up to ~8 R_E in the equatorial plane ($L < 8$).

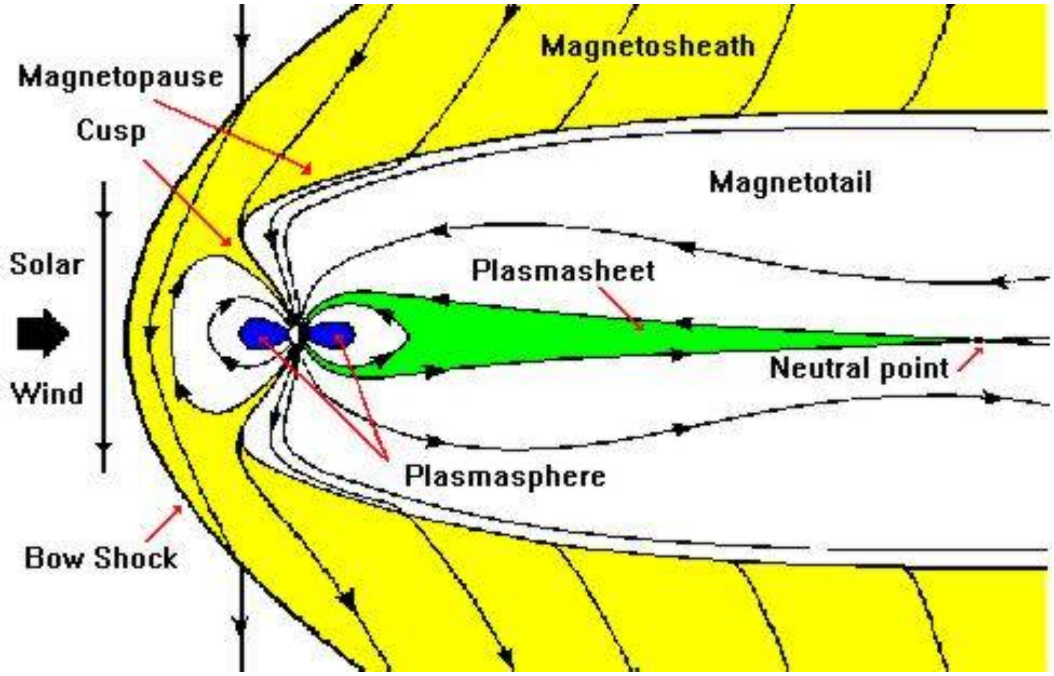

Figure 2.1: Diagram of the Earth's magnetosphere [CCMC website].

There are several distinct plasma populations within the inner magnetosphere that can be differentiated based on characteristic energy and location. The plasmasphere is composed of cold (~1 eV), dense (10s to 1000s cc) plasma that typically extends from the ionosphere (100s km altitude) to ~4-6 R_E in the equatorial plane [e.g., Sandel et al., 2003]. Plasmaspheric plasma originates from the ionosphere and slowly flows up magnetic field lines to fill flux tubes surrounding the Earth, and during quiet times the plasmasphere roughly co-rotates with the Earth. During geomagnetically active times, the outer region of the plasmasphere can be convected away by large-scale electric fields, creating a sharp radial density gradient known as the plasmapause. The outer edge of the plasmasphere often produces a plume that is detached from the main plasmasphere. Figure 2.2 shows plasmasphere erosion and the formation of a plasmaspheric plume from the Imager for Magnetopause-to-Aurora Global Exploration (IMAGE) spacecraft.

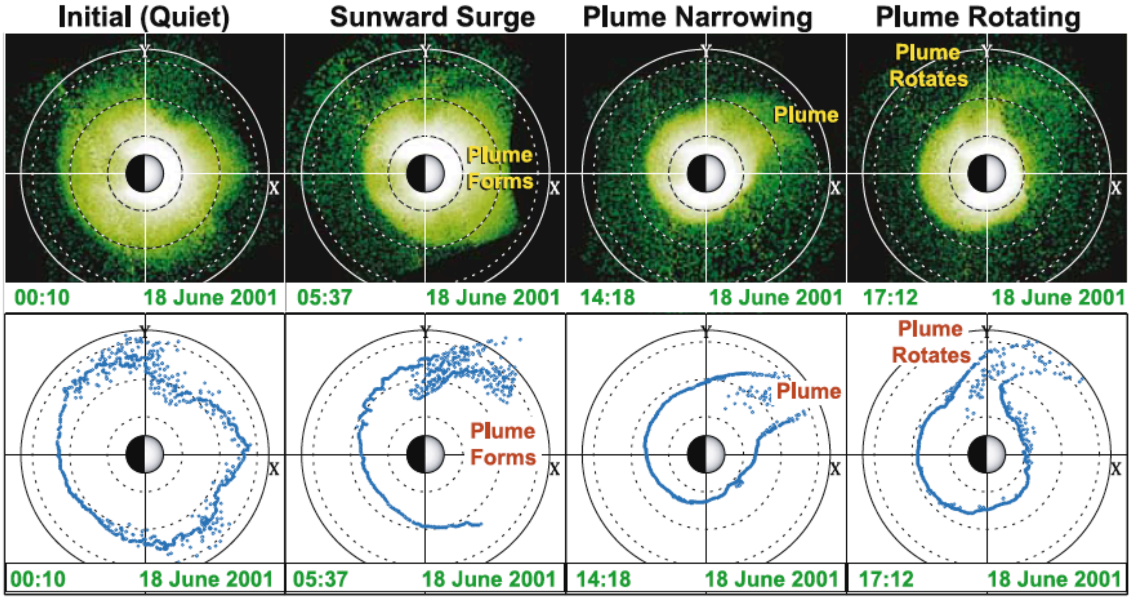

Figure 2.2: Evolution of the plasmasphere during a geomagnetic storm from the IMAGE spacecraft [Figure 5, Darrouzet et al., 2009].

The plasma sheet is defined by particles with energies from 100s eV to 10s keV that originate from both the Earth's ionosphere and the solar wind. The plasma sheet is mainly located on the night side, with the inner edge approximately coinciding with the outer edge of the dipolar region of the Earth's magnetic field. During geomagnetic storms and substorms, plasma sheet particles are transported earthward from the tail into the inner magnetosphere and contribute to the trapped energetic ring current and radiation belt populations. An enhanced ring current is a defining feature of geomagnetic storms, and it is generated by oppositely drifting electrons and ions, creating a net westward current that causes a global depression of the Earth's magnetic field [e.g., Daglis et al., 1999]. The peak ring current pressure is usually located near ~4 R_E in the equatorial plane, and the majority of the pressure is contributed by ions.

Particles with energies from 100s keV to MeV are considered to be part of the radiation belts, which are divided into an inner and outer belt. The inner belt is a fairly stable region located inside of ~2.5 R_E in the equatorial plane and is composed mostly of high-energy protons that are generated through cosmic ray albedo neutron decay (CRAND) and trapping of solar protons [e.g., Selesnick et al., 2014]. The inner radiation belt also contains 100s keV electrons, but it does not typically have a significant MeV electron population except in response to very large geomagnetic storms [e.g., Li et al., 2015]. The outer radiation belt is a much more dynamic region characterized by high-energy (100s keV to MeV) electrons located between ~4-7 R_E, and between the inner and outer belts, there is a slot region that is typically devoid of high-energy electrons. During active times, the slot region is often temporarily filled by enhancements of 100s keV electrons, but slow loss due to interactions between the electrons and the low-energy plasmasphere cause the slot region to be reestablished within a few days [e.g., Lyons and Thorne, 1973].

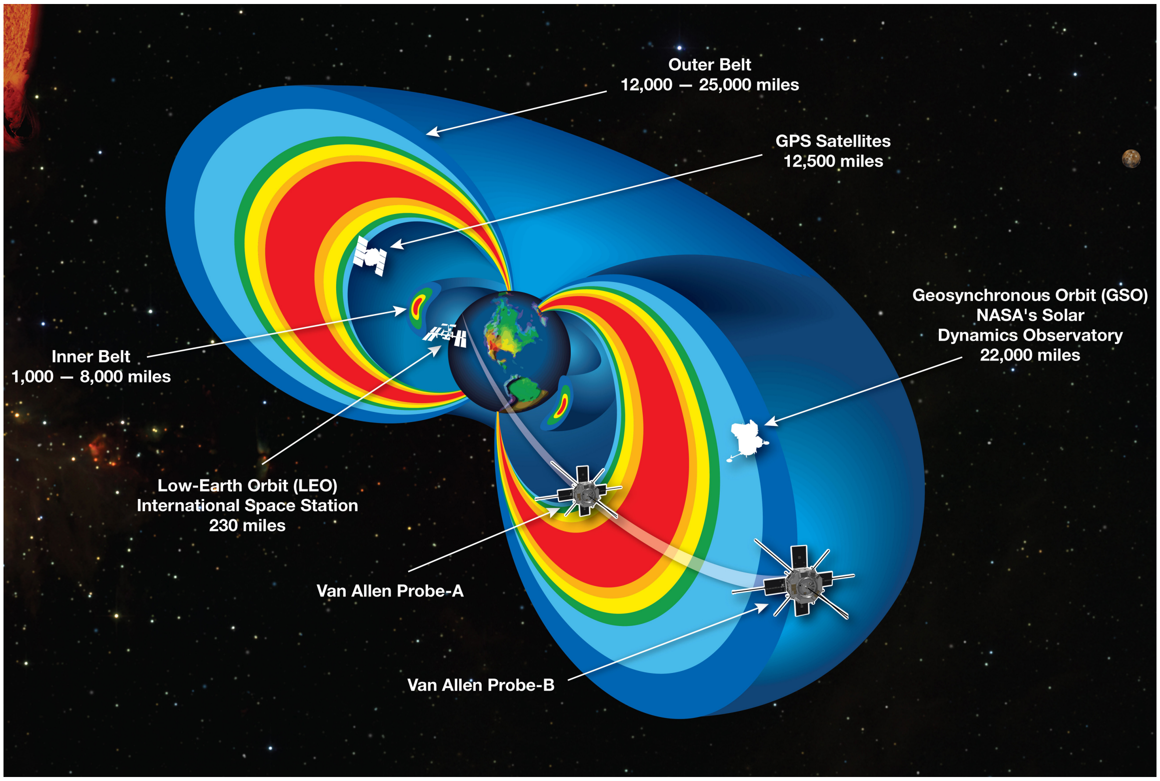

Figure 2.3: Schematic of the Earth's radiation belts [Van Allen Probes website].

2.2 Geomagnetic Storms and Substorms

Variations in the inner magnetosphere are largely driven by solar activity, with southward pointing interplanetary magnetic field (IMF) being an important factor for determining the coupling between the solar wind and the magnetosphere – southward IMF creates a more favorable condition for magnetic reconnection at the dayside magnetopause where the Earth's magnetic field points northward. Coronal mass ejections (CME) and co-rotating interaction regions (CIR) are the two main types of solar wind structures that lead to geomagnetic activity [e.g., Zhang et al., 2007]. CMEs consist of massive eruptions of plasma from the Sun that impact the magnetosphere and are often accompanied by sharp increases in dynamic pressure and a slow turning of the IMF. CIRs are characterized by high solar wind speed lasting up to several days, and they are features that co-rotate with the Sun on a 27-day period.

Geomagnetic storms are events that may last for many hours or days, and one of the defining features is a global depression of the magnetic field due to an enhanced ring current. Figure 2.4 shows solar wind measurements and geomagnetic indices for the 17 March 2013 geomagnetic storm. A CME impacted the magnetosphere at 06 UT on 17 March 2013, and there was variation in the IMF (panel a) and an increase in solar wind speed (panel b) and pressure (panel c). The Dst index (panel e), which is derived from ground magnetometer measurements of the horizontal deflection in the magnetic field, is often used to identify geomagnetic storms. The initial increase in Dst at 06 UT on 17 March 2013 is the sudden commencement, and the gradual decrease in Dst until 21 UT is the main phase of the storm. The decrease in Dst reflects a global depression of the magnetic field, and it is associated with enhanced convection caused by the southward IMF (negative Bz in panel a). After the IMF turns northward near 21 UT, the slow recovery phase begins and Dst gradually increases toward pre-storm levels.

Substorms are shorter events lasting for hours that often occur during geomagnetic storms, but can also occur without a storm. During substorms, the stretched magnetic field lines in the magnetotail reconnect, causing the magnetic field to snap back to a more dipolar configuration. The dipolarization of the magnetic field injects plasma sheet particles into the inner magnetosphere. The auroral electroject (AE) index (Figure 2.4d), which is derived from variations in the horizontal component of the magnetic field measured by ground magnetometers, is an indicator of substorm activity.

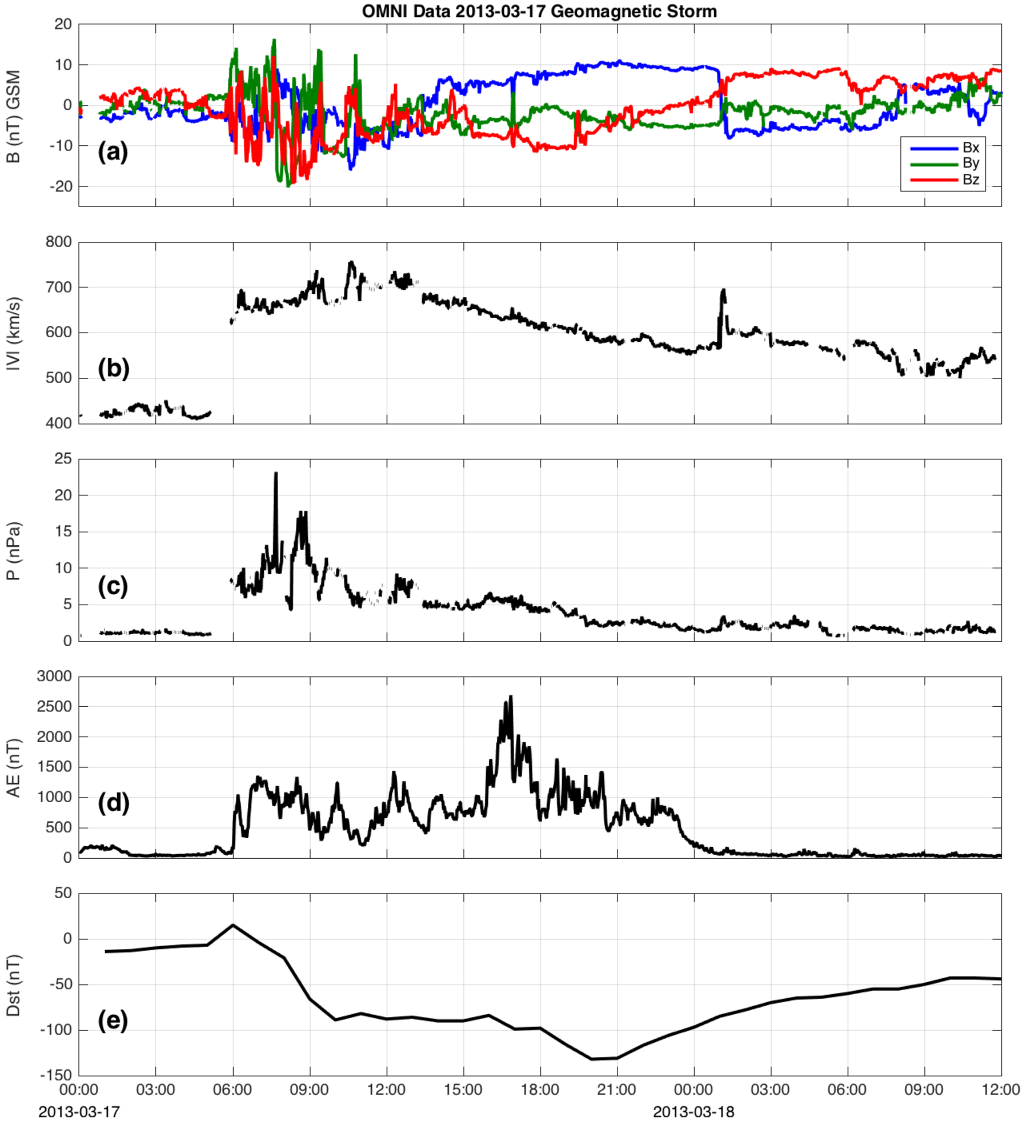

Figure 2.4: Solar wind and geomagnetic indices for the 17 March 2013 geomagnetic storm. (a) IMF in geocentric solar magnetic (GSM) coordinates, (b) solar wind speed, (c) solar wind dynamic pressure, (d) AE index, and (e) Dst index.

2.3 Electric Fields in the Inner Magnetosphere

The large-scale electric field in the inner magnetosphere is generally described by the superposition of a dawn-to-dusk convection electric field and a radially inward pointing co-rotation electric field. The convection electric field is generated by the interaction of the solar wind with the Earth's magnetic field, where magnetic reconnection at the dayside magnetopause allows the solar wind to drag magnetic field lines over the polar cap from the day side to the night side [Dungey, 1961]. There is a "frozen-in" electric field in the solar wind given by

$$\boldsymbol{E} = -\boldsymbol{v}x\boldsymbol{B}$$

(Eq. 2.1)

where $\boldsymbol{v}$ is the solar wind velocity and $\boldsymbol{B}$ is the interplanetary magnetic field. The solar wind speed is typically ~400 km/s, and the IMF strength is ~5 nT. Assuming a southward IMF and anti-sunward flow, the frozen-in electric field would be 2 mV/m pointing from dawn to dusk. This electric field maps along magnetic field lines to the polar cap, creating a large-scale potential drop in the magnetosphere from dawn to dusk. The typical quiet-time convection electric field is ~0.2 mV/m, so only a fraction of the solar wind electric field reaches the inner magnetosphere.

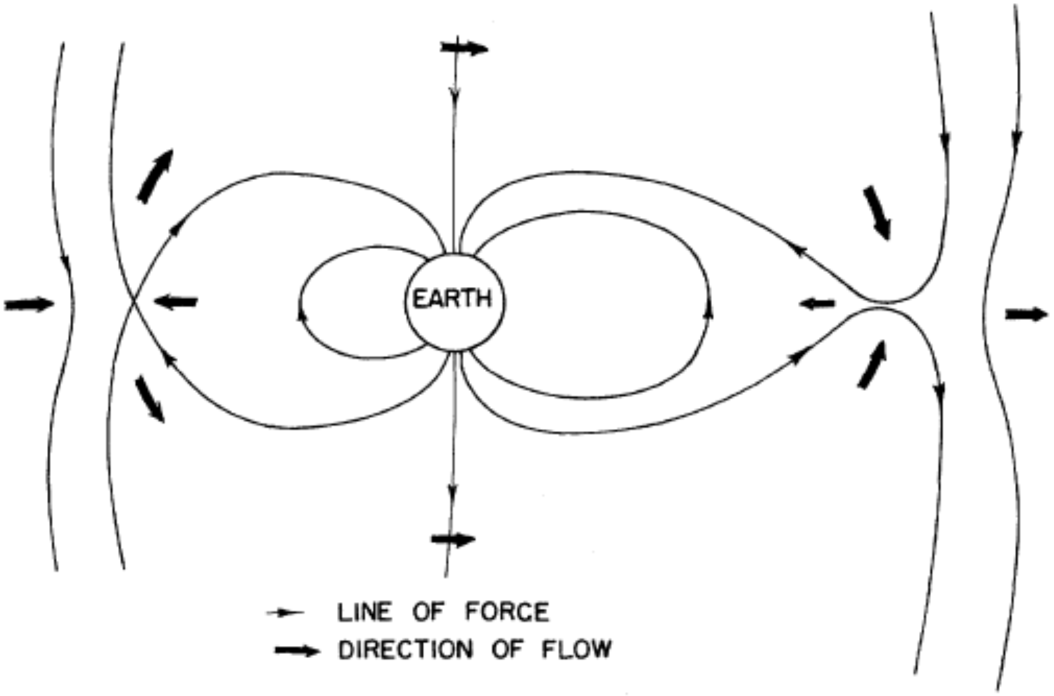

Figure 2.5: Dungey cycle [Figure 1, Dungey, 1961].

The co-rotation electric field is created by viscous interaction between the ionosphere and the upper neutral atmosphere, which co-rotates with Earth. The co-rotation electric field can be calculated by

$$\boldsymbol{E}_{\boldsymbol{corot}} = -(\boldsymbol{\omega}_{\boldsymbol{E}} \times \boldsymbol{R}) \times \boldsymbol{B}$$

(Eq. 2.2)

where $\boldsymbol{\omega}_{\boldsymbol{E}}$ is the angular rotation rate of the Earth, $\boldsymbol{R}$ is the position vector and $\boldsymbol{B}$ is the local magnetic field. In the equatorial plane, Eq. 2.2 can be approximated by

$$E_{corot} \cong \frac{14}{R^2}\left(\frac{mV}{m}\right)$$

(Eq. 2.3)

where R is radial distance in Earth radii.

The co-rotation electric field decreases in magnitude with radial distance, and beyond a certain distance the convection electric field becomes dominant. The balance between co-rotation and convection forms a separatrix – inside the separatrix plasma is mostly co-rotating with Earth, and outside of the separatrix plasma is flowing sunward from the tail to the day side. The inner co-rotating region generally corresponds to the plasmasphere and usually extends to ~4-6 R_E, although during periods of strong convection the plasmapause can move inside of 2 R_E.

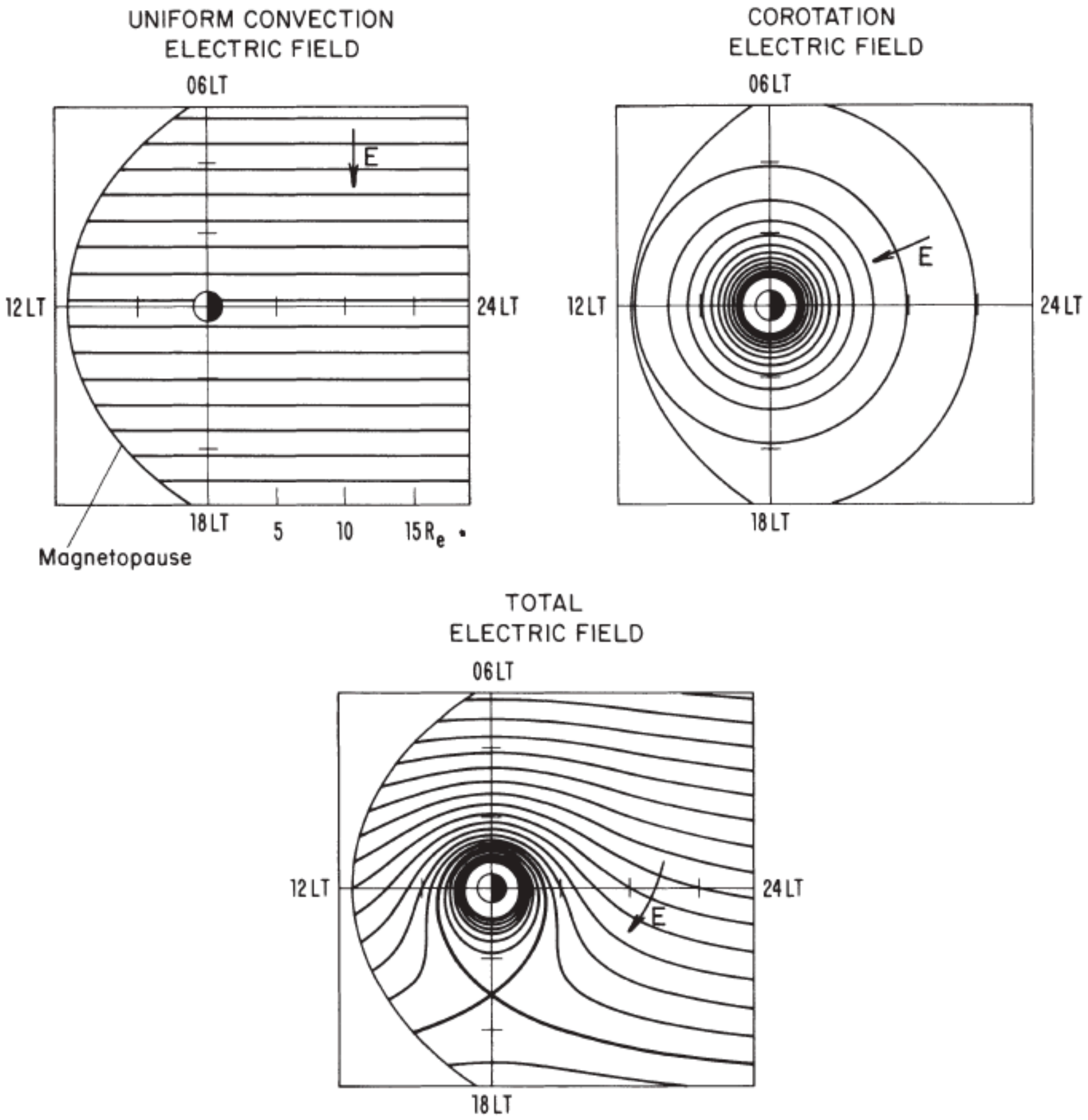

Figure 2.6: Diagram of potential contours for a (a) uniform convection electric field, (b) co-rotation electric field, and (c) combined convection and co-rotation [Figure 2.2, Lyons and Williams, 1984].

This simplified picture of convection and uniform co-rotation represents the standard description of large-scale electric fields in the inner magnetosphere. One aspect of this thesis is to explore the actual structure of the large-scale electric field using in situ measurements near the equatorial plane (Chapter 4).

In addition to convection and co-rotation, there are many other mechanisms that generate electric fields in the inner magnetosphere. Ultra-low frequency (ULF) waves (1 mHz to 1 Hz) are oscillations associated with fundamental modes of the magnetic field, and they play an important role in radiation belt electron dynamics through drift-resonant interactions [e.g., Elkington et al., 2003]. Earthward-propagating dipolarization fronts associated with substorms carry azimuthal electric fields as the magnetic field strength increases [e.g., Sarris et al., 2002], and interplanetary shocks can create similar azimuthal electric fields through global compression of the magnetosphere [e.g., Li et al., 1993]. Field-aligned currents connecting the magnetosphere and the ionosphere can also generate strong electric fields associated with subauroral polarization streams (SAPS) [e.g., Foster and Vo, 2002] and subauroral ion drifts (SAID) [e.g., Anderson et al., 2002]. SAPS will be addressed in more detail in Chapter 5.

Plasma instabilities can also generate higher frequency waves. Pitch angle anisotropies in ions can lead to electromagnetic ion cyclotron waves (EMIC) that resonate near the ion gyro frequency (~0.1-10 Hz). EMIC waves propagate efficiently in the presence of cold, dense plasma, and they are often observed near the overlap of the ring current ions and the plasmapause. Ion pitch angle anisotropies can also create magnetosonic waves (~100s Hz) both inside and outside of the plasmasphere. Similarly, electron pitch angle anisotropies can generate very low frequency (VLF) whistler-mode chorus waves (~10s kHz), however, chorus waves propagate more efficiently in lower-density regions outside of the plasmasphere. Chorus has been suggested to be the source of plasmaspheric hiss, which is characterized by broadband waves (~0.1-1 kHz) inside the plasmasphere [Bortnik et al., 2008].

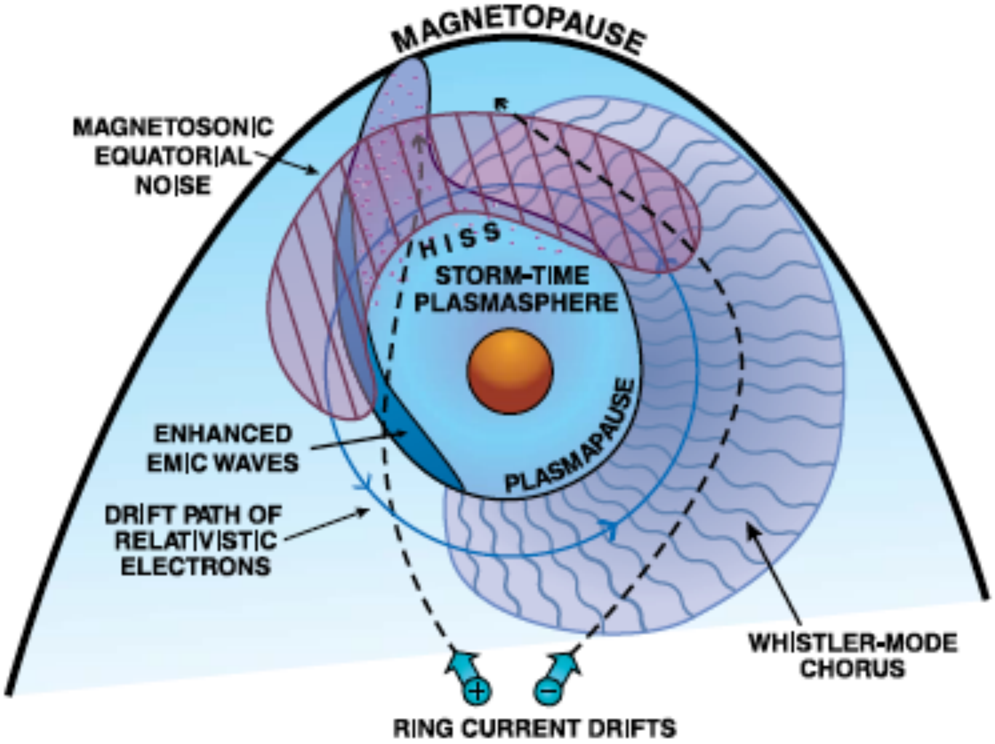

Figure 2.7: Diagram of waves in the inner magnetosphere [Figure 1,Thorne, 2010].

2.4 Charged Particle Motion

The dynamics of a charged particle under the influence of an electric and magnetic field are governed by the Lorentz force equation

$$\boldsymbol{F} = q(\boldsymbol{E} + \boldsymbol{v} \times \boldsymbol{B})$$

(Eq. 2.4)

where q is the charge, $\boldsymbol{E}$ is the electric field, $\boldsymbol{v}$ is the particle velocity, and $\boldsymbol{B}$ is the magnetic field. In order to change the energy of a particle, a force must be applied in the direction of the particle's velocity. The magnetic field can only exert a force perpendicular to the velocity, so electric fields are required to energize charged particles.

2.4.1 Adiabatic Invariants

The Lorentz equation (Eq. 2.4) leads to three characteristic types of motion for a charged particle trapped in the Earth's roughly dipolar magnetic field: gyration about the magnetic field line, bounce along the magnetic field line between mirror points, and drift azimuthally about the Earth. Each type of motion has an associated adiabatic invariant that is conserved if the magnetic and electric fields change on slower temporal and longer spatial scales than the characteristic motion related to the invariant. The first invariant, μ, is related to the gyro motion about the field line.

$$\mu = \frac{{p_\perp}^2}{2m_0 B}$$

(Eq. 2.5)

$p_\perp$ is the perpendicular component of momentum, m_0 is the rest mass, and B is the magnetic field strength.

In a dipole magnetic field, the field strength increases along the field line at higher latitudes and reflects particles back toward the magnetic equator. The location at which the particle reverses motion along the field line is called the mirror point. The second invariant, I, is related to the bounce motion along the field line.

$$I = \int_{s_m}^{s'_m} \left(1 - \frac{B(s)}{B_m}\right)^{\frac{1}{2}} ds$$

(Eq. 2.6)

B_m is the field strength at the magnetic equator, and the integral is taken along the magnetic field line between mirror points. The second invariant is often expressed as

$$K = \frac{J}{2\sqrt{2m_0\mu}} = I\sqrt{B_m} = \int_{s_m}^{s_m'} \left(B_m - B(s)\right)^{\frac{1}{2}} ds$$

(Eq. 2.7)

The third invariant, Φ, is the flux enclosed by the drift shell of the particle.

$$\Phi = \int B\, dS$$

(Eq. 2.8)

The third invariant is often rewritten in terms of L^*, which has the physical interpretation of the radial distance to the field line at the magnetic equator.

$$L^* = -\frac{2\pi k_0}{\Phi R_E}$$

(Eq. 2.9)

k_0 is the Earth's dipole moment and R_E is the radius of the Earth.

2.4.2 Guiding-center Approximation

Given that the gyro period of an electron is ~10^{-5} seconds, and that we are often interested in dynamics due to much slower changes in the electric and magnetic fields (~minutes), it is useful to average the equations over a gyro period. There are several types of drift terms that describe the average motion of the electron under different electric and magnetic field configurations. The azimuthal drift around the Earth is caused primarily by the gradient in the magnetic field, which varies as ~$1/L^4$ due to the $1/L^3$ dependence of the equatorial magnetic field strength in a dipole.

$$\boldsymbol{v}_{\nabla \boldsymbol{B}} = \frac{K_\perp}{qB} \frac{\boldsymbol{B} \times \nabla \boldsymbol{B}}{B^2}$$

(Eq. 2.10)

$K_\perp$ is the perpendicular kinetic energy. Curvature of the magnetic field line also contributes to azimuthal drift by

$$\boldsymbol{v_{curv}} = \frac{2K_\parallel}{qB}\frac{\boldsymbol{R_c}\times\boldsymbol{B}}{{R_c}^2 B}$$

(Eq. 2.11)

where $K_\parallel$ is the parallel kinetic energy, and $\boldsymbol{R_c}$ is the radius of curvature of the magnetic field line. The charge dependence of the gradient and curvature drifts causes electrons to drift eastward and ions to drift westward. Equatorially mirroring particles do not experience curvature drift because they have no velocity parallel to the magnetic field.

An electric field causes a drift perpendicular to both the electric and magnetic fields.

$$\boldsymbol{v_{E\times B}} = \frac{\boldsymbol{E}\times\boldsymbol{B}}{B^2}$$

(Eq. 2.12)

Combining Eq. 2.10-2.12 and substituting the definitions for kinetic energy and radius of curvature results in the guiding-center approximation for motion perpendicular to the magnetic field line.

$$\boldsymbol{v_{GC}} = \frac{\gamma m v^2}{2qB^2}\left(1 + \frac{{v_\parallel}^2}{v^2}\right)\hat{\boldsymbol{b}}\times\boldsymbol{\nabla B} + \frac{\boldsymbol{E}\times\boldsymbol{B}}{B^2}$$

(Eq. 2.13)

γ is the relativistic factor given by

$$\gamma = \frac{1}{\sqrt{1 - \frac{v^2}{c^2}}}$$

(Eq. 2.14)

where c is the speed of light. The bounce motion of the guiding center along the magnetic field line is given by

$$\frac{dv_{\parallel}}{dt} = -\frac{\mu}{\gamma^2 m}\hat{\boldsymbol{b}} \cdot \nabla \boldsymbol{B}$$

(Eq. 2.15)

One practical application for the guiding-center equations is to model the trajectories of electrons using a particle tracer. In order to integrate the Lorentz force for an electron and accurately capture the gyro motion, integration time steps on the order of 1 μs are required. Using the guiding-center approximation, simulation time steps of 1 second or more are adequate to model electrons. This allows extended simulations for many particles to be run to test the effects of different electric and magnetic field configurations. We use a guiding-center particle tracer in Chapter 6 to study the effect of the convection electron field on 100s keV electrons in the slot region.

2.4.3 Electric Fields and Particle Energization

We stated earlier that electric fields are required to alter the energy of a charged particle because a force must be applied in the direction of the particle's velocity, and magnetic fields can only apply a force perpendicular to the velocity. The combined effect of a gradient in the magnetic field and an electric field on a 90-degree pitch angle proton is shown in Figure 2.8. These results were obtained by directly integrating the Lorentz equation (Eq. 2.4). The gradient in the magnetic field is along the +Y direction, and the electric field is in the –X direction. Without the electric field, the proton drifts (to the left) according to the gradient-B drift (Eq. 2.10), and the energy remains constant. When an electric field is applied perpendicular to the gradient in the magnetic field, the **ExB** drift

(Eq. 2.12) causes the particle to move into a stronger magnetic field. The electric field is in the direction of the net gradient-B drift velocity, which causes the energy to increase. An equivalent interpretation is that the energy increases to conserve the first adiabatic invariant in the stronger magnetic field.

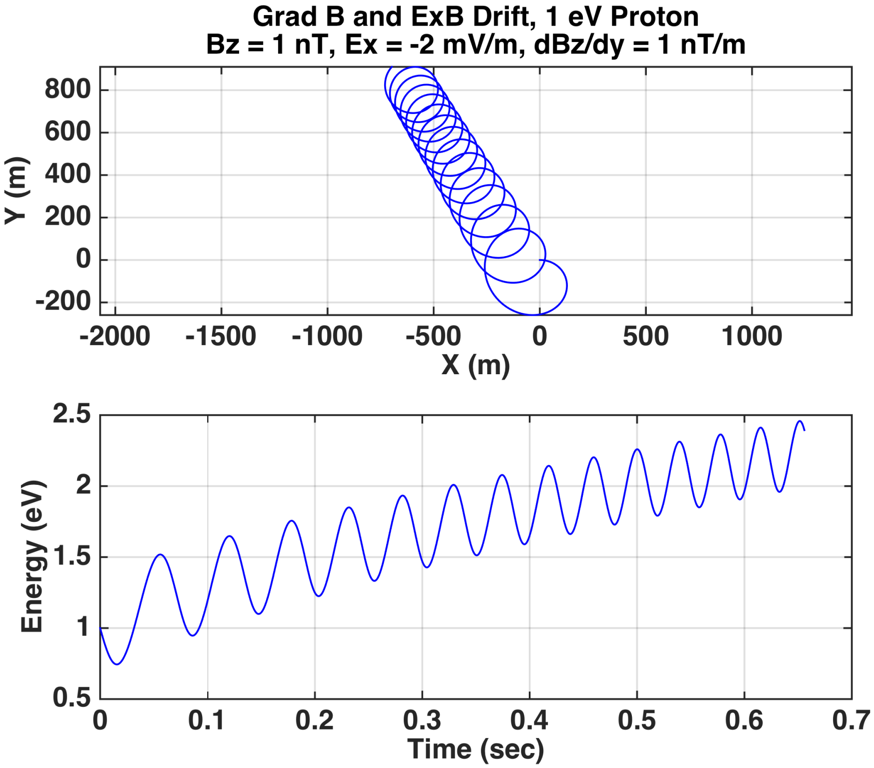

Figure 2.8: The trajectory of a proton under the influence of combined gradient and ExB drifts.

2.5 Radiation Belt Dynamics

Electrons in the outer radiation belt are highly dynamic, often displaying orders of magnitude variations in flux over short intervals during both storm and non-storm periods [e.g., Reeves et al., 2003; Schiller et al., 2014]. The dynamics are typically discussed in terms of competing radial transport, local acceleration and loss mechanisms. Under radial transport, the third adiabatic invariant is broken, but the first two invariants are conserved.

In this scenario, if a particle moves inward to lower L shells, the energy increases in order to conserve μ as the magnetic field strength increases. Likewise, outward transport to larger L shells reduces the energy of the particle. Radial transport can be caused by large-scale electric fields associated with convection, dipolarization fronts, or global compression of the magnetosphere through interplanetary shocks, or by gradual radial diffusion through drift resonance with ULF waves [e.g., Li et al., 1993; Sarris et al., 2002; Elkington et al., 2003].

Local acceleration refers to in situ heating of electrons by high-frequency waves that can break the first and second adiabatic invariants, altering both energy and pitch angle. VLF chorus waves are thought to play a major role in locally accelerating electrons to MeV energies in the outer belt [e.g., Reeves et al., 2013]. Chorus waves are generated by an instability related to pitch angle anisotropy of keV electrons. The chorus acceleration mechanism begins with keV plasma sheet electrons being injected into the inner magnetosphere, and during this process they are preferentially accelerated perpendicular to the magnetic field, setting up the pitch angle anisotropy required to generate the chorus waves. These chorus waves then resonate with higher-energy (~100s keV) electrons, and can accelerate a portion of the electrons to very high energies (> 1 MeV).

Radiation belt losses can be classified into two major categories: precipitation to the atmosphere and magnetopause shadowing. Trapped particles bounce along field lines between magnetic mirror points, with the mirroring altitude determined by the equatorial pitch angle and the ratio of the high-latitude magnetic field strength to the equatorial field strength. If an electron mirrors below ~100 km altitude, the atmospheric density is high enough to cause the electron to collide with neutral particles. This process is precipitation loss, and the equatorial pitch angle below which the particle will be lost is known as the "loss cone". Similar to local acceleration, precipitation loss is associated with wave-particle interactions that alter the energy and pitch angle of the particle. Inside the plasmasphere, VLF hiss waves are known to scatter radiation belt electrons into the loss cone, causing slow precipitation loss [e.g., Lyons and Thorne, 1973]. Also, EMIC waves created by anisotropic keV ion pitch angle distributions can cause rapid pitch angle scattering and loss for MeV electrons [e.g., Blum et al., 2015]. Additionally, the same VLF chorus waves that can energize electrons to MeV energies may also scatter electrons into the loss cone [e.g., Shprits et al., 2008].

Magnetopause shadowing refers to inward motion of the magnetopause that intersects the drift paths of radiation belt electrons. The magnetopause location is determined by a pressure balance between the magnetosphere and the solar wind. During non-storm times, the magnetopause is located near 10 Re, but increased solar wind pressure can cause the magnetopause to move inward to below 6 R_E, allowing previously trapped electrons to escape the inner magnetosphere [e.g., Turner et al., 2014].

In order to differentiate between acceleration and loss mechanisms, radiation belt flux measurements are often converted to phase space densities (PSD) as a function of the adiabatic invariants μ, K and L*. PSD relates to flux by

$$f = \frac{j}{p^2}$$

(Eq. 2.16)

where j is flux and p is the relativistic momentum.

In situ flux measurements by spacecraft are sorted by energy and pitch angle, and variations in the spacecraft location within the magnetic field can lead to apparent changes in flux that may not reflect real changes in the particle distributions. Changes in radial PSD profiles can be used to infer acceleration mechanisms, where local peaks indicate local acceleration [e.g., Green et al., 2004].

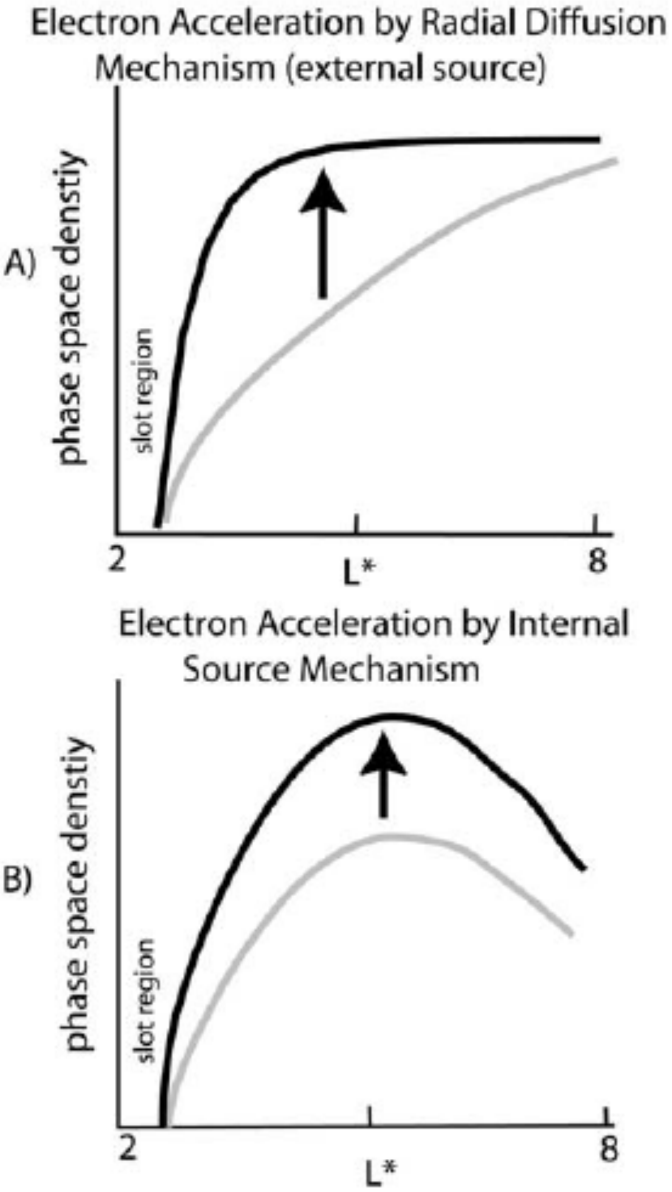

Electron Acceleration by Radial Diffusion Mechanism (external source)

Electron Acceleration by Internal Source Mechanism

Figure 2.9: Schematic of PSD evolution for (a) radial transport and (b) local acceleration [Figure 2, Green et al., 2004].

2.6 Science Questions

There are many open questions surrounding the dynamics of the inner magnetosphere. We will address the following questions in this dissertation:

- **What are the important error sources for measuring electric fields in the inner magnetosphere, and how well do current spacecraft models predict the observed behavior of the double-probe instrument?**
- **What is the average structure of the large-scale electric field in the equatorial magnetosphere, and how does it vary with geomagnetic activity?**
- **What physical processes drive the structure of the electric field in the inner magnetosphere?**
- **How do electric fields at low L shells relate to 100s keV electron dynamics in the slot region?**

Chapter 3: Measuring Electric Fields with Double-probe Instruments

The following chapter is based on work published in Califf and Cully [2016], Empirical estimates and theoretical predictions of the shorting factor for the THEMIS double-probe electric field instrument, J. Geophys. Res. Space Physics, 121, doi:10.1002/2016JA022589.

3.1 Introduction

Quantifying the DC and low-frequency components of the electric field is critical to understanding plasma dynamics in the inner magnetosphere. The large-scale convection electric field plays an important role in transporting plasma sheet particles into the inner magnetosphere, where they form the ring current and radiation belt populations [e.g., Daglis et al., 1999; Jaynes et al., 2015]. Convection and related subauroral polarization streams (SAPS) also drive plasmasphere erosion and plume structures that alter the growth and propagation of higher-frequency waves which are linked to both loss and acceleration of radiation belt electrons [e.g., Goldstein et al., 2003; Thorne et al., 2013]. Additionally, ULF waves are known to accelerate radiation belt electrons through drift resonance [e.g., Hudson et al., 2001], and impulsive electric fields related to interplanetary shocks and substorms can transport and energize electrons deep within the inner magnetosphere [e.g., Li et al., 1993; Sarris et al., 2002].

The THEMIS Electric Field Instrument (EFI) [Bonnell et al., 2008] consists of spherical sensors mounted at the ends of long wire booms in the spacecraft spin plane. There are two pairs of orthogonal spin-plane sensors with tip-to-tip separations of 49.6 m and 40.4 m. There are also two axial sensors on much shorter rigid booms, but this study only addresses the spin-plane measurement. Ideally, the spherical probes couple directly to the plasma potential, and the electric field can be estimated by measuring the potential difference between opposite spheres.

$$E_{12} = -\nabla\phi = \frac{(V_2 - V_1)}{dx}$$

(Eq. 3.1)

V_1 and V_2 are the measured potentials of the spheres relative to the spacecraft potential, and dx is the distance between the spheres.

In reality, the probes arrive at a potential determined by a balance of currents, resulting in an offset between the probe and plasma potentials. The natural currents come from incoming ambient electrons and ions, outgoing photoelectrons, and outgoing backscattered and secondary electrons. Due to the much higher thermal velocity of electrons relative to ions, the ion term can be neglected, and the dominant current sources are incoming ambient electrons and outgoing photoelectrons. The photoelectrons create a sheath around the probe that has an effective resistance between the probe and the plasma. The sheath resistance is approximately V_{ph}/I_e, where V_{ph} is the energy of the escaping photoelectrons, which is on the order of a few volts, and I_e is the ambient electron current to the probe [e.g., Bale et al., 2008].

In order to reduce the effect of the sheath, a negative bias current is applied from the spacecraft to the probe. The bias current balances part of the escaping photoelectron current, and it brings the probe potential closer to the ambient plasma potential. In practice, the bias current is chosen by sweeping through a range of values and finding the minimum probe impedance $\Delta V/\Delta I$. This means that small changes in current have a small effect on the measured potential [e.g., Pedersen et al., 1984]. Given that the sheath resistance is dependent on both the photoelectron characteristics and the ambient plasma, the optimal bias current may vary in different plasma conditions. Also, in the absence of sunlight, there is no photoelectron current to balance the bias current, and the probes saturate to a large negative potential. A large bias current can also affect the spacecraft potential, which can impact low-energy plasma measurements by other instruments onboard. An example of the expected response to a range of bias currents is shown in Figure 3.1.

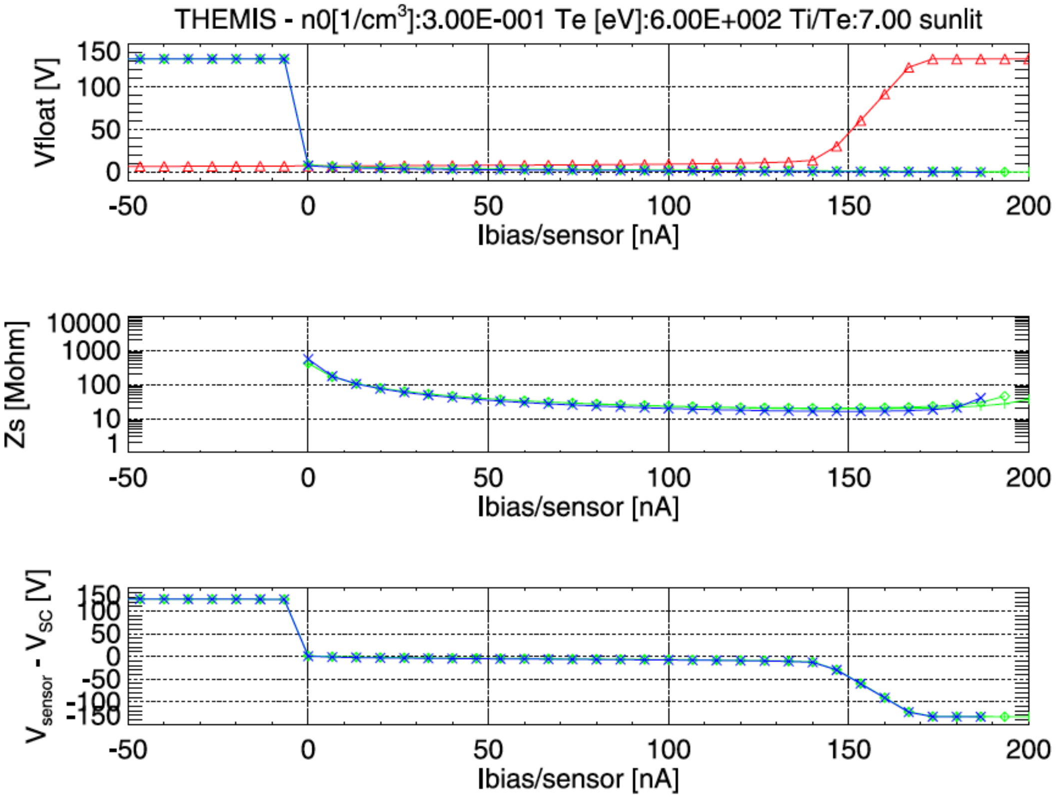

Figure 3.1: Modeled bias sweep for THEMIS EFI [Figure 15, Bonnell et al., 2008]. (a) EFI sensor and spacecraft floating potentials, (b) sheath resistance, and (c) sensor potentials relative to the spacecraft as a function of bias current.

The electric field is inferred through differential potential measurements between opposite probes, so offsets between the probes and plasma do not introduce errors if they are symmetric. This drives the spherical probe design, which has photoemission properties that are independent of sun angle. Also, correctly biasing the probes minimizes the effect of small variations in currents due to the ambient plasma or surface properties on the differential potential between opposite spheres.

The double-probe measurement can also be influenced by photoelectrons being exchanged between surfaces on the spacecraft that are intended to be isolated. For THEMIS, there are biased potential surfaces to mitigate this effect. The outer braid of the long wire booms is connected to the spacecraft potential, and at the preamp, there is an inner surface biased to the guard potential and an outer surface biased to the usher potential. The usher and guard surfaces are typically biased positively by a few volts to prevent photoelectrons from flowing across the preamp between the probe and the wire boom. Figure 3.2 shows the configuration of the EFI instrument for THEMIS.

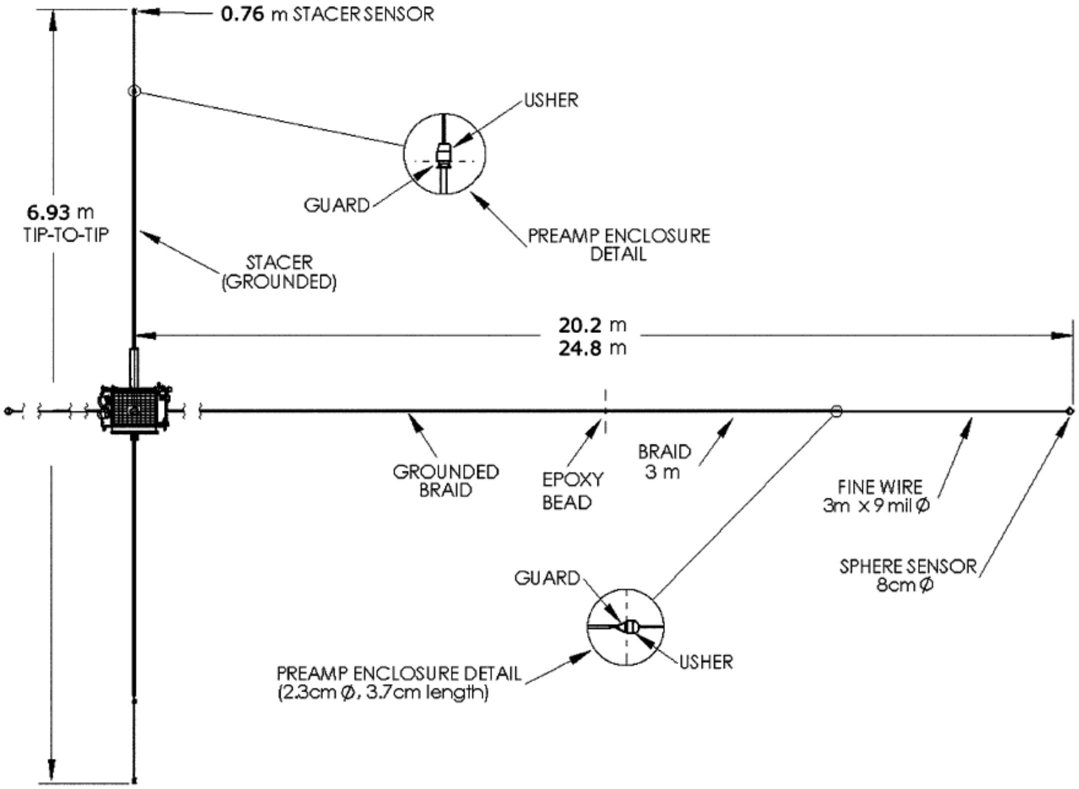

Figure 3.2: THEMIS EFI double-probe diagram [Figure 2, Bonnell et al., 2008].

In addition to measuring the electric field, the double-probe technique provides an estimate of the spacecraft potential through the average of the measured potential of opposite spheres.

$$V_{sc\ est} = -\frac{(V_1 - V_{sc}) + (V_2 - V_{sc})}{2}$$

(Eq. 3.2)

Here the electric field is assumed to be constant over the length of the booms, so the potential of each sphere with respect to the spacecraft is equal and opposite.

There are numerous well-known issues related to extracting the DC component of the electric field using the double-probe technique. Photoelectrons can flow between surfaces that are intended to be electrically isolated, causing an apparent sunward electric field [e.g., Pedersen et al., 1998]. Electrostatic wakes can form in the presence of cold ion flow, altering the potential structure around the spacecraft and introducing real, but unintended electric fields into the measurement [e.g., Engwall et al., 2006]. In the plasma sheet and radiation belts, higher-energy electrons can charge the spacecraft to large potentials and saturate the electric field instrument. This study addresses the boom shorting effect for the THEMIS EFI double-probe instrument, which is a scale factor error on the measurement due to the influence of the nearby wire booms on the potential measured by the spherical sensors.

In addition to instrumentation errors, the motion of the spacecraft with respect to the Earth's magnetic field can be a significant factor in the accuracy of DC electric field measurements. The spacecraft experiences an electric field due to the Lorentz transformation that must be subtracted in order to obtain a measurement in the rest frame of the Earth.

$$\boldsymbol{E} = \boldsymbol{v_{sc}} \times \boldsymbol{B}$$

(Eq. 3.3)

The strength of the spacecraft **vxB** electric field can be much larger than any relevant DC electric field near perigee because both the spacecraft velocity and the magnitude of the Earth's magnetic field are large. The spacecraft velocity and local magnetic field are well known from spacecraft ephemeris and the onboard magnetometer. However, scale factor uncertainties in the electric field measurement can introduce large errors in the **vxB** subtraction, making accurate determination of the shorting factor important for measuring DC electric fields in the inner magnetosphere.

The shorting factor for the ISEE-2 double-probe instrument was estimated by comparing the double-probe electric field to **–vxB** in the solar wind based on ion and magnetic field measurements [Pedersen et al., 1984]. When the long wire booms were connected to the spacecraft potential, the double-probe instrument measured only 70% of the ambient electric field (shorting factor = 0.7). However, when the wire booms were driven to -10 V relative to the spherical sensors, there was no apparent shorting. Pedersen et al. [1984] also note that considerably less shorting was observed for GEOS, which had 43 m tip-to-tip sensor separation, while the ISEE spheres were separated by 73.5 m. A similar estimate was made for Cluster (88 m tip-to-tip separation) by comparing **–vxB** from the ion spectrometer and magnetometer, and the shorting factor was found to be 0.9 [Khotyaintsev et al., 2014]. The authors state that the shorting factor is expected to change in more dense plasmas where the Debye length is small relative to the booms, but they chose to use a constant value because Cluster mostly operates in the long Debye length limit. Orbit-averaged shorting factor estimates from Cluster also show variation from ~0.74-1.0 [Fig. 3, Khotyaintsev et al., 2014], although the authors attribute this to poor data coverage.

The Van Allen Probes (100 m tip-to-tip separation) use a constant shorting factor of 0.947 that is derived by fitting many months of quiet-time perigee data to the expected electric field from spacecraft motion and co-rotation, which is similar to the technique used in this study [Scott Thaller, private communication]. Our study focuses on electric field measurements in the inner magnetosphere where not only is the shorting factor expected to be variable due to the spacecraft passing in and out of the dense plasmasphere, but accurate determination of the shorting factor is also critical because of the large **vxB** from spacecraft motion that must be subtracted from the measurement.

In this study we use multiple years of THEMIS data to derive an empirical shorting factor as a function of spacecraft potential, and then approximate the Debye length from spacecraft potential to show the relationship between shorting and Debye length. Next, we develop a spacecraft simulation to predict the shorting behavior, and then discuss the similarities and differences between the model and empirical data.

3.2 Empirical Shorting Factor Estimate

The shorting factor for THEMIS EFI was previously estimated by comparing the double-probe measurement to the expected frozen-in electric field based on the ion drift velocity and the local magnetic field [Bonnell et al., 2008].

$$\boldsymbol{E} = -\boldsymbol{v_i} \times \boldsymbol{B}$$

(Eq. 3.4)

This calibration was performed while the spacecraft was in the magnetosheath, and a scale factor error of approximately 0.7 was found, indicating that the double-probe instrument underreported the true electric field by ~30%.

In the inner magnetosphere, the spacecraft traverses through a highly variable plasma environment, and the shorting factor is expected to change. Deep inside the plasmasphere, densities can be on the order of 1000 cm^{-3} with a corresponding Debye length of 0.23 m, assuming an average temperature of 1 eV.

$$\lambda_D = \sqrt{\frac{\varepsilon_0 k_B T_e}{n_e q^2}}$$

(Eq. 3.5)

Therefore, the spheres are effectively shielded from the wire booms by the dense plasma, and the shorting factor should approach 1.0. At larger radial distances, the density rapidly decreases, and the characteristic temperature increases, causing the Debye length to increase. Assuming typical plasma sheet parameters, $n_e = 1\ cm^{-3}$ and $T_e = 5$ keV, the Debye length is 525 m, so we would expect Debye shielding to be negligible and the shorting factor to approach the 0.7 value reported by Bonnell et al. [2008].

Ion velocity measurements from the electrostatic analyzer (ESA) in the inner magnetosphere are complicated by background radiation and cold temperatures, so a comparison of the frozen-in electric field to the double-probe measurement is not possible for our study. Instead, we use the sum of **vxB** from spacecraft motion and the co-rotation electric field as a reference to infer the shorting factor.

$$\boldsymbol{E} = \boldsymbol{v_{sc}} \times \boldsymbol{B} - (\boldsymbol{\omega_E} \times \boldsymbol{B}) \times \boldsymbol{B}$$

(Eq. 3.6)

The spacecraft velocity $\boldsymbol{v_{sc}}$ is well known from ephemeris, the magnetic field $\boldsymbol{B}$ is measured by the onboard magnetometer [Auster et al., 2008], and the $\boldsymbol{\omega_E}$ is the rotation rate of the earth. The true electric field is expected to deviate from pure co-rotation outside the plasmasphere, and even inside the plasmasphere there is a known average lag near 2-3 R_E [Sandel et al., 2003]. In order to mitigate the impact of deviations from pure co-rotation, we only use data from quiet intervals, which are defined by $K_p < 2$ for 3 consecutive days and $K_p < 1$ for each data point. During quiet times, the plasmasphere is not expected to be undergoing rapid reconfiguration, and the co-rotation assumption is expected to be representative on average.

We combined data between 2009-2012 from THEMIS probes A, D and E, which are in ~1.1 x 12 R_E orbits with inclinations of ~10 degrees, to estimate the shorting factor. We used spin-fit electric field data from the long boom pair with 49.6 m tip-to-tip separation.

The electric field is expressed in the Despun Sun L-vectorZ (DSL) coordinate system, which is similar to Geocentric Solar Ecliptic (GSE), except that the Z axis is aligned with the spacecraft spin axis. The spacecraft spin axis is close to the ecliptic normal (GSE Z). The shorting estimate was computed using the DSL Y (~dawn-to-dusk) component of the electric field measurement exclusively because the DSL X component has a sunward offset due to photoelectrons that adds an additional level of complexity. We also only included data between 9-15 MLT where the co-rotation electric field points mostly in the X direction, which limits the impact of the co-rotation assumption on the shorting factor estimate and allows us to rely more heavily on the well-known **vxB** from spacecraft motion.

Examples of the shorting factor estimate for spacecraft potential between 2.3-2.7 V (panel a) and 5.4-5.8 V (panel b) are shown in Figure 3.3. We use the spacecraft potential computed onboard that is provided in the level 2 moment data. The lower spacecraft potential range corresponds to higher densities inside the plasmasphere (Figure 3.3a), and the higher spacecraft potential range relates to lower densities outside of the plasmasphere (Figure 3.3b). First, a linear fit was computed between the measurement and the predicted electric field (**vxB** + co-rotation). Next, the measurement residuals were calculated with respect to the linear fit, and outliers with residuals greater 3 standard deviations were removed. This process was repeated 5 times, and for a typical bin less than 5% of the measurements were removed as outliers. To produce the shorting factor as a function of spacecraft potential, a sliding window of +/- 0.2 V was used for spacecraft potential, resulting in over 200 data points for each bin.

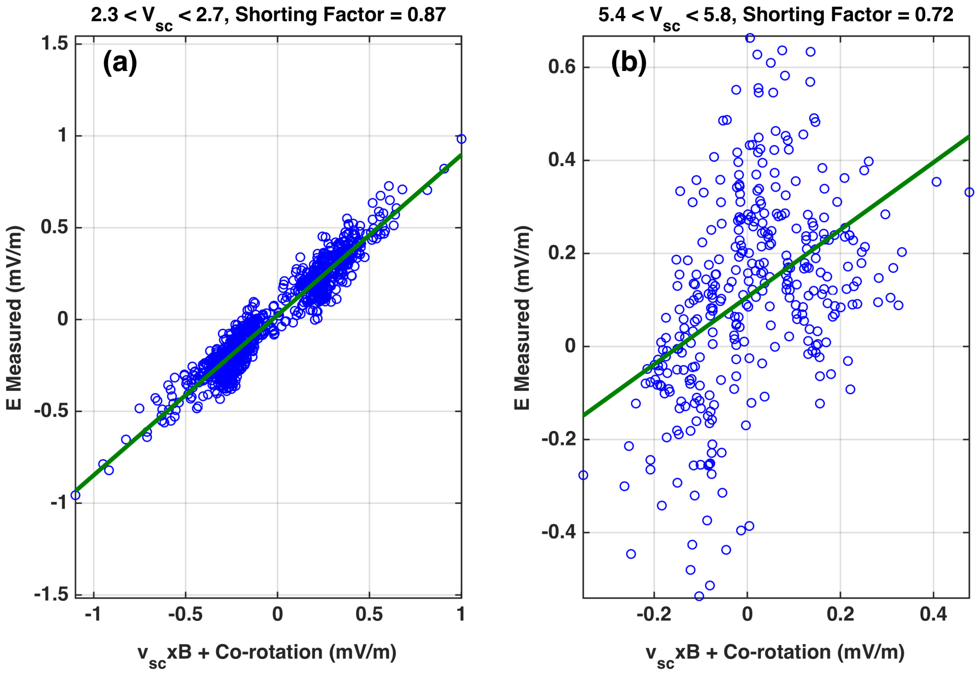

Figure 3.3: Examples of the empirical shorting estimate from THEMIS data for (a) 2.3 < V_{sc} < 2.7 and (b) 5.4 < V_{sc} < 5.8.

The empirical shorting factor is shown as a function of spacecraft potential in Figure 3.4a. For low spacecraft potential, the shorting factor is close to 1.0, which means that there is no scale factor error on the measurement. This is an intuitive result because these small potentials correspond to high density, so the probes should be shielded from the booms by the ambient plasma and the measurement should not be shorted. The tight clustering of points in Figure 3.3a suggests that there is little contamination from plasmaspheric wake effects [e.g., Khotyaintsev, 2014]. As spacecraft potential increases, the shorting factor decreases from 1.0 toward 0.7, where it appears to asymptotically approach 0.7 between 3 < V_{sc} < 5 V.

Above V_{sc} = 5 V, the shorting estimate becomes much more variable due to excessive scatter in the data. In Figure 3.4b, the standard deviations for the measurement residuals with respect to the linear fit and the predicted electric field are plotted for each bin of spacecraft potential. For low spacecraft potential, the predicted electric field (**vxB** + co-rotation) has a large standard deviation, while the variability in the measurement is small. This allows the slope to be estimated more accurately (Figure 3.3a). Near 5 V, the variability in the measurement approaches and then exceeds that of the predicted electric field (**vxB** + co-rotation) (Figure 3.4b), leading to the inaccurate shorting factor estimates for higher potentials. The physical interpretation is that the spacecraft is likely inside the plasmasphere when the potential is small, and the true electric field is more accurately represented by pure co-rotation. For higher potentials, the spacecraft may be outside the plasmasphere, where real variations in the electric field are expected to dominate co-rotation.

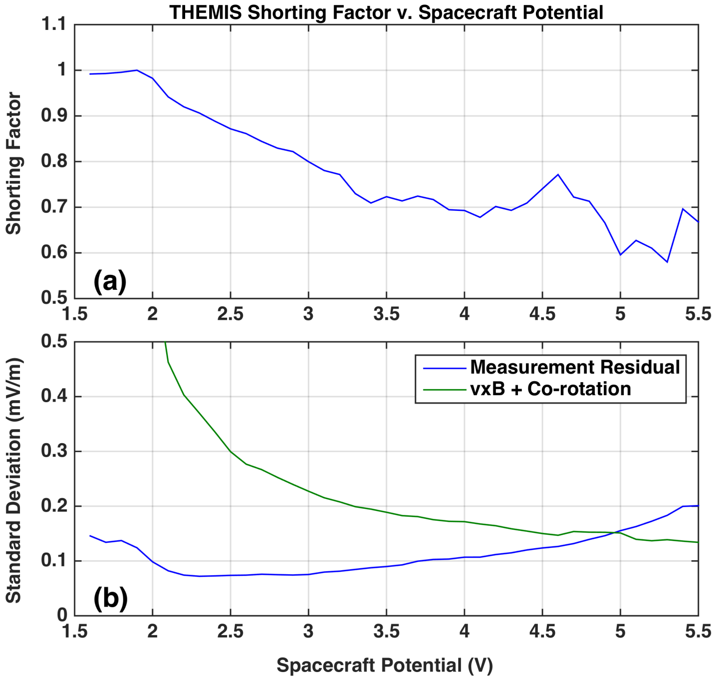

Figure 3.4: (a) Empirical shorting factor as a function of spacecraft potential, (b) standard deviations of the measurement residuals and the predicted electric field (vxB + co-rotation). The shorting factor estimate is poor when the spread in the residuals is greater than the spread in the predicted electric field.

The inverse relationship between the shorting factor and spacecraft potential is apparent in Figure 3.4a. We suggest that changes in the shorting factor are driven by changes in the Debye length, which are also correlated with the spacecraft potential. Ideally, the Debye length would be computed using measured temperature and density (Eq. 3.5), but these measurements are not reliable in the inner magnetosphere for THEMIS. Rather, we use an empirical technique to infer density from spacecraft potential [Nishimura et al., 2013], and then assume a range of temperatures to demonstrate the sensitivity of the results to the temperature assumption. It should be noted that the conversion from spacecraft potential to density is a rough approximation that likely changes over time due to varying surface properties and solar EUV emissions, so these results should be interpreted with caution.

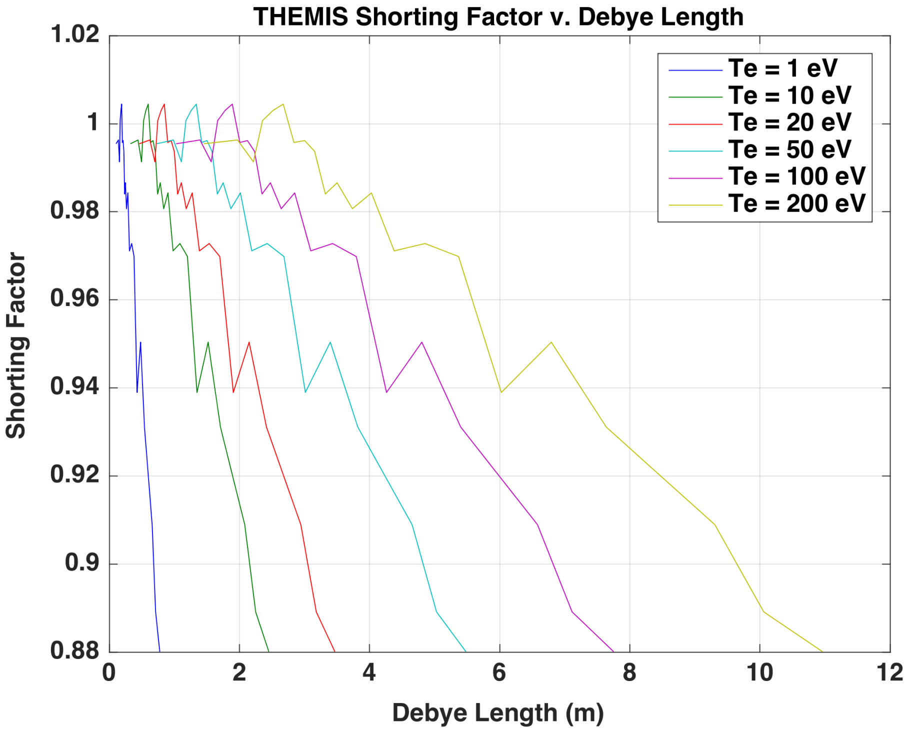

Figure 3.5: Empirical shorting factor as a function of Debye length for a range of assumed temperatures.

The empirical shorting factor is plotted as a function of Debye length in Figure 3.5. Data points corresponding to $V_{sc} > \sim 3.5$ V were not plotted due to the increased uncertainty in estimating the shorting factor for higher spacecraft potential that was discussed earlier, and the same outlier rejection scheme was used to remove data points outside of 3 standard deviations from the mean in each bin. A variable bin width was chosen to ensure that there were 300 data points or more in each bin. The shorting factor decreases with increasing Debye length as expected, however, the temperature assumption is a significant factor in determining the absolute relationship with Debye length. The THEMIS booms are ~25 m long, but the outer braid of the wire is driven to the spacecraft potential out to the preamp, which is only 3 m from the spherical probe. Therefore, one might expect that shorting would begin to become effective for Debye lengths on the order of 3 m or greater, and that the instrument may behave as if it were in vacuum once the Debye length is near the 25 m boom length. The significance of the relationship between shorting and Debye length will be discussed in more detail in the comparison to the simulation results.

3.3 Simulations

In order to interpret the experimental results presented in section 3.2, we ran a number of simulations of increasing complexity, starting from simple analytical models and progressing through fully self-consistent models with realistic physical parameters and geometry. To provide context for the calculations described below, we first describe a few salient features of the THEMIS EFI physical system of booms and sensors (Figure 3.6).

The THEMIS EFI booms are composed of several electrically isolated sections [Bonnell et al., 2008]. The first long boom section is enclosed within a wire braid of radius

1.25 mm, which is electrically grounded to the spacecraft. This section connects mechanically to the distal braid, a 3 m long section with the same diameter but with a software-controlled electric potential. In flight, the distal braid potential is frequently commanded to the spacecraft potential, so that electrically it appears as a continuation of the inner (proximal) braid; this is the configuration we consider here. The distal braid connects to the preamplifier enclosure, which has two electrically biased surfaces known as the inner and outer guard. Finally, the preamplifier is connected to the 8 cm diameter sensor sphere by a 3 m long, very fine (radius ~0.1 mm) wire. The total boom lengths (sphere center to sphere center) are 40.4 m (Y boom pair) and 49.6 m (X boom pair). We confine our analysis to the X boom pair.

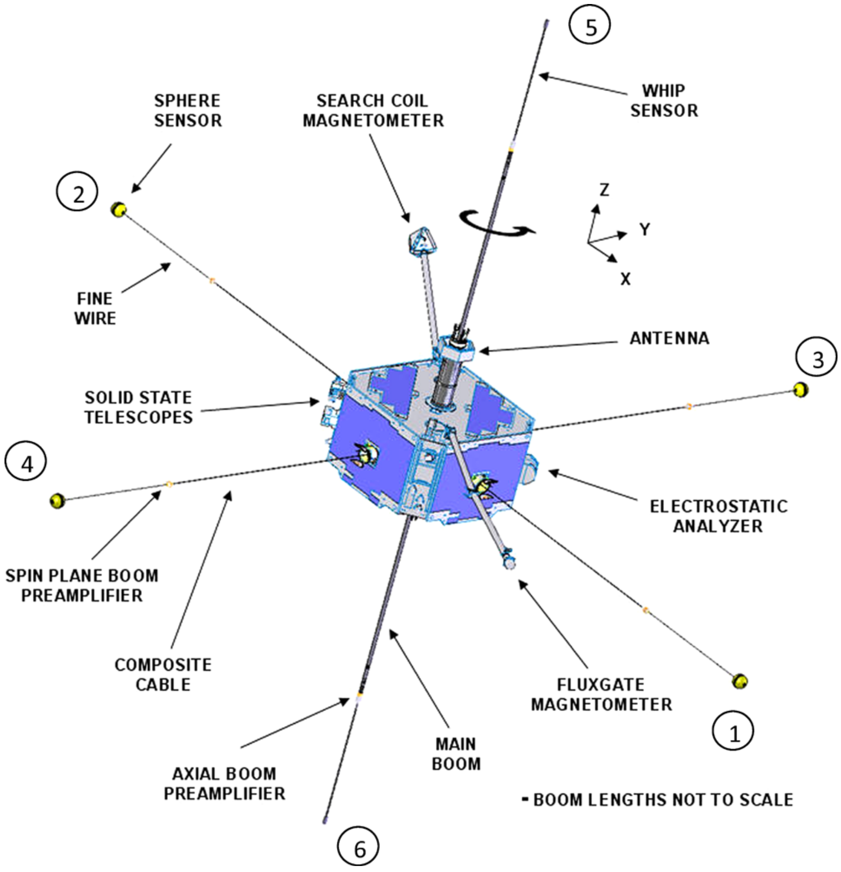

Figure 3.6: THEMIS EFI diagram [Figure 1, Bonnell et al., 2008].

3.3.1 Long Debye Length Limit

Theoretically, the simplest case to analyze is when the plasma density is sufficiently small that the Debye length greatly exceeds any spacecraft or boom dimension. In this case, the plasma can largely be neglected, and the shorting factor can be approximated analytically.

We consider the case when one set of wire booms is oriented in the x direction, parallel with the external electric field E_{ext}. For a simple analytical model, we neglect the spacecraft body and other booms, and model the spacecraft as a single conducting boom in the x direction with length a = 43.6 m (i.e. the separation distance between the preamplifiers). We neglect the sensor spheres and fine wires, and assume that the EFI instrument senses the local potential at the position of the sensor spheres, 3 m from the tips of the wire (i.e. points 49.6 m apart). The sufficiency of these simplifying assumptions will be evaluated below.

The external electric field induces a charge density $\sigma(x)$ on the booms in order to satisfy the boundary condition that the potential at the surface of the boom is constant and equal to the spacecraft potential V_{sc}. Physically, this charge density creates a potential perturbation that counters the applied electric field at the boom, partially short-circuiting the applied electric field (hence the term “boom shorting”). For simplicity, we further assume that the resulting charge density varies linearly as $\sigma(x) = \sigma_0 + {\sigma_0}'x$ with σ_0 and ${\sigma_0}'$ constant. The potential at position (x, y, z) exterior to the wire can then be solved analytically.

$$\phi = E_{ext}x + \frac{1}{4\pi\epsilon_0}\int_{-a}^{a} \frac{\sigma_0 + \sigma_0' s}{\sqrt{R^2 + (x-s)^2}} \mathrm{ds}$$

$$= E_{ext}x + \frac{(\sigma_0 + \mathrm{x}\sigma_0')}{4\pi\epsilon_0}\ln\left[\frac{x - a - \mathrm{x}_1}{x + a - \mathrm{x}_2}\right] + \frac{\sigma_0'(\mathrm{x}_1 - \mathrm{x}_2)}{4\pi\epsilon_0}$$

(Eq. 3.7)

with $R^2 = y^2 + z^2$, a the boom half-length, $x_1 = \sqrt{R^2 + (a - x)^2}$ and $x_2 = \sqrt{R^2 + (a + x)^2}$.

The unknown charge density coefficients σ_0 and σ_0' may then be determined by demanding that $\phi = V_{sc}$ at any two points on the surface of the wire boom. In practice, the points should be selected far from the ends of the boom to avoid overshoot. Figure 3.7 shows the resulting potential at the edge of the wire (R = 1.25 mm), choosing points at the midpoints of the wire booms ($x = \pm 10.9$ m), assuming $V_{sc} = 0.5\ V$ and $E_{ext} = 10$ mV/m. The potential is approximately constant at $\phi = V_{sc}$ in the range from -21.8 m to 21.8 m, and asymptotically approaches the undisturbed potential $\phi = E_{ext}x$ (black) at large $|x|$, as required.

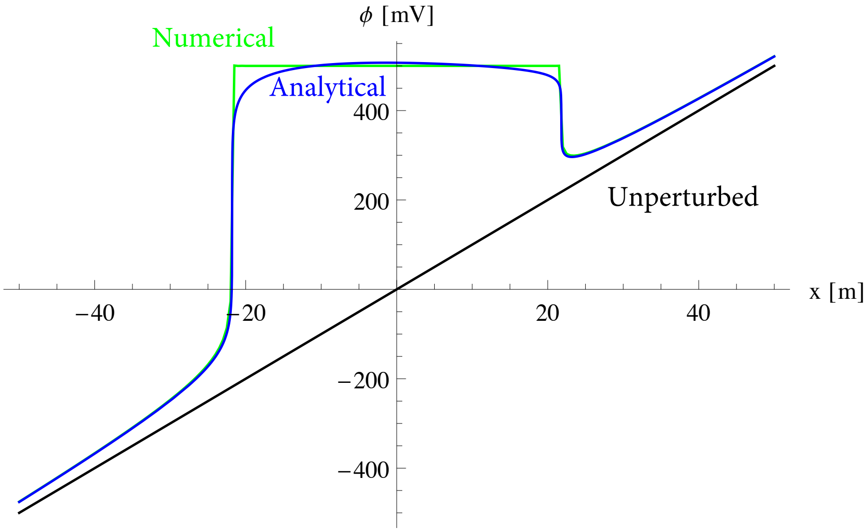

Figure 3.7: Blue: Potential along the line R = 1.25 mm for E_{ext} = 10 mV/m and $V_{sc} = 0.5\ V$ using (Eq. 3.7) and fixing ϕ at $x = \pm 10.9$ m. Black: Unperturbed potential $\phi = E_{ext}x$. Green: Numerical solution for E_{ext} = 10 mV/m and $V_{sc} = 0.5\ V$.

The shorting factor SF is then the ratio of the apparent electric field to the applied electric field, and is independent of both E_{ext} and V_{sc}. Fixing ϕ at $x = \pm 10.9$ m (i.e. the blue curve in Figure 3.7),

$$SF = \frac{\phi(x = 24.8\mathrm{m}, \mathrm{R} = 0) - \phi(x = -24.8\mathrm{m}, \mathrm{R} = 0)}{49.6\mathrm{m}} / E_{ext} = 0.947$$

Unfortunately, this numerical value is in strong disagreement with the experimental results from section 3.2, which show a shorting factor of ~0.7 at large Debye lengths. It is also inconsistent with the value of ~0.7 obtained by Bonnell et al. [2008].

There are several valid objections to the simple analytical solution presented above, and we will address them systematically. The first major objection is the assumed linear variation in the charge density on the wire. This assumption causes the potential to only roughly satisfy the boundary condition at the wire surface $\phi = V_{sc}$ (see Figure 3.7), which creates a strong sensitivity to where the boundary condition is fixed. To overcome this problem, we model the wire as a large number N of end-to-end linear line charges each spanning the distance $x_{1,i} < x < x_{2,i}$ and carrying linear charge density $\sigma_i + \sigma_i' x$. The potential at each line charge (indeed any point in the system) is affected by the charge of all N line charges:

$$\phi = E_{ext} x + \frac{1}{4\pi\epsilon_0} \sum_{i=1}^{N} \int_{x_{1,i}}^{x_{2,i}} \frac{\sigma_0 + \sigma_0' s}{\sqrt{R^2 + (x - s)^2}} \mathrm{ds}$$

(Eq. 3.8)

Instead of the set of 2 equations for σ_0 and σ_0' in the simple analytical solution, this results in a set of $2N$ equations for the $2N$ unkonwns σ_i and σ_i'. Once the $2N$ equations are solved (using LU decomposition or a similar method), the charge density is known, and the potential can be directly evaluated using Eq. 3.8. Using N = 1000, the numerically-determined curve is shown in green in Figure 3.7. With this solution, we find a shorting factor $SF = 0.942$, in surprisingly good agreement with the simple analytical result.

Another objection to the simple analytical model is that it neglects all of the spacecraft structure except for one pair of wire booms. To include the remainder of the spacecraft structure, we used the Boundary Element Method (BEM) code described by Cully et al. [2007]. The code extends the method of multiple line charges described in the previous paragraph to include arbitrarily oriented wires and 2-dimensional triangular surface charges. The model spacecraft includes the 10-sided main spacecraft body with realistic dimensions, both sets of radial EFI booms, the axial EFI booms and both sets of magnetometer booms. The model does not include the preamplifiers or EFI sensors, and the measured potential was again assumed to be the potential at the center of the sensor sphere. With this more realistic model, the shorting factor remains in excellent agreement with the analytical result: $SF = 0.942$.

The next major objection is that the sensor elements are not yet included in the model. Instead, we have so far neglected these elements and assumed that the biased sensor spheres float to the local potential at their locations. To overcome this objection, we include the preamplifier, thin wire and probe sphere in the model from the previous paragraph, and simulate the current-voltage relation (IV curve) for the probe by changing the probe potential and calculating the probe current. Probe currents are calculated by tracing $\sim 10^6$ photoelectrons from all illuminated surfaces, and the electric potential is calculated using the Boundary Element Method with an external electric field [see Cully et al., 2007]. The Boundary Element Method is an integral numerical technique applicable in the long Debye length limit, when the electric potential is dominated by charge on the spacecraft and not charge in the plasma. It is useful for solving the Laplace equation or coupled Poisson-Boltzmann equation in geometries with large discrepancies in scale sizes such as between the THEMIS boom length and thickness. The method and its application to spacecraft modeling are described in detail by Cully et al. [2007] and references therein.

In a tenuous plasma, the photoemission currents at the probe dominate over the plasma currents, which approach zero as the density approaches zero. Consequently, we neglect the plasma current arriving at the probes in the simulated IV curves, since we are interested in the long Debye length regime. Simulated IV curves for both probes on the X boom pair are shown in Figure 3.8 with a 10 mV/m external field. The shorting factor is found by interpolating the IV curve to the operating bias current of -180 nA to find the simulated probe voltage. However, the shorting factor remains in excellent agreement with the analytical result: $SF = 0.94$.

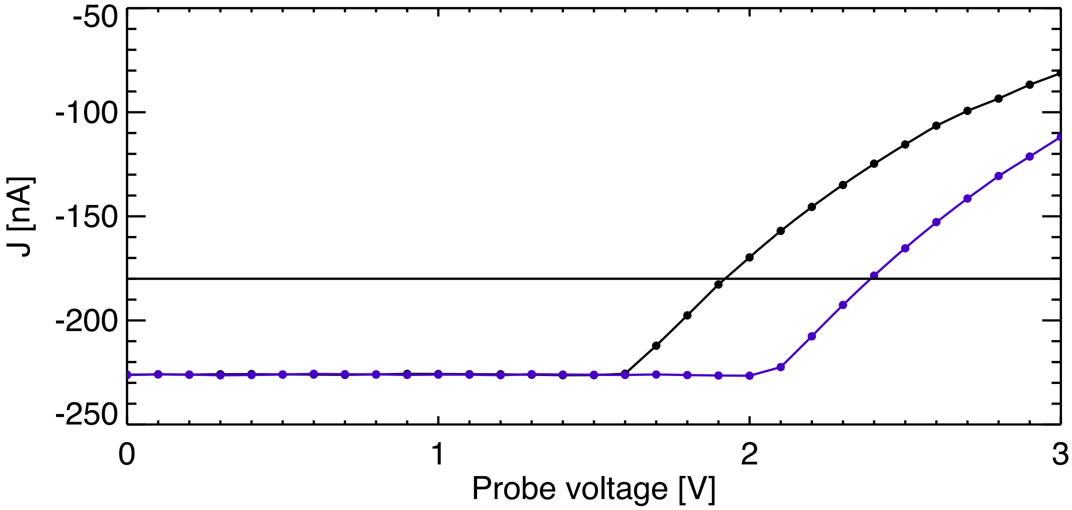

Figure 3.8: Calculated IV curves for the two probes on the X-axis booms, with an applied electric field of 10 mV/m.

The final refinement to the analytical model that we consider is the effect of the cloud of photoelectrons emitted from the spacecraft. The charge in the photoelectron cloud partially short-circuits the electric field in a similar manner to the shorting related to the charge on the booms. The external electric field pulls the cloud into an asymmetric shape, reducing the field seen by the probes. To assess this effect, we simulated the trajectories of $\sim 5 \times 10^7$ photoelectrons emitted from all surfaces, and accumulated the resulting charge density on a 256×256×256 grid. We then solved Poisson's equation on this grid using a fast spectral method to evaluate the potential due to the photoelectron cloud, with Neumann boundary conditions at the grid edges. Finally, we re-ran the photoelectron trajectories including the resulting electric field. The process of running the particles and re-calculating the electric field was iterated 10 times, although the iterations changed very little. We performed the simulations assuming external electric fields of 10 mV/m and 100 mV/m, and found an additional 0.7% shorting resulting from the photoelectron cloud, for a final shorting factor $SF = 0.93$.

Finally, we note that all of the above calculations are essentially similar: integral boundary element methods in various forms. We therefore calculated the vacuum shorting factor using the Spacecraft Plasma Interaction System (SPIS) [Roussel et al., 2008]. SPIS uses an entirely different numerical method to solve Poisson's equation: conjugant gradient on an unstructured tetrahedral grid. Moreover, the method is differential as opposed to integral, and it was developed independently of the authors. Thin elements such as wires can be included in SPIS 5 by situating them at cell edges and expanding the potential out into the cells [Sarrailh et al., 2014]. This method introduces some sensitivity to the exact meshing used for the problem space; experimentally, a coarse mesh results in a smaller calculated shorting factor than a fine mesh. Using a mesh with a 2 cm resolution near the boom tips (requiring ~70 GB of RAM), we built a detailed spacecraft model including all booms at their physical sizes and excluding the probes themselves. We introduced a 200 nT magnetic field and a 10 mV/m electric field, and calculated potentials at the probe locations. The shorting factor calculated from SPIS this way was 0.92, consistent with the other calculations to within the meshing uncertainty.

3.3.2 Intermediate Debye Lengths

The discussion in section 3.3.1 does not include the plasma, which is clearly a shortcoming for comparison with the data from section 3.2, which largely came from the plasmasphere. To construct an analytical model, we consider a Maxwellian proton-electron plasma and assume that V_{sc} is less than the electron and ion temperatures T_e and T_i. In a collisionless plasma with Maxwellian-distributed particles at the boundaries and no internal sources or sinks for the particles, Liouville's theorem demands a Boltzmann distribution for both electrons and ions:

$$n_e = n_0 \exp[e\phi/kT_e]$$

(Eq. 3.9)

$$n_i = n_0 \exp\left[-\frac{e\phi}{kT_i}\right]$$

(Eq. 3.10)

$$\nabla^2\phi = \frac{e}{\epsilon_0}(n_e - n_i)$$

(Eq. 3.11)

For small T_e and T_i, these equations can be linearized and the Green's function for ϕ becomes

$$G(x, x_0) = \frac{1}{4\pi\epsilon_0} \frac{e^{-\frac{|x-x_0|}{\lambda_D}}}{|x - x_0|}$$

(Eq. 3.12)

where $\lambda_D = \sqrt{\frac{\epsilon_0}{n_0 e^2 (1/T_e + 1/T_i)}}$ is the Debye length. We note that the spacecraft both absorbs and also emits particles, which formally makes equations 3.9 and 3.10 approximate and not exact (even prior to linearization). Including the emission and absorption would alter the particle distributions close to the spacecraft, and could potentially influence the result. This possibility will be discussed below.

Following the same derivation as was used for the vacuum case, (Eq. 3.7) becomes

$$\phi = E_{ext} x + \frac{1}{4\pi\epsilon_0} \int_{-a}^{a} \frac{(\sigma_0 + \sigma_0')s\, e^{-\frac{\sqrt{R^2+(x-s)^2}}{\lambda_D}}}{\sqrt{R^2 + (x-s)^2}} \mathrm{ds}$$

(Eq. 3.13)

which has a closed-form solution for $R = 0$ of

$$\phi = E_{ext} x + \frac{\sigma_0}{4\pi\epsilon_0} \left[\Gamma\left(0, \frac{-a + x}{\mathrm{LD}}\right) - \Gamma\left(0, \frac{a + x}{\mathrm{LD}}\right) \right]$$

$$+ \frac{\sigma_0{}'}{4\pi\epsilon_0} \left[-\lambda_D \left(e^{\frac{a-x}{\lambda_D}} + e^{-\frac{a+x}{\lambda_D}} \right) - x\,\mathrm{Ei}\left(\frac{a - x}{\mathrm{LD}}\right) + x\,\mathrm{Ei}\left(-\frac{a + x}{\mathrm{LD}}\right) \right]$$

(Eq. 3.14)

where $\Gamma(\mathrm{a}, \mathrm{z})$ is the incomplete gamma function and $\mathrm{Ei}(z)$ is the exponential integral function. We were unable to obtain an analytical solution for $R \neq 0$.

Eq. 3.14 can be used similarly to Eq. 3.7 to obtain the shorting factor. Unfortunately, the lack of a solution for $R \neq 0$ precludes directly calculating the charge density parameters σ_0 and $\sigma_0{}'$. However, if we assume that the charge density is independent of λ_D, then σ_0 and

$\sigma_0{}'$ can be taken from the long Debye length solution in section 3.3.1. The black curve in Figure 3.9 shows the shorting factor as a function of λ_D under this assumption. As $\lambda_D \rightarrow 0$, the effect of the booms is entirely screened out by the Debye shielding, and the shorting factor is 1. As $\lambda_D \rightarrow \infty$, the shorting factor asymptotically approaches the vacuum value 0.942. These results are in qualitative agreement with the empirical estimate shown in Figure 3.5, but the empirical data suggest that the shorting factor approaches ~0.7 for large Debye lengths rather than 0.942.

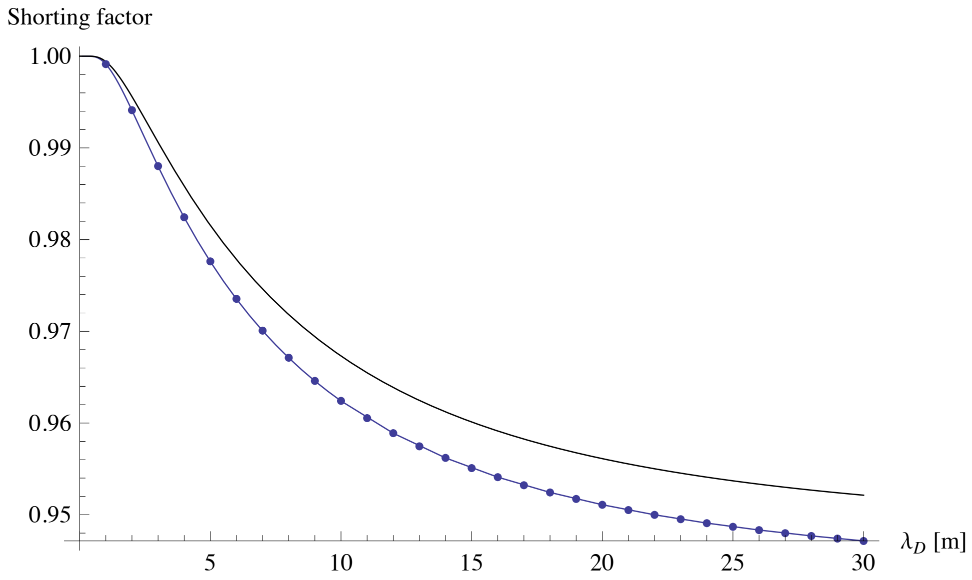

Figure 3.9: Black: analytic solution for the shorting factor as a function of Debye length. Blue solid curve: numerical solution including the boom only. Blue dots: numerical solution including all unbiased spacecraft surfaces.

Alternatively, the boom can be divided up into N short segments, and Eq. 3.13 evaluated numerically. In this case, the lack of an analytic solution for $R \neq 0$ does not interfere with calculating the charge density, and the solution is identical to the numerical solution used above for the vacuum case, but using the modified Green's function (Eq. 3.12). The results of that calculation with $N = 1000$ are shown as the blue solid curve in

Figure 3.9. The numerical solution is reasonably consistent with the analytical solution, although the analytic solution decreases slightly more slowly with λ_D.

The remainder of the spacecraft structure can be included using the BEM formulation of Cully et al. [2007], but using the modified Green's function (Eq. 3.12). The results of this calculation are shown as the blue dots in Figure 3.9. The lack of any discernible difference between this curve (blue dots) and the numerical results using the boom only (blue solid line) highlights that the only spacecraft structure relevant to the boom shorting is the boom wire itself.

Finally, it could conceivably be argued that the plasma environment in the plasmasphere does not allow for the linearization of Eq. 3.9-11, or that the particle absorption/emission near the spacecraft invalidates the Boltzmann assumption, so that the Green's function approach discussed above is not appropriate. The typical spacecraft potential V_{sc} in sunlight exceeds the electron temperature T_e by a small factor, while the linearization formally requires $V_{sc} \ll T_e$. To address this concern, we used SPIS [Roussel et al., 2008] to perform fully self-consistent Particle-In-Cell (PIC) simulations including the ambient plasma and photoemission from the illuminated surfaces, with an accurate model of the spacecraft including the EFI booms. The plasma model was a pure proton plasma with $T_e = T_i = 5$ eV and $n_e = 30$ cm^{-3} (λ_D = 2.1m), with a 200 nT magnetic field. The shorting factor computed from this simulation was 0.97±0.04, consistent with the other calculations.

3.4 Discussion

In the long Debye length limit, we can think of no further refinements that could plausibly affect the shorting factor. All major spacecraft surfaces and booms are included at their real geometric sizes, the probe potentials are calculated using IV sweeps, and the photoelectron cloud is included self-consistently. Some minor refinements are conceivable; for example, the photoemission current of the spacecraft body may be higher than the assumed 4.5 nA/cm^2 (a measured value for the probes derived from in-flight IV sweeps), increasing the impact of the photoelectron cloud. However, given the astonishing agreement between the most sophisticated model considered and the simplest analytical approximation, we find it implausible that further refinements would change the calculated shorting factor considerably. Unfortunately, we are forced to conclude that the expected shorting factor for THEMIS in the long Debye length limit is ~0.94, in disagreement with the experimental result of ~0.7 reported both here and in Bonnell et al. [2008]. It is possible that there are errors in the empirical methods used to estimate the shorting factor, but the independent approaches taken between this study and Bonnell et al. [2008] lead to the conclusion that the shorting factor in low-density plasmas is much smaller than the 0.94 predicted by theory.

3.5 Summary

Understanding the shorting factor is critical for interpreting double-probe electric field measurements, especially for DC measurements in the inner magnetosphere. Small uncertainties in the scale factor associated with shorting can introduce large errors near perigee where the **vxB** electric field from spacecraft motion dominates relevant physical variations in the electric field. We show that the shorting factor for THEMIS changes dramatically in the inner magnetosphere as the spacecraft encounters varying plasma environments. There is an inverse correlation between spacecraft potential and the shorting factor, which is related to plasma density and Debye length. In the most dense plasmas, there is almost no shorting, and in lower densities the shorting factor approaches ~0.7. There are uncertainties in the empirical estimate for lower densities, but the ~0.7 shorting factor is consistent with an independent estimate made in the magnetosheath [Bonnell et al., 2008].

We approached modeling the THEMIS double-probe instrument from various perspectives, ranging from a simple analytical approach to a complex PIC simulation. The behavior of shorting with Debye length was qualitatively consistent with the empirical results, where the shorting factor is near 1.0 for small Debye lengths, and it asymptotically reduces as the Debye length increases. However, in the long Debye length limit, all of the simulations predict a shorting factor of ~0.94, which significantly differs from the experimental result of ~0.7 shown here and in Bonnell et al. [2008].

This discrepancy presents an unsolved problem with many opportunities for future studies from both empirical and theoretical perspectives. Similar double-probe instruments have been and are currently being flown in the inner magnetosphere on CRRES, Cluster, Van Allen Probes and MMS, each with its own unique configuration and supporting instrument suites that may offer insights into the driving factors affecting the shorting factor. The empirical estimate could be obtained using the technique described in this paper with double-probe measurements alone, or by comparing the double-probe measurement to ion drift velocities or an electron drift instrument if available. On the simulation side, the details of the differing spin-plane configurations between missions such as boom length, fine wire dimensions, and biasing schemes could be modeled and compared to empirical estimates of the instrument behavior. We hope to motivate future investigations in order to refine our understanding of double-probe instruments and to ultimately enable new science in the inner magnetosphere.

Chapter 4: Characteristics of the Quasi-static Electric Field

The following chapter is based on work that was published in Califf et al. [2014], THEMIS measurements of quasi-static electric fields in the inner magnetosphere, J. Geophys. Res. Space Physics, 119, doi:10.1002/2014JA020360.

4.1 Introduction

The quasi-static electric field in the inner magnetosphere drives many processes critical to understanding magnetospheric plasma dynamics. The electric field is set up by the interaction of the solar wind with the Earth's magnetic field, creating a large-scale dawn-to-dusk convection electric field that drives plasma Earthward from the magnetotail. Earthward convection transports plasma sheet particles to regions of higher magnetic field strength, where they are adiabatically energized and contribute to the ring current. Curvature and gradient drifts cause electrons to drift eastward and ions to drift westward, leading to a polarization electric field pointing from dusk to dawn that shields the inner part of the magnetosphere from the convection electric field [e.g., Wolf et al., 2007]. This shielding mechanism can break down during large geomagnetic storms, which allows the large-scale electric field to move farther Earthward and sweep away the outer plasmasphere. In the less-dense region outside the plasmasphere, chorus waves can accelerate electrons to radiation belt energies [e.g., Horne et al., 2005], so this inward motion of the plasmapause allows energetic electron populations to form closer to Earth. The coupling between different plasma populations in the magnetosphere highlights the importance of understanding the structure of the quasi-static electric field.

The large-scale dawn-dusk electric field in the inner magnetosphere was previously studied in relation to the Kp geomagnetic index using data from the Combined Release and Radiation Effects Satellite (CRRES) [Rowland and Wygant, 1998]. The CRRES mission was launched on July 25, 1990 into an 18 deg inclination orbit with apogee near geosynchronous and perigee of 300 km. Two key results of this study were that a broad local maximum in the dawn-dusk electric field occurred between L = 3-6 for moderate Kp (4-5), and for the highest geomagnetic activity levels (Kp > 7), strong electric fields were observed inside L = 3. The observed electric fields below L = 3 for high Kp values were not expected based on the conventional model at the time [Volland, 1973; Stern, 1977], which assumed that the electric field was shielded near Earth, and the CRRES results also show that the quasi-static electric field is much more dynamic than a simple superposition of convection and co-rotation suggests.

The Rowland-Wygant [1998] CRRES-based study does not constitute the only prior observational evidence of strong electric fields on subauroral field lines in the dusk-midnight sector. The earliest evidence was ionospheric rather than magnetospheric. Since strong magnetic-field-aligned electric fields are unlikely to exist on subauroral field lines, those field lines are normally assumed to be approximate equipotentials, which means that the equatorial potential pattern can be mapped to the ionosphere and vice versa. In the quasi-dipolar subauroral region, a radially outward electric field in the equatorial plane maps to a poleward electric field in the ionosphere. Narrow (<1°), intense regions of poleward electric field discovered in the topside ionosphere many years ago [Galperin et al., 1974; Smiddy et al., 1977; Spiro et al., 1979] were called "polarization jets" or "SubAuroral Ionization Drift" (SAID) events. SAID events were mainly associated with the late stages of substorms. Later Yeh et al. [1991] used data from the Millstone Hill incoherent-backscatter radar and the ion drift meter on a DMSP polar orbiter during a major magnetic storm to demonstrate the existence of a several-degree-wide peak in the poleward ionospheric electric field in the dusk-midnight sector. After the Rowland-Wygant [1998] paper, Burke et al. [1998] found that SAPS flows observed by DMSP at low altitudes during a major storm lay on approximately the same field lines as strong flows observed by CRRES near the equatorial plane. Later, Foster and Vo [2002] used Millstone Hill data for a detailed statistical study of the strong flow events that occur in major storms and cover a wider range of latitude than SAID events, which are primarily associated with substorms. The storm-associated events were called SubAuroral Polarization Streams (SAPS). The Foster-Vo [2002] study covered a wide range of local time (14 LT to 06 LT). On the theoretical side, Southwood and Wolf [1978] proposed an explanation for SAID events by showing how a region of strong poleward ionospheric electric field (anti-earthward in equatorial plane) is the natural result of the inner edge of plasma-sheet ions, which are primarily responsible for shielding the inner magnetosphere, penetrating farther Earthward than plasma sheet electrons, which are primarily responsible for enhancing ionospheric conductance. The result is that part of the shielding field-aligned current flows into a low-conductance subauroral region of the ionosphere. Completion of the circuit requires an intense electric field across a low-conductance band between the equatorward edge of the shielding current and the equatorward edge of the diffuse aurora. There is no apparent need for a corresponding intense electric field on the dawn side because the plasma-sheet electrons there generally penetrate closer to Earth than most plasma sheet ions. Once the Rice Convection Model developed to the point of treating plasma sheet electrons and ions separately, simulations of substorm conditions [Harel et al., 1981] showed a similar feature. Later simulations [Garner et al., 2004; Sazykin et al., 2005] showed similar features at slightly lower latitudes and covering a wider latitudinal range during magnetic storms, and those features bore a strong resemblance to SubAuroral Polarization Stream (SAPS) events.

More recently, an empirical electric field model was developed by Matsui et al. [2008] based on data from Cluster. Due to the polar orbit of the Cluster spacecraft, magnetospheric electric field observations are mostly measured at high magnetic latitudes, and are then mapped to the equator using a magnetic field model. Additionally, the perigee of Cluster is 4 R_E, so the region below L = 4 cannot be sampled. The low-inclination THEMIS spacecraft allow the equatorial electric field to be measured in situ between 1.5-12 R_E, offering a unique view of the inner magnetospheric electric field that is complementary to the Cluster data.

CRRES provided highly accurate (< 0.1 mV/m) near-equatorial electric field measurements, however, the mission was limited to only 15 months due to an on-orbit anomaly. This caused the data to be biased in local time, with most of the measurements occurring on the dusk side. The question must be raised whether the results of electric field variation with L are duskside features, or if they are applicable to all local times. We address this issue using double-probe electric field data from the Time History of Events and Macroscale Interactions during Substorms (THEMIS) mission [Angelopoulos et al., 2008], which covers all local times and radial distances in the inner magnetosphere for over six years.

This study follows the methodology of the previous CRRES study [Rowland and Wygant, 1998] by sorting the electric field data by Kp to investigate the radial profile of the dawn-dusk electric field, and offers new insights into the local time dependence based on the extensive THEMIS dataset. CRRES offered an order of magnitude more in situ equatorial electric field data in the inner magnetosphere than had been previously published, and THEMIS provides another order of magnitude more data than CRRES.

4.2 Instrumentation

The five identical THEMIS probes were launched on February 17, 2007 with inclinations < 10 deg. The orbit apogees range from 10 to 30 R_E, and the perigees are near 1.5 R_E, allowing for in situ measurements of the near-equatorial electric field over the entire inner magnetosphere. In 2010, two of the probes were moved to a lunar orbit as part of the ARTEMIS mission, but the other three probes continue to offer data from the magnetosphere. This study focuses on data from THEMIS Probes A, D and E, which have apogees of approximately 12 R_E, over the time period from January 1, 2009 and December 31, 2012.

Each THEMIS spacecraft is equipped with an Electric Field Instrument (EFI) [Bonnell et al., 2008] that provides low-frequency electric field measurements in the spin plane, as well as three-axis wave measurements. The spin period of each spacecraft is approximately three seconds, with the spin axis roughly aligned with the ecliptic normal. Electric fields are inferred using the double-probe technique, which compares the potential difference between opposite sensors separated by a large distance from the spacecraft. The spin-plane booms provide 40 and 50 m separation in orthogonal directions, and the axial sensors are 6.9 m apart. Due to the close proximity of the axial sensors to the spacecraft, the low-frequency axial measurement is often contaminated and is generally not considered to be reliable, however, using the frozen-in assumption, the axial component of the electric field can be inferred when the local magnetic field vector is sufficiently out of the spin plane [Bonnell et al., 2008].

For the purposes of this study, we only use electric fields that are directly observed by the spin-plane booms, focusing on the MGSE (Modified Geocentric Solar Ecliptic) Y component. This coordinate system has the Z-axis aligned with the spacecraft spin axis, and the X-axis is chosen such that the Sun is in the X-Z plane. The Y_{MGSE} measurement roughly corresponds to the dawn-dusk electric field in the inner magnetosphere. Using the Y_{MGSE} measurement exclusively also eliminates the complexity of removing sunward offsets due to probe shadowing and photoelectron coupling between the probes and the spacecraft, which are common sources of error for double-probe instruments [e.g., Pedersen et al., 1998].

Electrostatic wakes are also known to introduce spurious electric fields in double-probe measurements [Eriksson et al., 2006]. Wakes are formed when the ion flow velocity is greater than the ion thermal velocity, which causes an ion depletion behind the spacecraft because the incoming ions are blocked by the spacecraft and their thermal velocity is too slow to fill the region. However, the electrons have much higher thermal velocity than the ions and are able to penetrate the wake, resulting in a charge asymmetry and an apparent electric field. As will be shown in section 4.4, the THEMIS data strongly agree with the CRRES results where coverage from the two missions overlaps. The CRRES booms were much longer (~90 m separation) than the THEMIS booms (~50 m separation), so the wake was not a significant factor for CRRES. Due to the agreement with CRRES, we believe that wakes have a minimal impact on the long-term average electric field measurement by THEMIS, and we have not attempted to identify or remove wakes from the data.

The THEMIS EFI measurements have a scale factor uncertainty, known as boom shorting, that causes the measured electric field to be smaller than the true electric field due to coupling between the spacecraft and the probes [Pedersen et al., 1998]. Boom shorting has been estimated to introduce an approximately 30% reduction in the measured electric field by comparing $-\mathbf{v}_i \times \mathbf{B}$ ($\mathbf{v}_i$: ion velocity vector, $\mathbf{B}$: measured magnetic field vector) from the electrostatic analyzer and the fluxgate magnetometer to the double-probe measurement in the magnetosheath [Bonnell et al., 2008]. However, this factor changes as the spacecraft traverses varying plasma environments in the magnetosphere, potentially introducing significant errors near Earth where the induced $\mathbf{v}_{sc} \times \mathbf{B}$ ($\mathbf{v}_{sc}$: spacecraft velocity vector) and co-rotation electric fields, which must be subtracted from the measurement, are much larger than the variations in the dawn-dusk electric field that we are attempting to extract. For the purposes of this study, we have assumed no boom shorting effects in order to minimize the impact of the induced and co-rotation subtraction errors inside the plasmasphere. This may cause the reported electric field to be smaller than the true field for larger L shells, but does not significantly impact on the overall trends with geomagnetic activity.

4.3 Data Processing

This study includes all valid data from THEMIS Probes A, D and E between January 1, 2009 and December 31, 2012. Onboard spin-fit electric field data are used, which are sampled at the spacecraft spin period (~3 sec). The probes rely on photoemission to properly couple to the plasma, so all eclipse periods are removed. Also, large electric field outliers and intervals when the spacecraft potential was outside of the typical range are excluded by visual inspection. The spacecraft potential is usually ~1-2 V near perigee, and it increases to 30-50 V in more tenuous plasmas farther from Earth.

The electric field data are expressed in the frame co-rotating with Earth, so we compute and subtract both the induced $\mathbf{v}_{sc} \times \mathbf{B}$ due to the motion of the spacecraft with respect to Earth's magnetic field and the co-rotation electric field using spacecraft ephemeris data and onboard fluxgate magnetometer measurements [Auster et al., 2008]. Next, the data are averaged in five-minute intervals to filter waves that are not removed by spin averaging. Low-frequency waves with periods greater than five minutes are known to be common in the inner magnetosphere [e.g., Dai et al., 2013], but these waves are sufficiently averaged out by spatial binning and the long time interval of the dataset to accurately represent the average quasi-static component of the electric field. For the radial profile of the electric field, the data are binned by L shell in 1 R_E intervals for a given local time sector. The local time sectors are defined as dusk (15:00 < MLT < 21:00), midnight (21:00 < MLT < 03:00), dawn (03:00 < MLT < 09:00) and noon (09:00 < MLT < 15:00). The L value is computed as the radial distance of the field line at the magnetic equator using spacecraft position and assuming a dipole approximation of the Earth's magnetic field.

A significant amount of effort was expended investigating the details of the spin-fit data and the various systematic biases in the measurement prior to compiling the data for this study. We reviewed the impact of probe shadowing spikes when the sun is close to the spin plane on the spin-fit data, and studied the sunward and anti-sunward offsets that occur inside and outside of the plasmasphere [Califf et al., 2013]. The varying offsets in the sunward component of the measurement present significant challenges for a large-scale statistical study of this kind, and therefore, we have focused only on the dawn-dusk component of the electric field. By comparing the onboard spin-fit estimate of the dawn-dusk electric field to the spin-resolution measurement when the spin-plane booms were aligned with Y_{MGSE}, we determined that the slow-survey spin-fit data very closely match the direct dawn-dusk measurement, even when significant offsets are present in the sunward direction. This allows us to use slow-survey data, which are available over the entire orbit.

4.4 Results and Discussion

Figure 4.1 presents a comparison of the radial profile of the average dawn-dusk electric field based on the CRRES and THEMIS data as a function of the Kp index. The CRRES data were limited to MLT between 12:00 and 04:00, while the THEMIS plot represents MLT from 16:00 and 23:00. The THEMIS local time interval was chosen to approximately match the local times where CRRES had full radial coverage in order to make a meaningful comparison of the observations over the full range of L shells. Each plot shows the mean of the data in a given Kp and L shell bin, and the error bars represent the variance of the mean following the original CRRES study [Rowland and Wygant, 1998]. The error bars are generally smaller than the width of the line used to plot the trends, which reflects an accurate determination of the mean of the sampled data due to the large number of observations included in the study (four years of five-minute averaged data from three spacecraft). Although the mean values are well defined, there is significant variation in any given observation. The standard deviations of the data in each bin are generally on the order of 1-2 mV/m, and increasing variation is observed with higher Kp.

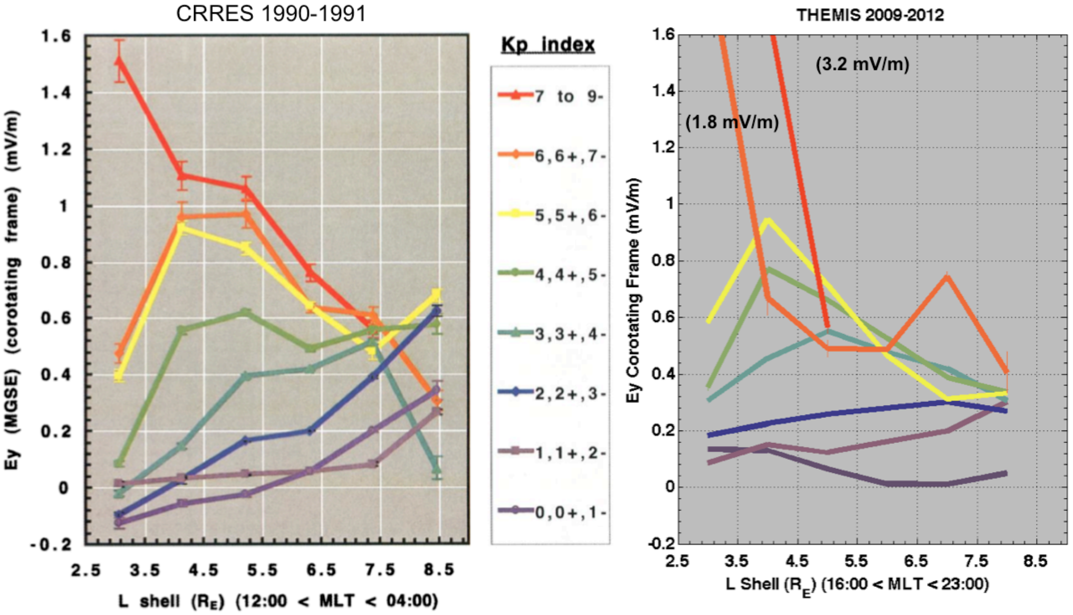

Figure 4.1: Dawn-dusk electric field in the frame co-rotating with Earth as a function of the Kp index. The data are binned in 1 R_E intervals, with the mean of the data plotted at the center of the L shell bin. The error bars represent the variance of the mean. (left) Results from the CRRES mission for MLT between 12:00 and 04:00 [Plate 1, Rowland and Wygant, 1998]. (right) THEMIS observations from 2009-2012 using probes A, D and E for MLT between 16:00 and 23:00.

Qualitatively, the data convey remarkable similarities in the observed structure of the quasi-static electric field as the level of geomagnetic activity increases. The dawn-dusk electric field magnitude generally increases with Kp, and a broad local maximum develops for moderate activity levels between L = 4-5. There were relatively few large geomagnetic storms from 2009-2012, so there are not many data points for the THEMIS results above Kp = 6. However, strong electric fields were observed inside L = 3 during the most active times, which is consistent with the CRRES observations. Additionally, the dawn-dusk electric field is shielded close to Earth for low Kp, as indicated by the approach to zero magnitude as L decreases.

It should be noted that the absolute magnitude of the results below L = 4 may be affected by uncertainties in the induced and co-rotation electric field subtraction related to the variable boom shorting factor for THEMIS, although the relative increase in magnitude with Kp should be independent of this effect. Also, a direct comparison between CRRES and THEMIS measurements for higher L shells could be impacted by the different magnetic latitudes at which the electric fields were measured. CRRES was in a geotransfer orbit, so L shells above 6.6 R_E could only be sampled at latitudes off of the magnetic equator. This has the effect of amplifying the electric field because the magnetic field lines are considered to be equipotentials and they converge at higher magnetic latitudes [Mozer, 1970]. The THEMIS data are also somewhat affected by sampling off the magnetic equator, but with apogees near 12 R_E, the larger L shells can be accessed at lower magnetic latitudes.

The main advantage of the THEMIS dataset is full local time coverage, which enables us to explore the local time dependence of the dawn-dusk electric field. Figure 4.2 shows the results divided into four local time sectors: dusk (15:00 < MLT < 21:00), midnight (21:00 < MLT < 03:00), dawn (03:00 < MLT < 09:00) and noon (09:00 < MLT < 15:00). The data have been restricted to Kp < 6 to highlight the trends in bins where there are a significant number of samples. For Kp > 6, there are relatively few samples (~30 orbits) and the average magnitudes are much larger (up to 3 mV/m) than for less active times, which tends to overwhelm the local time dependency seen in the Kp < 6 bins. The strongest electric fields are observed on the dusk side, with the average magnitudes being approximately a factor of two greater than the other local time sectors, even during quiet times.

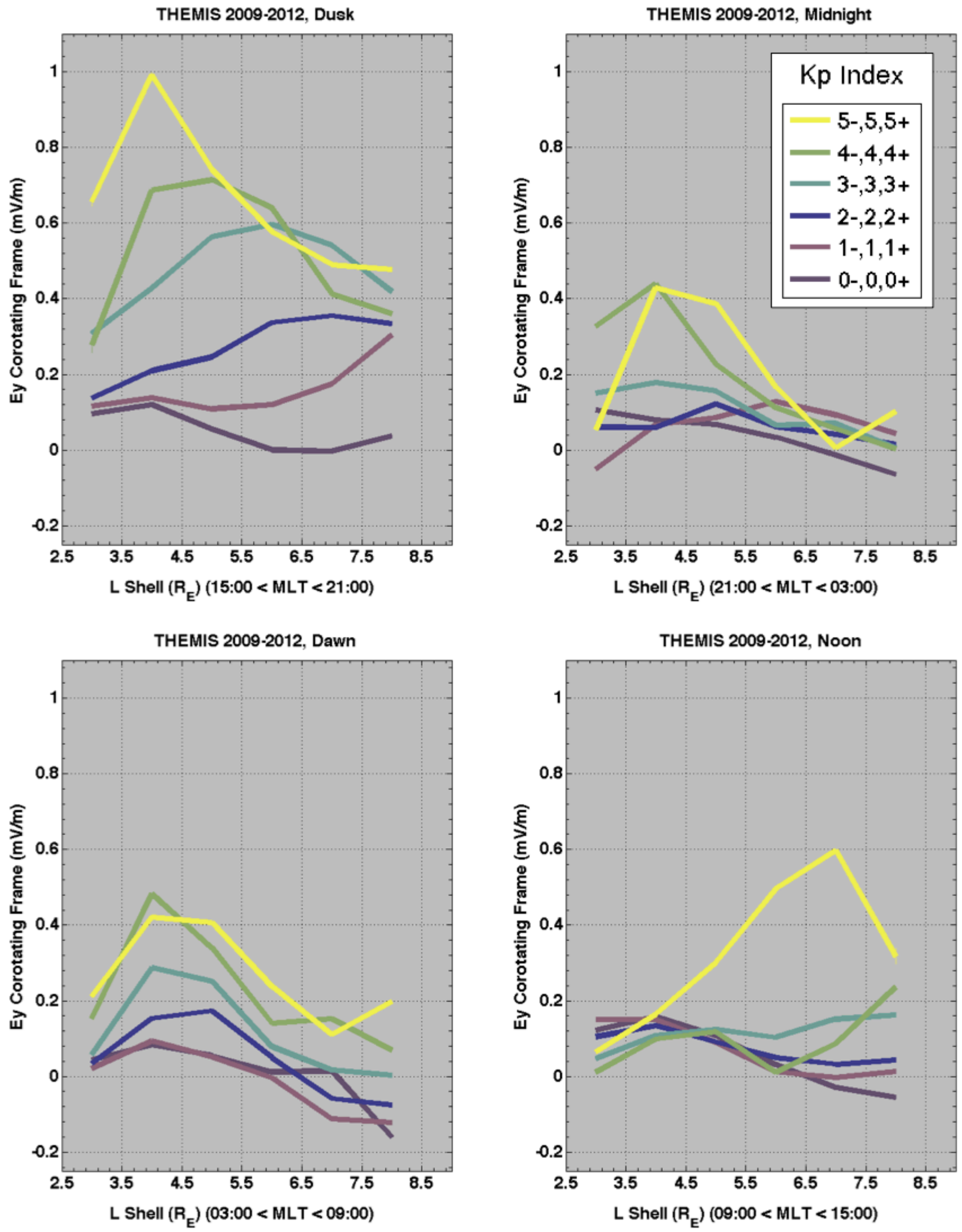

Figure 4.2: Radial profiles of the dawn-dusk electric field in the frame co-rotating with Earth as a function of the Kp index for the dusk (a), midnight (b), dawn (c) and noon (d) local time sectors. Data are only shown for Kp < 6.

The enhanced electric field region between dusk and midnight has been attributed to subauroral polarization streams (SAPS). SAPS are strong poleward electric fields generated by field-aligned currents that close through the low-conductivity region of ionosphere and then map back out the equatorial magnetosphere along magnetic field lines [e.g., Foster and Vo, 2002]. DMSP ion drift-meter data and Millstone Hill radar data from specific events often show two or more peaks in the poleward electric field, plotted as a function of latitude in the dusk sector (e.g., Figure 4.2 of Foster and Vo [2002] and Figure 4.1c of Foster et al. [2014]). However, multiple peaks are not prominent in Figure 4.2. The dual-peak structure is likely smoothed out by the broad-binned statistical averages used in this study, and it is possible that the high-latitude peak maps out to beyond 8 R_E and would not be present in our results.

Generally, the trends for dusk, dawn and midnight are similar, with the local maximum observed near L = 4 for moderate Kp and strong electric fields observed close to Earth in the higher Kp bins. It is especially important to note that the in the midnight sector, there is no clear enhanced dawn-dusk electric field at higher L shells for increased Kp. The Kp index is generally associated with increased magnetospheric convection, so one would expect that as Kp increases, there would be stronger Earthward flows from the magnetotail that would cause an increase in Ey at higher L shells near midnight. These results are a striking illustration of how the electric field in the inner magnetosphere is significantly affected by coupling with the ionosphere, and not purely determined by enhanced Earthward convection from the magnetotail that extends close to Earth.

In the noon sector, the average electric field is almost exclusively below 0.2 mV/m when Kp < 5, and while stronger electric fields are observed for higher Kp, the peak is located near L = 7 rather than L = 4 as in the other local time sectors. We suspected that these enhanced electric fields may have been related to dayside magnetopause crossings, however, only one magnetopause crossing was clearly identified (and subsequently removed from the dataset) for the Kp 5-6 bin in the noon sector inside L = 8.5, and there were ~1 mV/m dawn-dusk electric fields between L = 7-8 leading up to the crossing. While it is possible that the statistics are skewed by some measurements outside of the magnetopause, there is still strong evidence of enhanced electric fields near L = 7 inside the magnetosphere for Kp > 5. There is evidence that the SAPS flow moves to higher latitudes (at ionospheric heights) near local noon, and its equatorial projection (the plasmaspheric plume, which is the plasma carried by the SAPS) moves toward the dayside magnetopause [Walsh et al., 2014]. The increased Ey magnitude seen by THEMIS at L~7 near local noon may be due to crossing the SAPS and plume in this local-time sector.

Synoptic maps of the data for CRRES and THEMIS are displayed in Figure 4.3, with color representing the magnitude of the dawn-dusk electric filed in the frame co-rotating with Earth. The L shell and MLT corresponding to each electric field measurement were converted to Cartesian coordinates, and then were averaged in 0.5 R_E x 0.5 R_E bins. For Kp < 3, there were over 35,000 hours of THEMIS data, and the Kp 3-6 bin was well sampled with 368 days of unique observations comprising over 4000 hours of coverage. However, there were only 12 days of data with Kp > 6-, which coincidentally resulted in most of the sampling occurring on the dusk side during the most active times. It should be noted that the color scales for the CRRES data are held constant, while the color range for THEMIS in Figure 4.3a is smaller in order to accentuate the spatial variation in the electric field during periods of low geomagnetic activity.

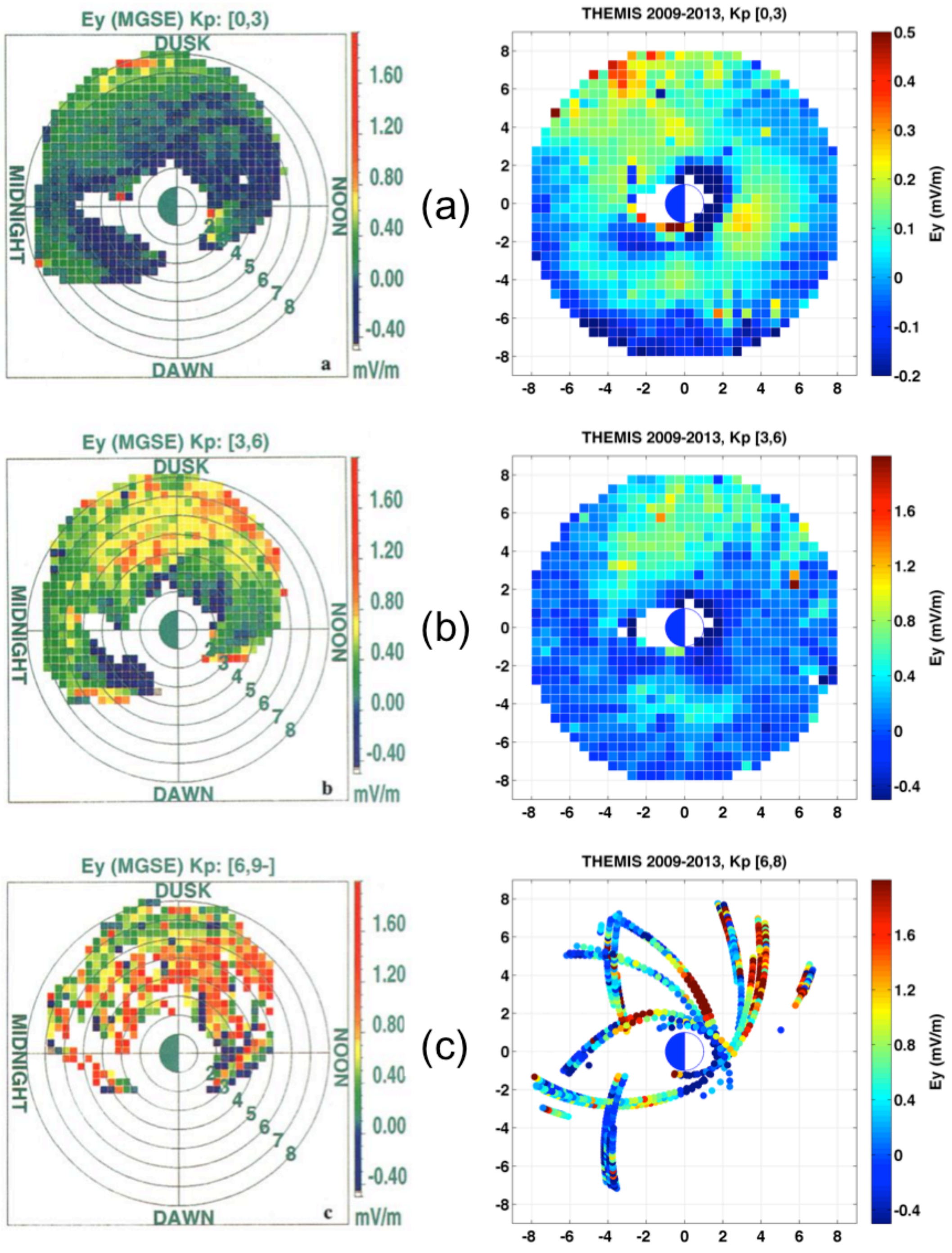

Figure 4.3: Synoptic maps of the dawn-dusk electric field in the frame co-rotating with Earth observed by CRRES (left) [Plate 2, Rowland and Wygant, 1998] and THEMIS (right) for varying levels of geomagnetic activity: (a) 0 ≤ Kp < 3, (b) 3 ≤ Kp < 6 and (c) 6 ≤ Kp < 9. The data shown are polar plots of L and MLT with the Ey magnitude represented in color. Each plot contains spatially binned averages except (c, right), which shows five-minute averages of the electric field from various THEMIS orbits overlaying each other to better convey the data coverage.

Overall, there is excellent agreement in the structure of the large-scale electric field between CRRES and THEMIS for the regions of the magnetosphere covered by both missions. During low Kp intervals ($0 \leq Kp < 3$), the strongest electric fields are in the dusk-midnight sector, with a similar enhancement observed by THEMIS and CRRES near L = 7 just after dusk. The THEMIS results also show electric fields on the order of 0.1-0.2 mV/m spanning L = 3-6 from dawn through noon that was outside of the CRRES coverage, as well as confirmation of a localized enhancement near 11:00 MLT at L = 3 that was present in the CRRES data.

During periods of moderate geomagnetic activity (Kp 3-6), there are enhanced electric fields on the dusk side, concentrated between 18:00-24:00 MLT. The day-night asymmetry of the radial dependence of Ey on the dusk side was noted based on the CRRES results [Rowland and Wygant, 1998], although it was unclear whether this was real, or that it was caused by an increased occurrence of geomagnetic storms during certain phases of the CRRES orbit precession. Based on four years of THEMIS data, we confirm that this asymmetry is a physical feature, with the enhanced region on the dusk side extending as close as L = 3-4 near 21:00 MLT, but being confined to beyond L = 6 by 15:00 MLT. The THEMIS data also reveal a local enhancement of ~0.4 mV/m on the dawn side centered near L = 4 that is outside of the CRRES coverage.

We should remark that Huang et al. [2001] reported on the latitude variations of convective flow observed from Millstone. Their observations were for one major storm and one minor one. For those events, they found a range of local times extending from before midnight to past dawn (in one case) where there was systematic eastward flow at auroral latitudes, but strong westward flow at subauroral latitudes. Their results show the peak of the westward flow at subauroral latitudes occurring at lower latitudes near midnight, and moving to higher latitudes toward dusk, which is in agreement with the duskside features observed by CRRES and THEMIS. On the dawn side, the westward flow reported by Huang et al. [2001] corresponds to Ey < 0 in the equatorial plane, in contradiction to the statistical averages shown in Figure 4.2b. We do not have a compelling explanation for the difference in the two results. Of course, the studies were quite different (e.g., two events vs. statistical average).

A qualitatively similar, locally enhanced dawn-dusk electric field on the dawn side near L = 4 has been observed in a self-consistent magnetospheric electric field model by Gamayunov et al. [2009]. The model specifies the electric potential at high and low latitude boundaries, and then computes the ionospheric potential based on ring current pressure, field-aligned currents and ionospheric conductivity. The magnetospheric electric field is derived by mapping the ionospheric potential back out to the magnetosphere. Although dawn-dusk electric field maxima at lower L shells on both the dawn and dusk sides are qualitatively reproduced by the model, the predicted magnitudes are much larger than the electric fields observed by CRRES and THEMIS. Rice Convection Model (RCM) simulations by Garner et al. [2004] also reproduce a dawnside local Ey enhancement near L = 4, but show an additional negative Ey peak on the dawn side at lower L shells that is not apparent in the THEMIS statistical data. The positive Ey peak near L = 4 and the negative Ey peak at lower L are also seen in Comprehensive Ring Current Model (CRCM) runs by Fok et al. [2003]. The model results discussed here are from individual runs for specific storms, and given the many factors involved in determining the inner magnetospheric electric field, it is not surprising that there are discrepancies between the models and the statistical averages presented in this paper.

For the THEMIS results with Kp > 6 (Figure 4.3c, right), the raw five-minute averages are displayed rather than the binned data to convey the relatively few number of orbits that occurred during periods of high geomagnetic activity. Despite the sparse data coverage, there is clear evidence that the strong electric fields occur close to Earth during very active times. The enhancement also appears to be greater on the dusk side, although much of the dawn side has not been sampled by either mission for Kp > 6. The few THEMIS orbits on the dawn side in Figure 4.3c consistently show electric fields below 0.5 mV/m, but there are many observations with magnitudes greater than 1.5 mV/m on the dusk side. The THEMIS data also highlight the spatial variability of the electric field during active times. For instance, multiple orbits passed through the pre-dusk sector during different time periods with Kp > 6, and some observed electric fields greater than 1.5 mV/m, while others report dawn-dusk electric fields near 0 mV/m in nearly the same spatial location. For Kp < 6, electric field enhancements were observed in very specific locations, but the strong electric fields during the most active times appear to be less predictable, although they are generally concentrated on the dusk side.

The dawn-dusk electric field is expected to be mostly positive, and is associated with sunward convection from the magnetotail. However, both CRRES and THEMIS observed small average dusk-dawn electric fields in some regions of the inner magnetosphere, possibly indicating anti-sunward convection. Some of these negative electric fields can be attributed to induced and co-rotation electric field subtraction errors in locations close to Earth, but there appears to be a region of slightly negative electric field extending across the entire day side for L < 2 for all Kp values that may be real. This feature cannot be explained simply by a systematic **vxB** subtraction error because the induced electric field is positive on the dusk side and negative on the dawn side. Also, the small negative fields near L = 7 across the dawn side are on the same order as the magnitude of the co-rotation electric field in this region. These observations could indicate average stagnant flow, rather than the apparent anti-sunward convection that arises from subtracting the expected co-rotation electric field.

The extensive dataset from THEMIS offers important new insights into the structure of the quasi-static electric field as the geomagnetic activity level changes, as this is the first study to provide complete local time coverage based on in situ equatorial measurements. First, the revolutionary results first reported by CRRES are confirmed, showing that the electric field is enhanced near Earth during moderately to highly active times. This behavior is consistent in the dusk, midnight, and dawn sectors, although the magnitudes are greater on the dusk side. Near local noon, we observed behavior more consistent with the conventional model of an externally imposed large-scale convection electric field that is shielded near Earth, although the enhancement at higher L shells near noon may be related to SAPS moving to higher latitudes and convecting the plasmaspheric plume toward the dayside magnetopause. Also, the ambiguity of the day/night asymmetry in the CRRES results has been resolved, with enhancements occurring closer to Earth in the dusk-midnight sector and at larger radial distances in the pre-dusk sector. The dawnside enhancement near L = 4 for moderate to high Kp is a new magnetospheric observation made by THEMIS, as CRRES did not sample the dawn side. This feature is commonly explained by SAPS on the dusk side, however, SAPS are not thought to be prevalent beyond

03:00 MLT [Foster and Burke, 2002]. Additionally, a poleward SAPS electric field would produce a negative Ey on the dawn side, which is in the opposite direction of the THEMIS statistical observations.

4.5 Summary

The quasi-static electric field in the inner magnetosphere is much more spatially dynamic than the basic model of convection and co-rotation suggests. Previous observations by CRRES offered the first in-depth view of the structure of the large-scale electric field using in situ measurements near the equatorial plane. The results showed that the dawn-dusk electric field is shielded near Earth for low Kp, and that there is a local maximum near L = 4 during periods of moderate geomagnetic activity. Also, strong electric fields were observed near L = 3 during the most active times. However, the CRRES measurements were limited to the dusk side, motivating our effort to cover all local times using THEMIS.

Observations from THEMIS confirmed the CRRES results on the dusk side, and, for the first time, provided a detailed view of the quasi-static electric field across the entire inner magnetosphere using in situ equatorial measurements. These results revealed a strong local time dependence of the structure of the electric field. The largest electric fields were located on the dusk side, with a maximum appearing closest to Earth near 21:00 MLT. On the dawn side, there was a similar peak in dawn-dusk electric field at L = 4, but overall, the magnitudes were about a factor of two smaller than on the dusk side. The smallest average electric fields were observed in the noon sector, and as Kp increased, the peak was found to be located farther out, near the dayside magnetopause, in contrast to the enhancement near L = 4 for the other local time sectors.

These results using the full local time coverage of THEMIS are important to understanding the dynamics of plasma in the Earth's magnetosphere and the coupling between the ionosphere and the magnetosphere. Previously, this type of complete picture of the electric field has only been available by mapping high-latitude ionospheric measurements to the equatorial magnetosphere using magnetic field models. Also, the somewhat controversial CRRES results of enhanced electric fields near Earth have been strongly confirmed, with the additional detail that the behavior is not observed near local noon. Finally, the local maximum in Ey on the dawn side near L = 4 during periods of moderate geomagnetic activity is a new observation that was not covered in the CRRES data.

Chapter 5: The Cause of the Strong Duskside Electric Fields

The results in Chapter 4 demonstrate that the large-scale electric field in the inner magnetosphere is much more structured than the simple model of convection and co-rotation suggests. There are strong electric fields on the dusk side, and during active times the electric field is enhanced at low L shells. Next we investigate the cause of the strong electric fields at low L shells on the dusk side using equatorial magnetospheric measurements from the Van Allen Probes and low-altitude, high-latitude observations from DMSP. The following chapter is based on work that was published in Califf et al. [2016a], Large-amplitude electric fields in the inner magnetosphere: Van Allen Probes observations of subauroral polarization streams, J. Geophys. Res. Space Physics, 121, doi:10.1002/2015JA022252.

5.1 Introduction

Subauroral polarization streams (SAPS) [Foster and Burke, 2002] play an important role in modifying the electric field in the equatorial inner magnetosphere, contributing to a region of intense electric fields in the dusk sector. SAPS are typically discussed from an ionospheric point of view as a strong westward plasma flow equatorward of the auroral precipitation boundary commonly occurring between dusk and predawn [Foster and Vo, 2002]. The westward flow corresponds to a poleward electric field in the ionosphere, which maps to the equatorial magnetosphere as a radially outward electric field.

SAPS arise from coupling between the magnetosphere and the ionosphere, and the location and intensity of the flow depend on numerous factors, including plasma sheet particle precipitation boundaries, magnetospheric pressure gradients, field-aligned currents and ionospheric conductivity [e.g., Southwood and Wolf, 1978; Anderson et al., 2001]. During periods of enhanced convection, plasma sheet ions and electrons are transported from the tail into the inner magnetosphere. Due to the combination of convection, co-rotation, and oppositely directed gradient drifts for ions and electrons, the inner edge of the plasma sheet ions is earthward of the inner edge of the plasma sheet electrons of similar energy on the dusk side [e.g., Korth et al., 1999].

Pressure gradients at the inner edge of the plasma sheet ions can lead to Region 2-type field-aligned currents that flow into the ionosphere equatorward of the precipitating electron boundary and close poleward (Figure 5.1). In the absence of sunlight, ionospheric conductivity is driven mainly by precipitating electrons [e.g., Burke et al., 1998], so the current closes through a region of low conductivity between midnight and dusk, leading to a strong poleward electric field in the ionosphere. Additionally, the increased flow speed in the ionosphere leads to frictional heating and increased recombination rates, which can further decrease the conductivity and create a positive feedback effect on the SAPS electric field [Schunk, 1976; Banks and Yasuhara, 1978].

This study focuses on a period of steady southward IMF in late June 2013 where the Van Allen Probes observe strong electric fields spanning the outer edge of the plasmasphere on multiple duskside passes. We investigate the relationship between the electric field and particle measurements in the equatorial inner magnetosphere during this 18-hour period, and we complement the observations with high-inclination data from DMSP. Previous studies comparing equatorial and high-latitude data have focused on magnetically conjugate observations of latitudinally narrow SAID events [e.g. Burke et al., 2000; Puhl-Quinn et al., 2007]. In contrast, our study provides a broad overview of the evolution of the SAPS region and its impact on the inner magnetosphere from an equatorial perspective over the course of a long-lasting geomagnetic storm, with concurrent supporting measurements from high latitude as well. The data suggest that SAPS can be characterized as a broad spatial region persisting for hours that also contains smaller-scale spatial and temporal variation due to numerous earthward-propagating injections. We also show that the SAPS electric field is correlated with plasmasphere erosion and 100s keV electron enhancements deep within the inner magnetosphere.

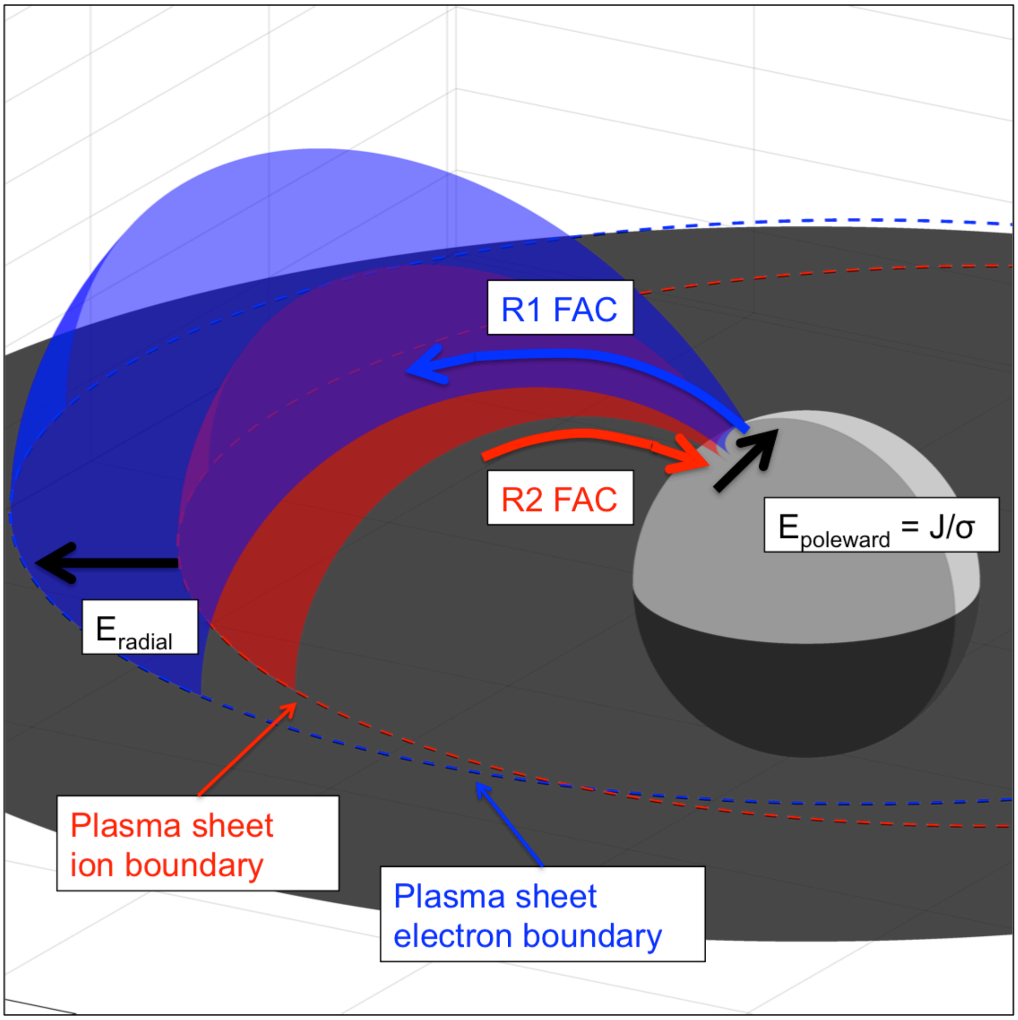

Figure 5.1: Diagram of field-aligned currents flowing into the ionosphere at the inner edge of the plasma sheet ions, which is equatorward of the plasma sheet electrons near dusk. The current closes poleward through a low-conductivity region, causing the strong SAPS electric field that maps to the equatorial magnetosphere.

5.2 Event Overview

On 27 June 2013, a coronal mass ejection (CME) arrived at Earth, causing a geomagnetic storm with minimum Dst < -100 nT that lasted for several days. Figure 5.2 shows the solar wind conditions and geomagnetic indices for the storm. Initially, there was an increase in dynamic pressure from a combination of higher solar wind speed and density in the CME, and then early on 28 June the interplanetary magnetic field (IMF) began to turn southward, which is a signature of a magnetic cloud event [e.g., Kataoka et al., 2015]. The IMF remained steadily southward for 18 hours (dashed lines, Figure 5.2a), and during this period there was increased substorm activity, as indicated by the elevated AE index (Figure 5.2e). The Dst index reached -100 nT during the long-duration main phase, and Dst remained below -70 nT until the IMF abruptly turned northward, initiating a slow recovery over the next two days. During the interval of steady southward IMF, the Van Allen Probes observed large-amplitude DC electric fields spanning ~1 R_E in radial distance over four consecutive outbound passes across the duskside inner magnetosphere. We focus on the cause of the strong electric fields by investigating their relationship to plasma sheet particle boundaries and field-aligned currents both near the equatorial plane and at high latitudes.

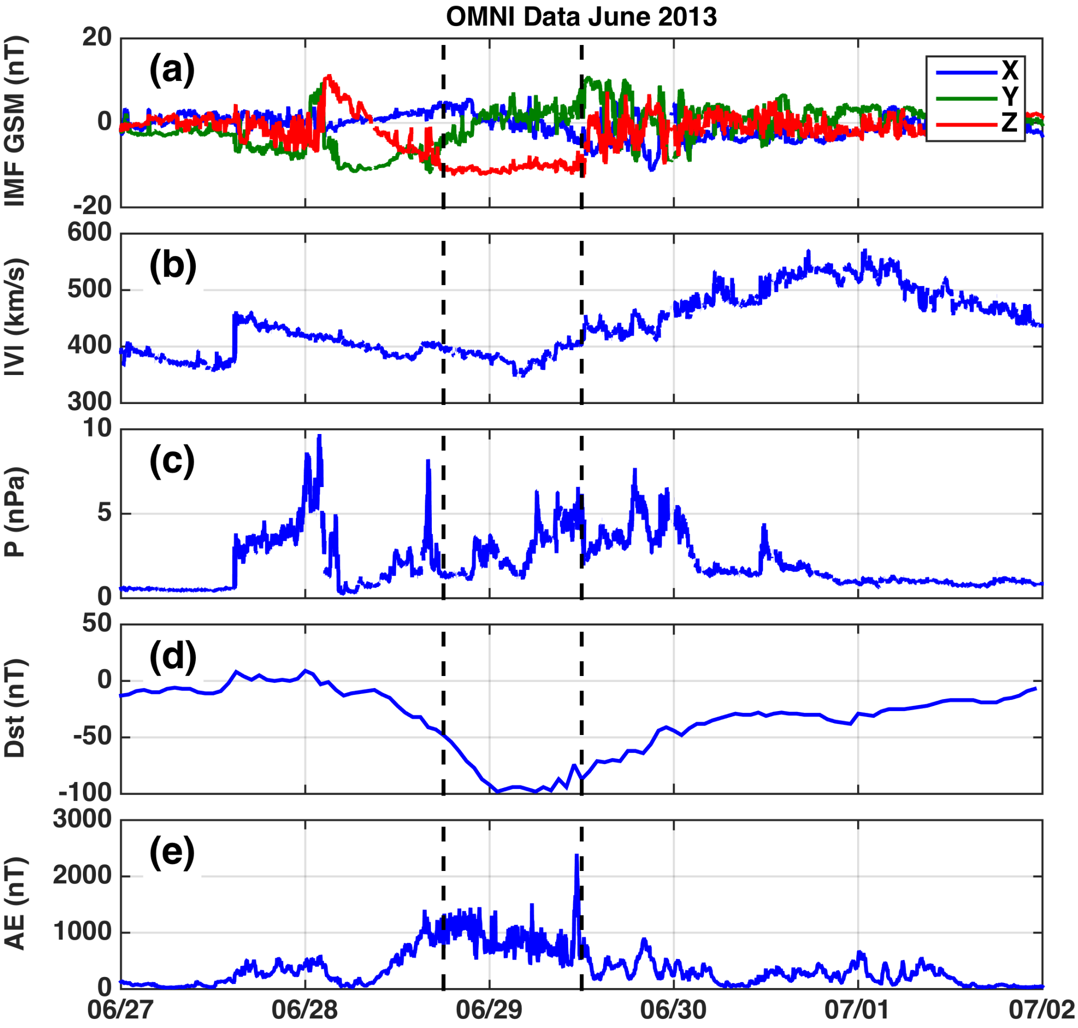

Figure 5.2: Solar wind conditions and geomagnetic indices for the June 29 2013 geomagnetic storm. (a) Interplanetary magnetic field, (b) solar wind speed, (c) solar wind pressure, (d) Dst index and (e) AE index.

5.3 Data Description

The equatorial data are from the twin Van Allen Probes, which are in approximately geo-transfer orbits with ~10 degree inclination. The magnetic latitude of the observations varies between +/- 20 degrees due to the tilted offset of the Earth's dipole, and the spacecraft typically cover all L shells up to L ~ 6 depending on magnetic latitude, although in some cases the L shell can reach L > 12 in the midnight sector [e.g., Saikin et al., 2015].

During the 29 June 2013 time period, both spacecraft have apogees near 21 MLT, and the outbound portion of the orbit provides a radial cut of the equatorial magnetosphere between 18-21 MLT, which is ideal for observing the duskside SAPS feature. The orbital periods are nine hours, and the spacecraft are separated by approximately four hours during this time. We focus on consecutive outbound passes that provide a radial spatial profile of the electric field, plasma sheet particle boundaries and field-aligned currents between L = 2-6. We use DC electric field data from the Electric Field and Waves (EFW) experiment [Wygant et al., 2013] expressed in the frame co-rotating with Earth. EFW also provides a measurement of spacecraft potential, which has been calibrated to estimate density through comparison with the density derived from the upper-hybrid line [Kurth et al., 2015]. We use EFW density primarily to identify the plasmapause. To infer currents, we use fluxgate magnetometer data from EMFISIS [Kletzing et al., 2013], and the ion and electron observations are provided by HOPE [Funsten et al., 2013] for energies up to ~50 keV and MagEIS [Blake et al., 2013] for 50 keV to MeV energies.

To complement the Van Allen Probes observations, we use low-altitude, high-inclination data from DMSP F16, F17 and F18, which are in ~800 km sun-synchronous polar orbits. We use differential particle fluxes from the Special Sensor J (SSJ) covering ions and electrons up to 30 keV to identify the plasma sheet precipitation boundaries and the Special Sensor Magnetometer (SSM) to infer currents. The three spacecraft have orbital planes separated in MLT that provide extensive coverage spanning the dusk side over the course of this storm. Due to the much shorter orbital period of the low Earth orbit spacecraft and the dense nature of magnetic field lines at high latitudes, the DMSP observations capture radial profiles of the inner magnetosphere between L = 2-6 in less than 10 minutes, and the three spacecraft pass through this L range four times per orbit. This allows the entire radial structure of the SAPS region to be sampled every 10-15 minutes at varying local times, contributing both broader and higher-resolution spatial and temporal data to the equatorial picture from the Van Allen Probes, which require over four hours to traverse from L = 2-6.

5.4 Van Allen Probes Observations and Interpretations

The following sections step through the duskside passes in which SAPS electric fields are observed by the Van Allen Probes during the 29 June 2013 storm. In Pass 1 (Figure 5.3), we show the basic structure of the particle boundaries and fields associated with SAPS. Pass 2 (Figure 5.4) contains a sharp electric field enhancement at the inner ion boundary, as well as evidence of multiple injections throughout the region. The lower-energy ions (~20-40 keV) move earthward of the original ring current ions (~200-400 keV) in Pass 3 (Figure 5.5), and the final SAPS structure is observed in Pass 4 (Figure 5.6) before the end of the southward IMF period.

5.4.1 Pass 1: Van Allen Probe B

The first clear observation of the SAPS structure is shown in Figure 5.3 for an outbound pass from Van Allen Probe B (28 June 2013 20-22 UT) near the beginning of the main phase of the storm. The IMF had been steadily southward for two hours before this pass, and the spacecraft observes strong DC electric fields persisting for 40 minutes as the spacecraft moves from L = 3.5 to L = 4.5. We interpret this primarily as a spatial feature that the spacecraft passes through because the general feature is present on multiple consecutive passes over many hours, although there are also temporal characteristics that will be addressed later. The spacecraft begins inside the plasmasphere, where density is large (Figure 5.3b), and then it crosses the plasmapause at the sharp gradient in density near 21:10 UT. We have defined the plasmapause as the most earthward location where the density drops below 50 cc, and this point is marked by a red square in Figure 5.3b.

A high-energy (200-400 keV) ion population is encountered at L = 3 (Figure 5.3e), which was present before the storm and is part of the preexisting trapped ring current [e.g., Daglis et al., 1999; Zhao et al., 2015]. Next, a sharp lower-energy (10-50 keV) ion boundary is encountered near L = 3.5 (blue dashed line, Figure 5.3f) that was not present on the previous pass. The ions form a "nose" configuration, where ~20 keV ions are encountered first, and higher and lower energy fluxes increase at larger radial distances. This is a spatial feature that is a consequence of the energy-dependent drift paths under the influence of co-rotation, convection and magnetic gradient drifts [e.g., Chen, 1970; Smith and Hoffman, 1974].

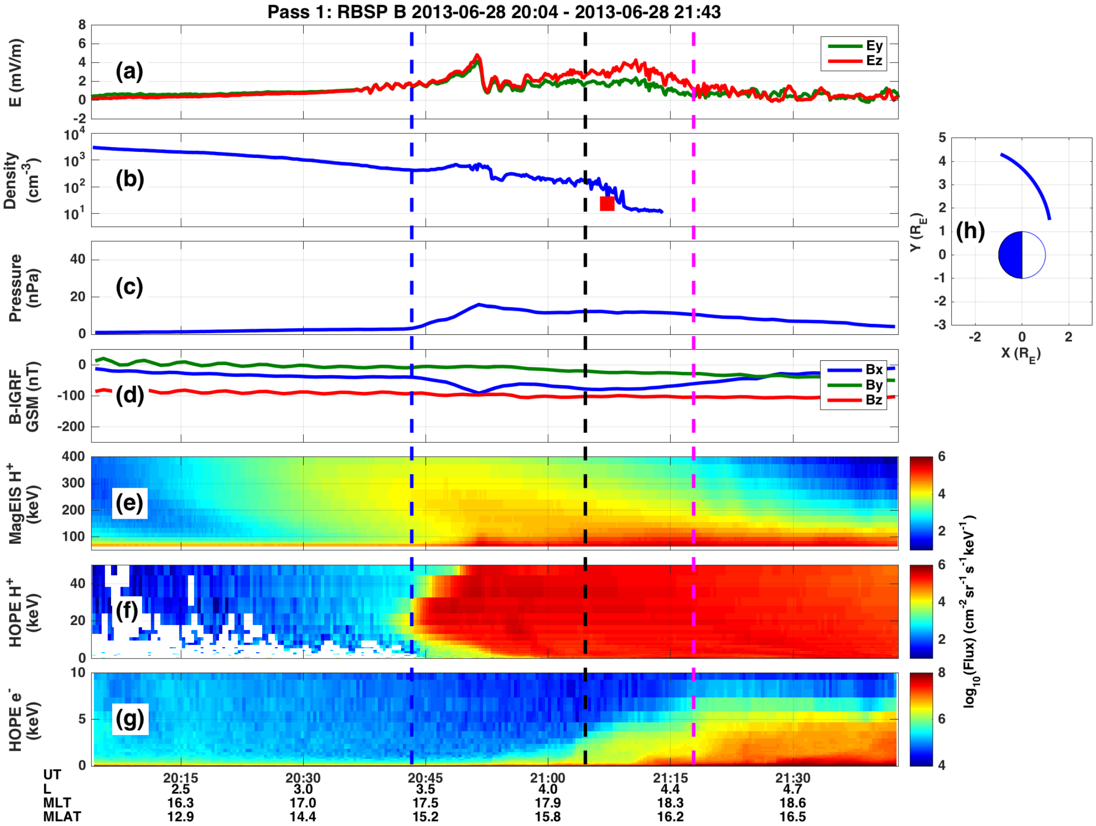

Figure 5.3: Example of SAPS from Van Allen Probe B on 28 June 2013. (a) DC electric field in the frame co-rotating with Earth from EFW, (b) density derived from spacecraft potential, (c) isotropic pressure computed from HOPE and MagEIS particle data, (d) EMFISIS magnetic field with IGRF removed, (e) differential proton fluxes between 50-400 keV from MagEIS, (f) differential proton fluxes between 1-50 keV from HOPE, (g) differential electron fluxes between 0-10 keV from HOPE, and (h) Van Allen Probe B orbit. The vertical lines show the inner boundaries for: 20 keV ions (blue), 2 keV electrons (black) and 5 keV electrons (magenta).

There is an increase in pressure at the inner edge of the ions (blue dashed line, Figure 5.3c) that is accompanied by a negative perturbation in B_x GSM (Figure 5.3d). The blue dashed line indicates the innermost location where the 20 keV ion flux exceeds 10^4 (cm^{-2} sr^{-1} s^{-1} keV^{-1}). The pressure is calculated using ion and electron data with energies of 0.2 keV to 1 MeV from HOPE and MagEIS assuming isotropic pitch angle distributions. Zhao et al. [2015] showed that the isotropic assumption has little effect on the magnitude of the computed pressure, and our focus is on the location of the pressure gradient, rather than the absolute magnitude of the pressure. The magnetic field data shown are the measured magnetic field with the IGRF removed, and slow variations are interpreted as indications of spatial gradients in the GSM Y direction. In the inner magnetosphere near the equatorial plane, the magnetic field is mostly oriented along GSM Z, so the parallel current can be written as

$$J_{\parallel} = \frac{1}{\mu_0}\left(\frac{\partial B_y}{\partial x} - \frac{\partial B_x}{\partial y}\right)$$

(Eq. 5.1)

The negative B_x perturbation as the spacecraft moves in Y is an indication of a field-aligned current from the equatorial magnetosphere to the ionosphere in the northern hemisphere, which is expected given the observed pressure gradient at the inner edge of the ions. Had the spacecraft been off-equator in the southern hemisphere rather than in the northern hemisphere, we would expect a positive B_x perturbation corresponding to a field-aligned current directed toward the ionosphere in the south. Similarly, a positive B_x perturbation in the northern hemisphere is an indication of a field-aligned current out of the ionosphere.

At L = 4.1, more than 0.5 R_E after measuring the nose ion population, the spacecraft meets the inner edge of the 2 keV electrons (black dashed line, Figure 5.3g), and the inner boundary for 5 keV electrons is observed at L = 4.6 (magenta dashed line, Figure 5.3g). The black and magenta dashed lines indicate the innermost location where the 2 and 5 keV electron fluxes exceed 10^6 ($cm^{-2}\,sr^{-1}\,s^{-1}\,keV^{-1}$), respectively. The outer edge of the enhanced electric field region corresponds well with the inner boundary of the 5 keV electrons, but not with the 2 keV electrons. It is possible that the auroral precipitation boundary associated with the outer edge of the SAPS region maps more closely to the 5 keV equatorial boundary, rather than the 2 keV boundary.

The electrons display different energy dispersion than the ions, where lower-energy electrons are observed before higher-energy electrons. The electron enhancement above 2 keV is also mostly located outside of the plasmasphere, whereas the ion enhancement penetrates inside the plasmasphere. The electron energy is mostly below 5 keV, while the ion flux enhancement extends from 10-50 keV. The difference in energy may be attributed to the characteristic energy of the plasma sheet ions being approximately a factor of seven higher than plasma sheet electrons [Baumjohann et al., 1989], as well as the fact that the ions drift closer to Earth at dusk and therefore gain more energy through conservation of the first adiabatic invariant than the electrons.

The pressure gradient near the sharp inner edge of the plasma sheet ions leads to field-aligned currents that flow into the ionosphere, and the inner edge of the plasma sheet electrons is related to the electron precipitation boundary in the ionosphere, which has an associated field-aligned current out of the ionosphere. In the post-dusk sector, precipitating electrons are the primary driver of ionospheric conductivity [e.g., Burke et al., 1998]. Because the ions are earthward of the electrons in the equatorial magnetosphere, the field-aligned current maps into the ionosphere at a lower latitude than the electron precipitation boundary, and the current closes horizontally poleward via the Pedersen current though a region of low conductivity in the ionosphere [e.g., Yeh et al., 1991]. The finite conductivity and poleward current causes a large poleward electric field and corresponding fast westward flow. This high-latitude electric field maps to the equatorial magnetosphere as a radially outward electric field, which is consistent with the broad enhancement in the GSM Y electric field observed by the Van Allen Probes near dusk between the inner edges of the plasma sheet ions and electrons. Qualitatively, the enhanced electric fields in Figure 5.3 agree with the theoretical description of SAPS, although there is some ambiguity in defining the electron precipitation boundary based on the equatorial magnetospheric particle data.

5.4.2 Pass 2: Van Allen Probe A

The radial profile of the particles, pressure, field-aligned currents and electric fields are shown for the following outbound pass by Van Allen Probe A in Figure 5.4. These observations occur four hours after the previous example, and the IMF has been steadily southward for eight hours. Again, the spacecraft encounters a high-energy (200-400 keV) ion population in nearly the same location as the previous pass, followed by a lower-energy ion population with a nose energy near 30 keV. The lower-energy population has a similar spatial structure to the one previously observed by Van Allen Probe B, except that it has moved earthward from L = 3.5 to L = 3.0, and the nose energy has increased from 20 to 30 keV.

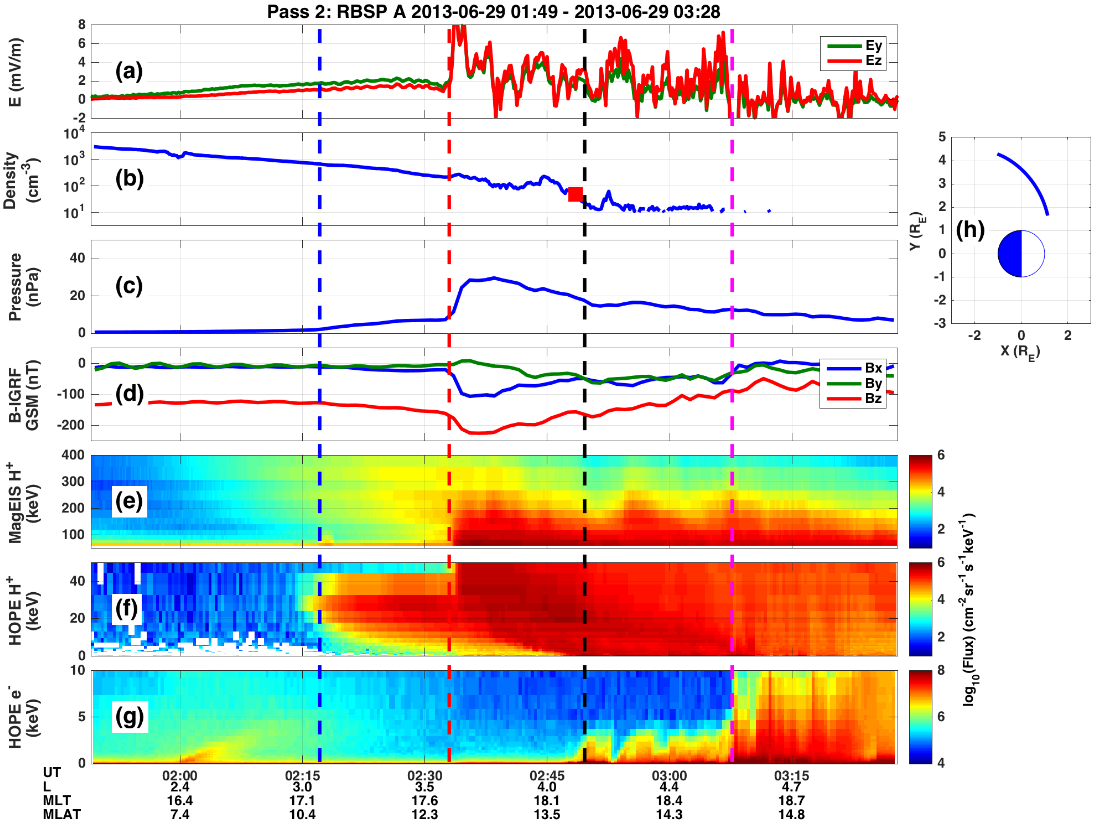

Figure 5.4: Example of SAPS from Van Allen Probe A on 29 June 2013 in the same format as Figure 5.3. The vertical lines show the inner boundaries for: 20 keV ions (blue), 80 keV ions (red), 2 keV electrons (black) and 5 keV electrons (magenta).

On the previous pass, there was a strong pressure gradient and field-aligned current located at the inner edge of the nose ions, but in this case the pressure gradient is smaller and the field-aligned current is either small or non-existent based on the magnetic field data (blue dashed line, Figure 5.4d). Despite the lack of a strong pressure gradient, there is an elevated electric field of ~2 mV/m between L = 2.2-3.6, which is large relative to statistical averages at these low L shells, although not uncommon during very active times. Data from CRRES and THEMIS show that the average dawn-dusk electric field tends to be less than 0.6 mV/m and decreasing in magnitude below L = 3.5 during moderate storms (3 < Kp < 6). However, during the largest storms (Kp > 6) there can be an increasing trend extending inside L = 3 with average magnitudes greater than 1.5 mV/m [Rowland and Wygant, 1998; Califf et al., 2014].

This low-L electric field enhancement is not clearly related to plasma sheet particle boundaries as it begins 0.8 R_E earthward of the inner edge of the nose ions. This is an example of the high-latitude convection electric field penetrating directly to low-latitudes. Penetration electric fields are typically described as short-duration events related to rapid changes in the polar cap potential on timescales faster than the time required to establish ring current shielding [e.g., Greenspan et al., 1991; Burke et al., 1998]. However, observations [Mannucci et al., 2008] and RCM simulations [e.g., Garner et al., 2004] have shown that penetration electric fields can last for hours during large storms.

A second, more dramatic pressure gradient is encountered at L = 3.6 that is accompanied by a very large ~10 mV/m spike in the electric field (red dashed line) and clear magnetic perturbations in both B_x and B_z. At the red dashed line, the 80 keV ion flux increased by more than a factor of 2 within 0.1 L. This electric field spike is followed by a fluctuating electric field with a net positive GSM Y DC component that persists until the spacecraft encounters the inner edge of the 5 keV plasma sheet electrons at L = 4.5 (magenta dashed line). The electric field does decrease briefly at the 2 keV electron boundary (black dashed line). We consider the broad region between the ion and electron boundaries (red and magenta dashed lines) to be the SAPS region. The initial electric field spike is an example of a subauroral ion drift (SAID), which is a more narrow and intense feature within the SAPS region that is generally understood to arise through the same magnetosphere-ionosphere coupling mechanism as SAPS [e.g., Anderson et al., 2001]. The large electric field at L = 3.6 is clearly inside the plasmapause and it is correlated with the pressure increase related to a dramatic flux enhancement for ions between 20-200 keV (Figure 5.4e-f).

5.4.3 Pass 3: Van Allen Probe B

The next pass in Figure 5.5 occurs four hours later, and the low-energy (20-40 keV) ion nose population has moved farther earthward, while the inner boundary of the high-energy ion population has remained relatively constant during the storm. This pass occurs 12 hours into the steady southward IMF period of the storm, and the recovery phase has yet to begin. Similar to the previous pass, there is evidence that the electric field penetrates earthward of the inner edge of the plasma sheet ions and associated pressure gradient with a magnitude of ~1 mV/m extending below L = 2.1. As was described previously, this is an example of a long-lasting penetration electric field [e.g., Mannucci et al., 2008; Garner et al., 2004], and is not caused by SAPS.

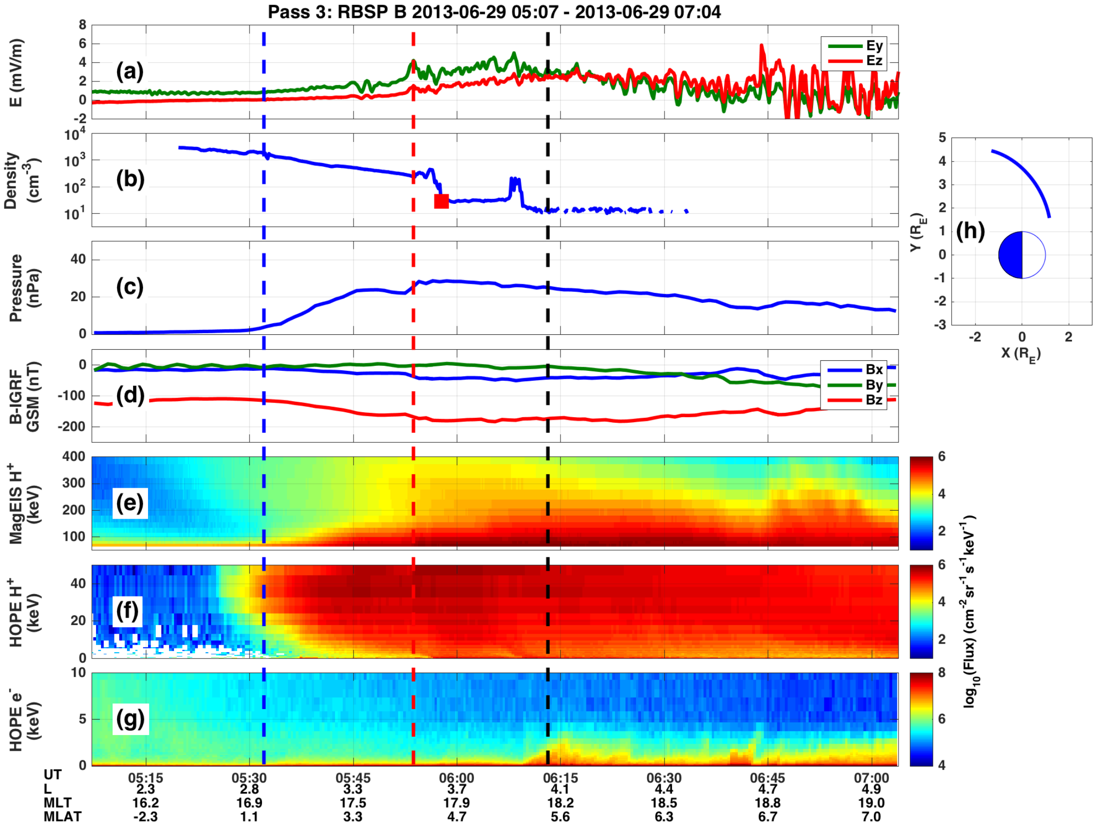

Figure 5.5: Example of SAPS from Van Allen Probe B on 29 June 2013 in the same format as Figure 5.3. The vertical lines show the inner boundaries for: 20 keV ions (blue), 80 keV ions (red), and 2 keV electrons (black).

At the inner edge of the lower-energy nose ion population (blue dashed line) there is a gradual increase in the electric field, and then a sharp enhancement occurs coincident with the inner boundary of the higher-energy ions that is consistent with a SAPS electric field (red dashed line). There is a flux increase of nearly a factor of two for 80 keV ions at the red dashed line. Our interpretation is that an additional injection of 10s keV ions (Figure 5.5e) happened to coincide with the preexisting high-energy ions (200-400 keV), causing an increased pressure gradient, field-aligned current and increased magnetospheric electric field, rather than the electric field being caused by the high-energy ions directly, as this population has been steady throughout the storm. In the region between the initial nose ions and the new injection, the pressure has increased by a factor of 2-3 relative to the previous pass (blue and red dashed lines, Figures 5.4 and 5.5), but the electric field is slightly smaller in magnitude. This demonstrates the significance of pressure gradients, rather than absolute pressure magnitude, in driving field-aligned currents and modifying the magnetospheric electric field.

The SAPS electric field in this case appears to extend from the inner edge of the 20 keV ions at L = 2.8 (blue dashed line, Figure 5.5) out to L = 4.5. However, the electron boundary that defines the outer edge of the classical SAPS region is not so clear. In the first two passes, there was a sharp increase in flux of electrons up to at least 5 keV near L = 4.5 that corresponded well with the outer boundary of the enhanced electric field region, but in this pass the electron energy is mostly below 2 keV.

5.4.4 Pass 4: Van Allen Probe A

The final Van Allen Probe pass that clearly observes the SAPS boundaries and electric field signatures is shown in Figure 5.6. This example occurs at the end of the steady southward IMF period just before the recovery phase of the storm. In this case, the nose ion population has moved farther inward to L = 2.5 and the nose energy is now greater than 40 keV, rather than ~20 keV as in the first pass. The factor of two increase in energy is consistent with the expected energy gain due to adiabatic transport from L = 3.5 to L = 2.5. The high-energy population (200-400 keV) has remained roughly in the same location as in the initial pass. There is an increase in the electric field beginning at the inner edge of the lower-energy ions, and an additional enhancement just inside the inner edge of the higher-energy ions, similar to the previous pass. The 1-2 mV/m penetration electric field at low L shells inside of the inner edge of the nose ions is not present in this case.

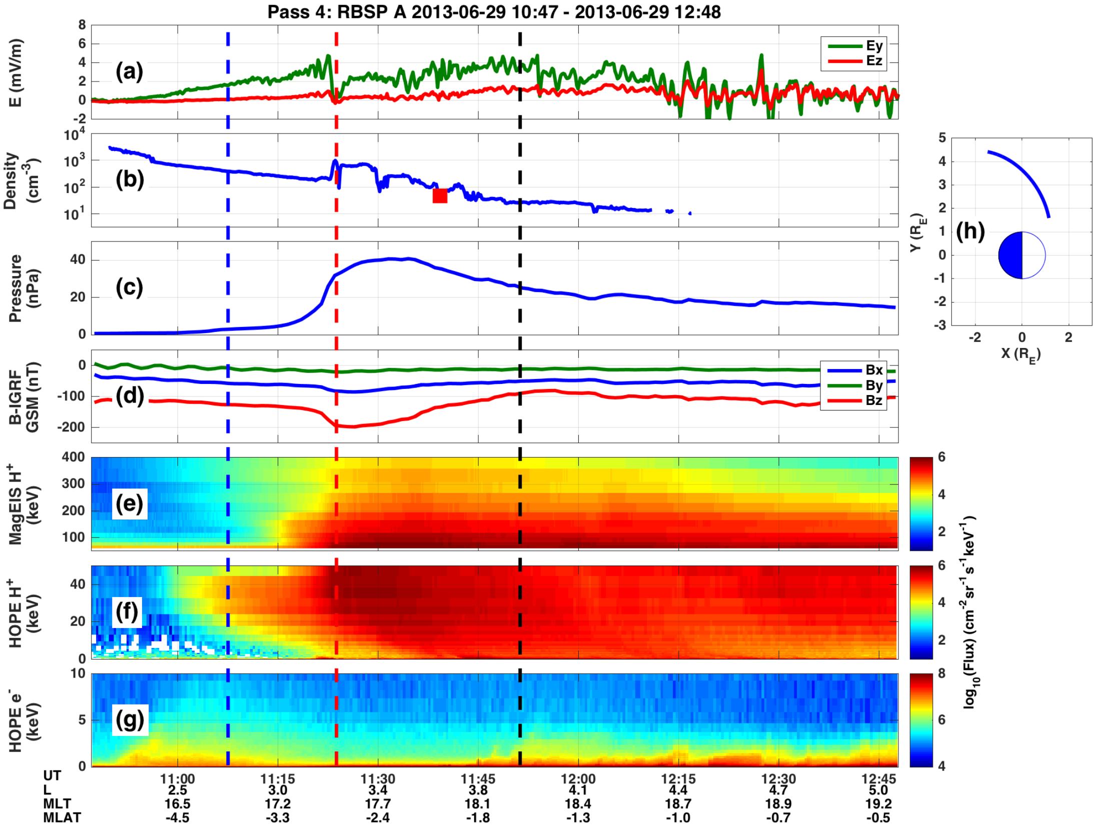

Figure 5.6: Example of SAPS from Van Allen Probe A on 29 June 2013 in the same format as Figure 5.3. The vertical lines show the inner boundaries for: 20 keV ions (blue), 80 keV ions (red) and 2 keV electrons (black).

At the large pressure gradient (red dashed line), there is a rapid decrease in the electric field, followed by a gradual broad enhancement extending out to L = 4.4. Similar to the previous case, the inner edge of the plasma sheet electrons is difficult to identify, and the electron energy is mostly below 2 keV. One difference between the first two passes in which >5 keV electrons were observed near the outer electric field boundary and the last two passes where electron energy was lower is the magnetic latitude of the spacecraft. The higher-energy electrons were observed at MLAT > 15 deg, but the last two passes were closer to the magnetic equator (MLAT < 7 deg) and did not observe the >5 keV electrons. It is possible that the difference is related to magnetic mapping errors, where the actual magnetic field for the first two passes maps to larger equatorial radial distances than the dipole model used to approximate the L shell.

5.4.5 Van Allen Probes and DMSP

In Figure 5.7, the Van Allen Probe A outbound pass (Pass 2, Figure 5.4) is compared to two DMSP passes by F17 and F18 traversing through the dusk sector at high latitudes. The data are plotted versus L shell to compare the spatial structure of the equatorial and high-latitude magnetic perturbations and particle boundaries. The Van Allen Probe L shell is calculated using an Earth-centered dipole model, and the DMSP L shell is based on altitude adjusted corrected geomagnetic coordinates (AACGM). Our goal is to qualitatively examine the relative spatial positions of features related to SAPS.

It is important to note that the Van Allen Probes are in geo-transfer orbits near the equatorial plane, and the spacecraft require 4.5 hours to traverse from L = 2-6, while the DMSP spacecraft are in ~800 km sun-synchronous polar orbits with orbital periods of ~90 minutes, enabling them to sample the high-latitude magnetic field footpoints corresponding to L = 2-6 in ~10 minutes. Therefore, the DMSP data provide a faster snapshot of the radial profile of the particle and fields structures, while the Van Allen Probe data capture both long-lasting, large-scale spatial features, as well as temporal features on timescales much shorter than the 4.5 hours required to sample the entire spatial profile.

The Van Allen Probe A data show an unusually large electric field of ~10 mV/m at L = 3.6 (Figure 5.7a), and the DMSP F17 (Figure 5.7e-g) and F18 (Figure 5.7h-j) passes occur 30 and 6 minutes before the spike is observed in the equatorial plane, respectively. The relative magnetic tracks of Van Allen Probe A, DMSP F17 and DMSP F18 are shown in Figure 5.7k and 5.7l, where the L and MLT coordinates have been plotted in the equatorial plane. The location of Van Allen Probe A during each DMSP pass is indicated by color-coded vertical dashed lines in Figure 5.7a. For example, the red vertical dashed lines indicate the location of Van Allen Probe A over the course of the DMSP F18 pass from L = 2-6 plotted in Figure 5.7h-j.

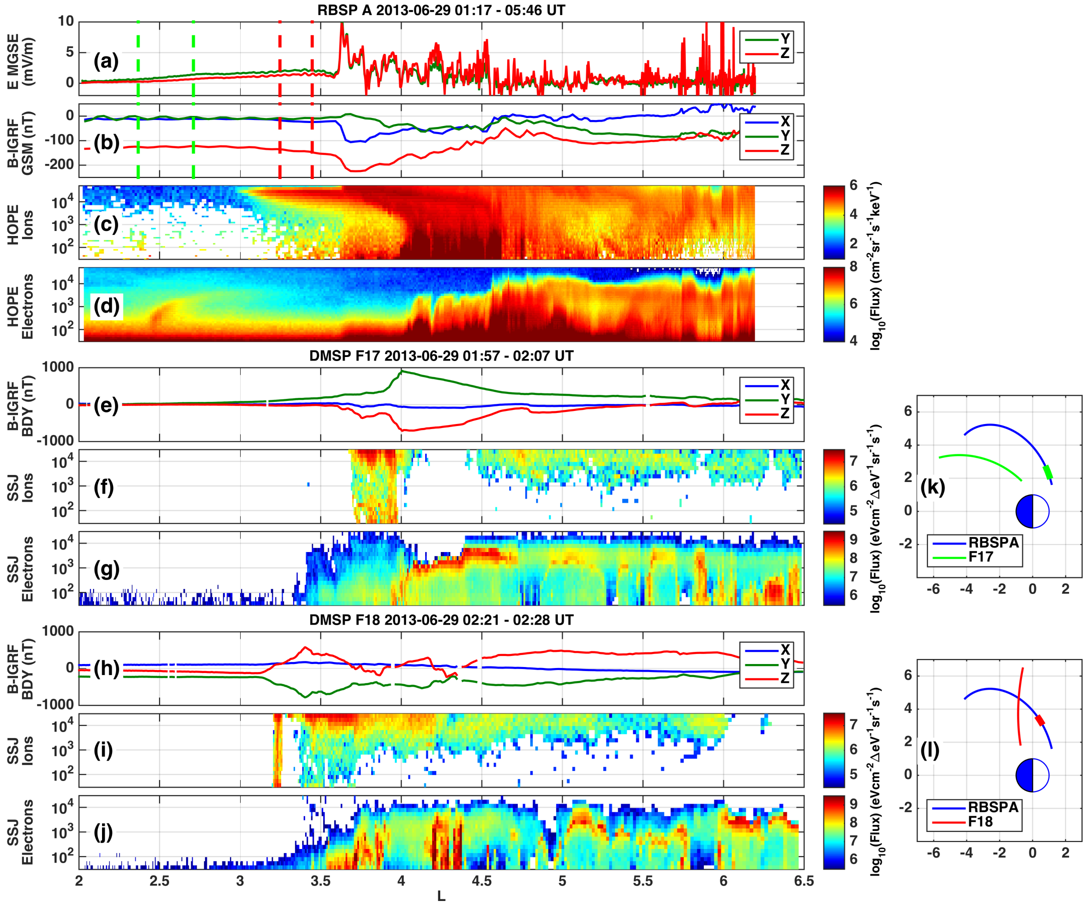

Figure 5.7: Spatial profiles of the electric field, magnetic perturbations, and particle fluxes from the Van Allen Probes and DMSP near a large electric field spike in the inner magnetosphere. The top panels show RBSP A (a) EFW electric field, (b) EMFISIS magnetic field with IGRF removed, (c) HOPE ion fluxes, and (d) HOPE electron fluxes for one outbound duskside pass. Below are DMSP F17 (e) SSM magnetic field with IGRF removed, (f) SSJ ion fluxes, and (g) SSJ electron fluxes. Panels (h-j) display a separate DMSP F18 pass in the same format as panels (e-g). All data are plotted against L shell, although the Van Allen Probes sample the spatial region over 4.5 hours while the DMSP passes occur in 7-10 minutes. The orbit plots in panels (k) and (l) show (L,MLT) coordinates projected into the equatorial

plane, and the location of RBSP A during each DMSP pass is highlighted in the orbit plots in panels (k) and (l), and also with the vertical dashed lines in panels (a) and (b) using the same color scheme to identify DMSP F17 and F18.

The magnetic field data from DMSP are shown with the IGRF subtracted out, and a slope in B_z, which is aligned with the orbit normal vector, is interpreted as a spatial gradient indicating a field-aligned current. The sign of the B_z perturbation relative to the direction of field-aligned current is opposite between the F17 and F18 data in this case because the spacecraft are in different hemispheres, with F17 being in the south and F18 in the north. In each of the DMSP passes, the spacecraft first encounters a sharp ion precipitation boundary with 10s keV energy followed by a dispersed electron precipitation boundary. The ion boundary is accompanied by a field-aligned current into the ionosphere, marked by the slope in B_z in Figures 5.7e and 5.7h, and a current out of the ionosphere with an opposite B_z perturbation is measured with the electron precipitation boundary. These high-latitude particle boundaries and associated field-aligned currents correspond well with the features measured by Van Allen Probe A in the equatorial plane, despite the uncertainties involved in magnetic mapping.

An interesting feature in the DMSP data is the existence of multiple alternating field-aligned current structures between L = 3-5. With each change in slope of B_z, there are alternating regions of ion and electron precipitation. To this point in the paper, the SAPS region has been discussed in terms of a steady spatial separation between the plasma sheet ions and electrons, however, these data suggest that the region is composed of multiple layers of particle boundaries and alternating current structures. The Van Allen Probe A magnetic field data also support this view: there are multiple variations in the slope of B_x (Figure 5.7b) between L = 3.5-5 that are correlated with fluctuations in the electric field and particle pressure. These alternating current structures may be a series of incoming discrete injections from the tail related to the elevated substorm activity during this period (Figure 5.3e).

If we assume the DMSP data provide a snapshot of the spatial separation between successive injection fronts, and the Van Allen Probes data measure the injections passing over the relatively stationary spacecraft, we can estimate the propagation speed of the injection structures. The magnetic perturbations from DMSP are separated by approximately 1 R_E when mapped to the equatorial plane, and between L = 3.5-5 Van Allen Probe A measures magnetic field fluctuations with a period of ~2-4 minutes. This results in an earthward propagation speed of 25-50 km/s. Reeves et al. [1996] used dispersionless electron injection signatures from LANL and CRRES to estimate the radial propagation of the injections from L = 6.6 (geosynchronous orbit) to L = 5, and found an average earthward propagation speed of 24 km/s, which is consistent with our estimate.

The injections are initiated farther back in the tail, where magnetic reconnection launches a dipolarization front earthward with speeds of 200-500 km/s between 10-20 R_E [Runov et al., 2011]. Most dipolarization fronts slow down and stop at geosynchronous orbit or beyond [e.g., Sergeev et al., 2012], and they are not expected to penetrate inside the plasmasphere. The much slower propagation speeds from our study and Reeves et al. [1996] are consistent with earthward injections that are slowing down in the inner magnetosphere. By connecting the magnetic perturbations between the Van Allen Probes and DMSP, we suggest that the electric field pulse at L = 3.6, which is inside the plasmasphere, is the remnant of a dipolarization front, where the initial dipolarization in the magnetic field farther back in the tail evolves into a SAPS/SAID structure in the inner magnetosphere.

In addition to the radial spatial structure of the SAPS region revealed within a single DMSP pass (~10 min), the three DMSP spacecraft also show variation in the particle precipitation boundaries and field-aligned currents between successive passes close together in time and MLT. The data are consistent with a picture of multiple, narrow in MLT injections occurring on timescales of minutes, and the integrated effect producing a build-up of pressure, field-aligned currents, and the broad region of strong electric fields in the equatorial region. Recent studies have suggested that small-scale injections may be of equal or greater importance than large-scale convection in transporting plasma sheet particles into the inner magnetosphere based Van Allen Probes observations [Gkioulidou et al., 2014] as well as RCM-E simulations [Yang et al., 2015], and our observations support this view.

5.5 SAPS Impact

5.5.1 Plasmasphere Erosion

As was seen from the Van Allen Probes particle and electric field data (Figures 5.3-5.6), the inner edge of the plasma sheet ions penetrates inside the outer edge of the plasmapause at dusk, and the SAPS electric field can be enhanced partially inside the plasmasphere. Two consecutive Van Allen Probes duskside passes are shown in Figure 5.8, and the effect of the large electric fields inside the plasmasphere is apparent. We define the plasmapause as the most earthward location where the density drops below 50 cc. In Figure 5.8a, Van Allen Probe A observes a ~10 mV/m spike near L = 3.6 that was associated with a strong pressure gradient and a magnetic perturbation, and the plasmapause is located at L = 4.1 based on the gradient in spacecraft potential. Four hours later, Van Allen Probe B passes through the same spatial region, and the plasmapause has moved inward to the location of the previously observed large electric field spike.

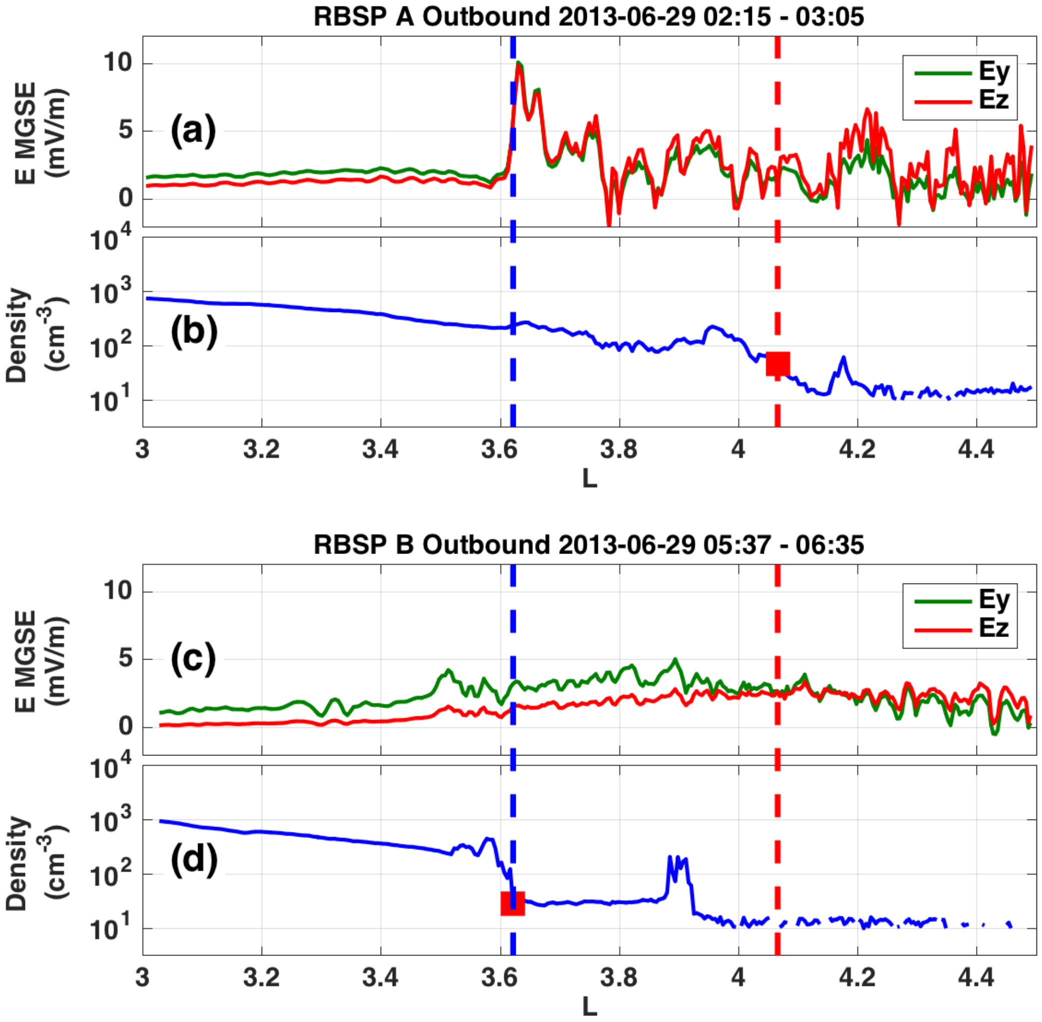

Figure 5.8: Consecutive outbound duskside passes from Van Allen Probes A and B showing strong electric fields and a subsequent inward motion of the plasmapause.

This is a direct example of the effect of the plasma sheet ions drifting through the outer edge of the plasmasphere, causing a large electric field that convects away the lower-energy particles and redefines the plasmapause at a lower L value. While plasmasphere erosion and the formation of plumes have historically been explained by variations in the strength of the convection electric field, this example shows a clear correlation between localized electric fields on the dusk side and changes in the plasmapause, adding further evidence that SAPS should not be ignored in basic descriptions of magnetospheric electric fields and plasmasphere dynamics [e.g., Goldstein et al., 2003]. The connection between SAPS and plasmasphere erosion is important due to the impact the plasmasphere has on the coupled magnetospheric system, including the propagation of waves that affect the loss and energization of radiation belt electrons.

5.5.2 Particle Energization

The same electric field spike that was related to plasmapause motion in the previous section is also correlated with flux enhancements in the higher-energy ion and electron populations. Figure 5.9 shows the electric field along with ion and electron fluxes for selected energies from MagEIS. Across the ~10 mV/m electric field spike, the ions display flux increases of 1-2 orders of magnitude between 30 keV (not shown) and 170 keV (Figure 5.9b). Shortly after the large electric field is observed, there is an enhancement in 200 keV to 1 MeV electron flux and a decrease in 50-80 keV flux. A detailed analysis of the relationship between the electric field pulse and the energetic particle response is outside of the scope of this paper, but the correlation between SAPS and 100s keV electrons is interesting and will the subject of a future study.

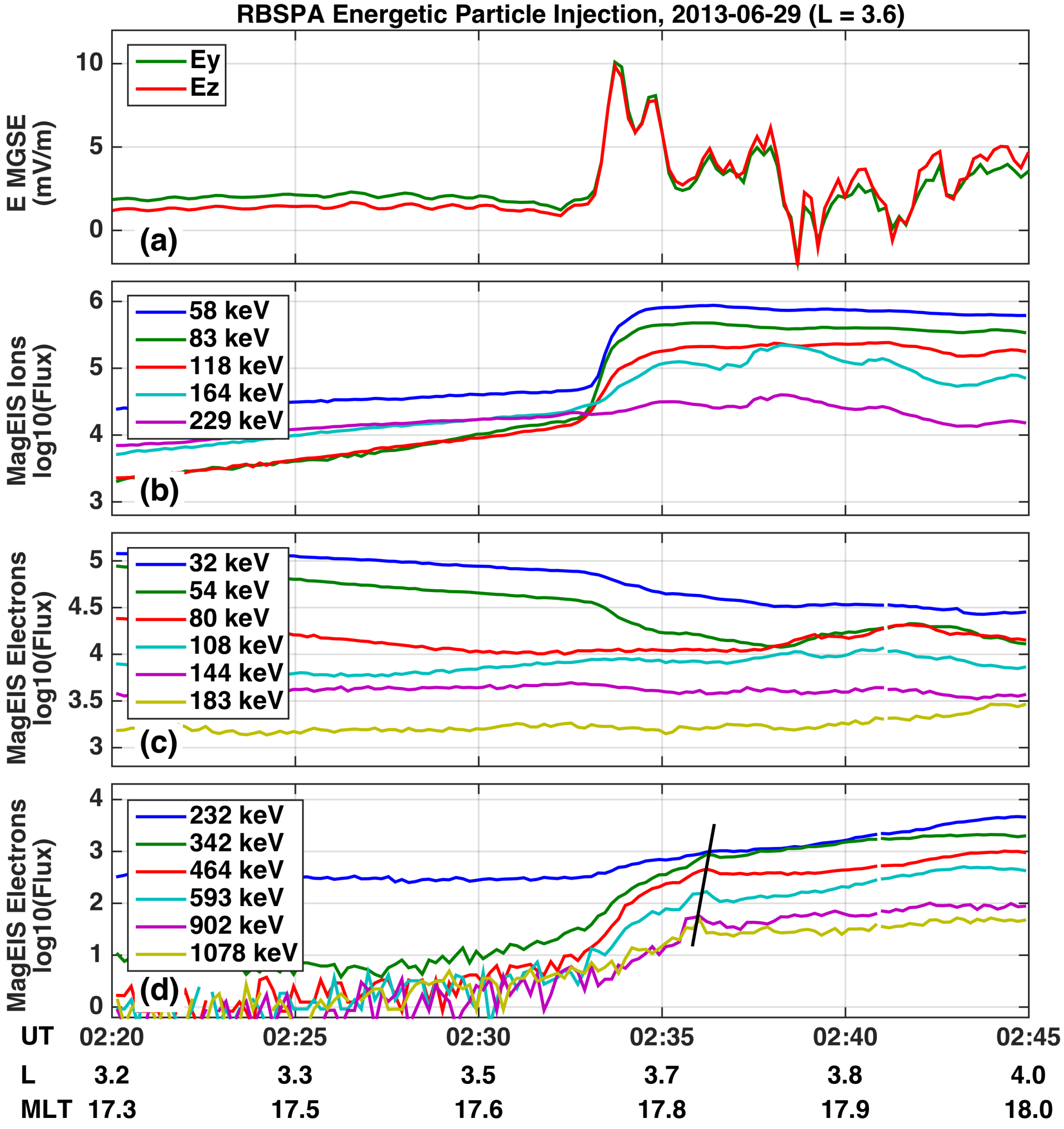

Figure 5.9: A large-amplitude electric field spike from EFW on Van Allen Probes A (a) with corresponding ion (b) and electron (c-d) fluxes from MagEIS. The black line in panel (d) shows a dispersed electron injection signature.

5.6 Summary

This study shows observations of the particles and fields associated with SAPS during an extended period of southward IMF during the 29 June 2013 geomagnetic storm. Overall, the major aspects of the traditional SAPS description were observed in relation to the strong electric fields measured by the Van Allen Probes. Near dusk, plasma sheet ions contributed to increased pressure in the inner magnetosphere, causing field-aligned currents to flow into the ionosphere. The plasma sheet electron boundary was observed to be radially outward from the ion boundary both at the equatorial plane and at high latitudes, and consequently the keV electron precipitation boundary in the ionosphere was located at a higher latitude than the field-aligned current associated with the ions. This spatial arrangement lead to a current closing through a low-conductivity region, resulting in a strong electric field that mapped back to the equatorial magnetosphere.

Although most of the observations were in agreement with the traditional SAPS picture, there were cases of enhanced electric fields earthward of the inner edge of the plasma sheet ions ($L < 2.5$) that are examples of long-duration penetration electric fields. Also, the ion inner edge was consistently identified in the Van Allen Probes data and was observed to move earthward throughout the storm, but the equatorial plasma sheet electron boundary was not as clear in two of the four passes. The outer boundary of the SAPS region corresponded to the inner boundary of 5 keV electrons in the first two passes, however, the 5 keV electron boundary was not observed in the last two passes. We suspect that the difference may be related to magnetic mapping.

The combination of the equatorial Van Allen Probes and high-latitude DMSP spacecraft showed that the SAPS region can be characterized as a broad spatial region persisting for hours that also contains significant small-scale spatial and temporal variation within. We interpret multiple variations in the magnetic field data as earthward propagating spatial structures separated by ~1 R_E in the equatorial plane with speeds between 25-50 km/s. These features may be the earthward extent of substorm-related dipolarization fronts slowing down and piling up in the inner magnetosphere, resulting in the integrated effect of a large pressure gradient at the inner edge of the plasma sheet ions. We also showed that a SAPS does penetrate inside the plasmasphere, and that there may be a relationship between SAPS electric fields and 100s keV electron enhancements at low L shells in the inner magnetosphere.

Chapter 6: Electric Fields and 100s keV Electron Dynamics

The Van Allen Probes have reported frequent flux enhancements of 100s keV electrons in the slot region, with lower-energy electrons exhibiting more dynamic behavior at lower L shells. Also, in situ electric field measurements from Combined Release and Radiation Effects Satellite (CRRES), Time History of Events and Macroscale Interactions during Substorms (THEMIS) and the Van Allen Probes have provided evidence for large-scale electric fields at low L shells during active times. We study an event on 19 February 2014 where 100s keV electron fluxes were enhanced by orders of magnitude in the slot region and electric fields of 1-2 mV/m were observed below L = 3. Using a 2-D guiding center particle tracer and a simple large-scale convection electric field model, we demonstrate that the measured electric fields can account for energization of electrons up to at least 500 keV in the slot region through inward radial transport. This work has been recently submitted to the Journal of Geophysical Research Space Physics [Califf et al., 2016b].

6.1 Introduction

Recent observations by the Magnetic Electron Ion Spectrometer (MagEIS) [Blake et al., 2013] onboard the Van Allen Probes have highlighted the dynamic nature of 100s keV electrons at low L shells in the inner magnetosphere [e.g., Zhao et al., 2014; Turner et al., 2015; Reeves et al., 2016]. The quiet-time structure of the radiation belts consists of an inner belt (L < ~2.5), an outer belt (L > ~3.5), and a slot region (~2.5 < L < ~3.5) that contains fewer energetic electrons. The structure of the slot region is energy dependent, with the outer edge of the inner belt extending to larger L shells for lower energies.

Frequently during storms, the 100s keV electron flux increases by orders of magnitude at low L shells (L < 3), sometimes filling the slot region to the point that there is no clear distinction between the inner and outer belts.

Figure 6.1 shows MagEIS spin-averaged electron fluxes for energies between 169-731 keV sorted by L shell from June 2013 to October 2014. For electron flux plots in this study, we use McIlwain L computed from the OP-77 magnetic field model, which is provided in the MagEIS level 2 and level 3 data. The outer radiation belt is more dynamic than the inner belt, and the inner belt is mostly composed of relatively lower-energy electrons. Many of the variations in the outer belt extend to L = 3 or below, and some enhancements appear to connect the inner and outer belts, filling the slot region. These slot filling events occur frequently for lower energies, but become much less common for electrons above ~500 keV.

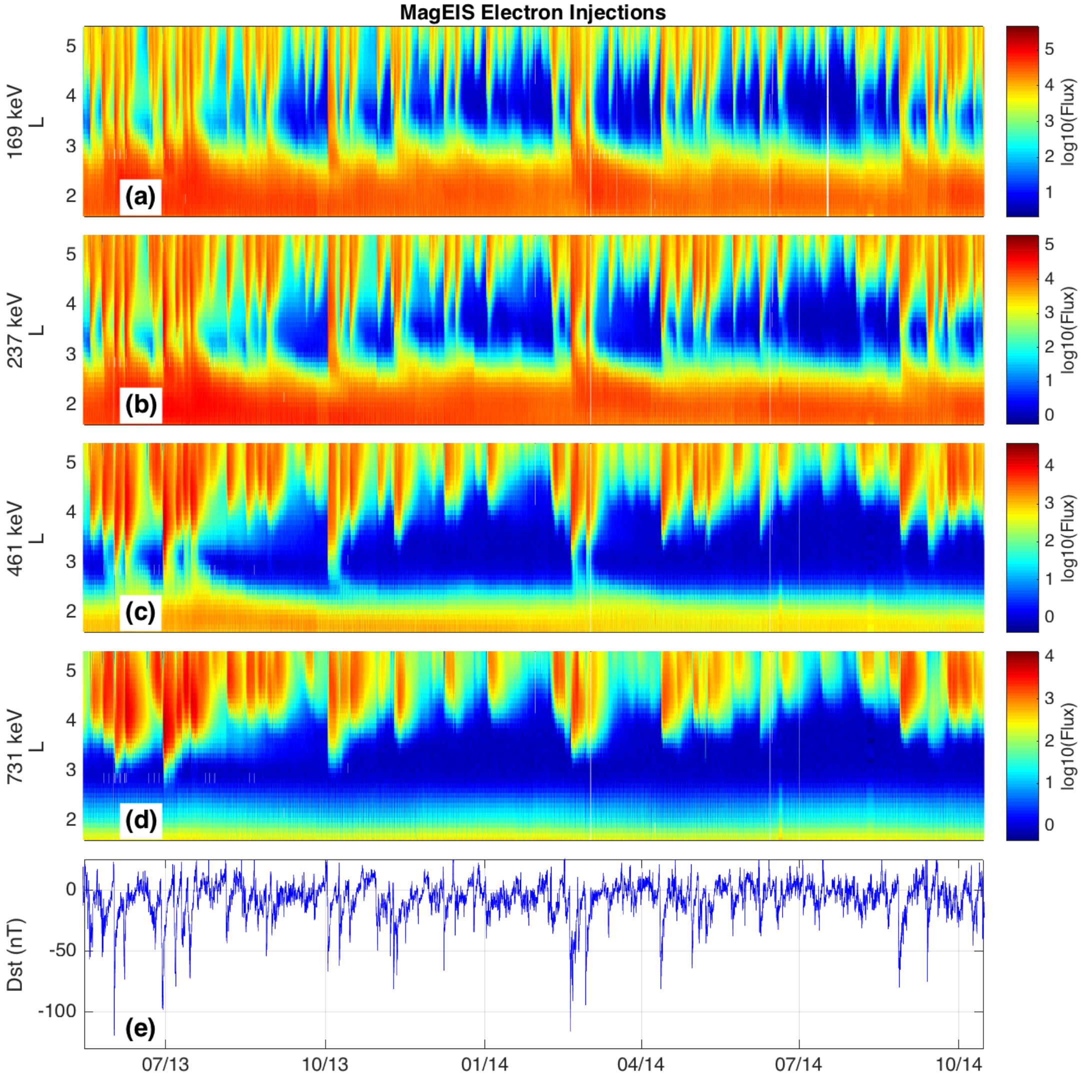

Figure 6.1: Spin-averaged fluxes for electrons between 169-731 keV (a-d) measured by both Van Allen Probes and (e) the Dst index from May 2013 to October 2014.

Spin-averaged fluxes for 169-731 keV electrons at specific L shells are plotted for a series of events between June 2013 and November 2014 in Figure 6.2. Flux enhancements of an order of magnitude or more are common at L = 3 for 169 keV electrons, and for a given energy, the flux is more variable at higher L shells. The enhancements are characterized by a fast rise phase followed by a slow decay: the rise phase corresponds to the period where the energization mechanism is dominating loss, and the decay is likely caused by slow pitch angle scattering from plasmaspheric hiss [e.g., Lyons and Thorne, 1973].

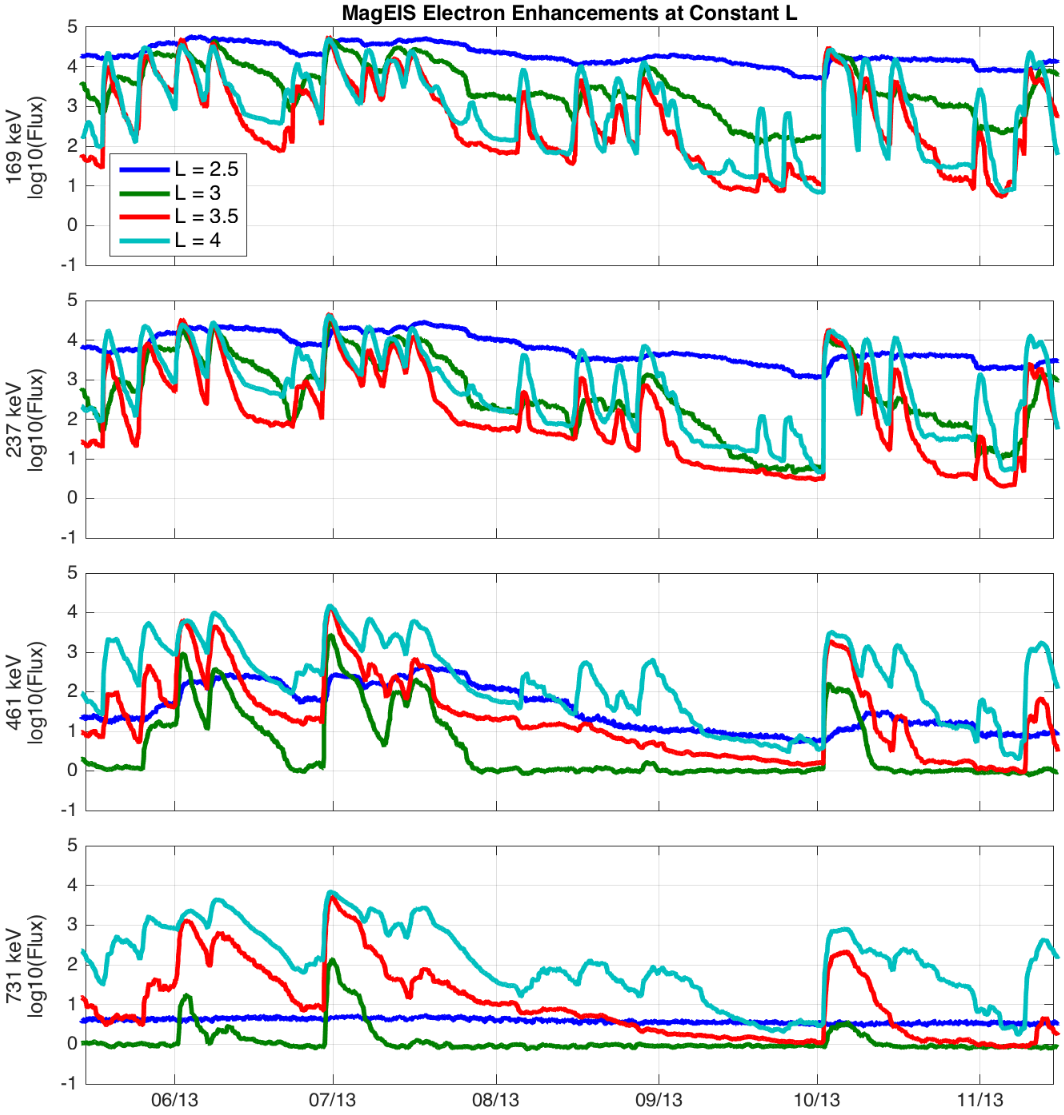

Figure 6.2: Spin-averaged fluxes at specific L shells from June to November 2013.

We are focused on electric fields during the rise phase of the enhancements in order to investigate the mechanism that is energizing 100s keV electrons at low L shells. Radiation belt electron energization is typically discussed in terms of radial transport and local acceleration. If a particle is transported radially inward and the first adiabatic invariant is conserved, the particle will gain energy as the magnetic field strength increases. The electric field is important in this scenario because inward radial transport across magnetic field lines requires an azimuthal electric field.

Local acceleration by chorus has been identified as a mechanism for energizing electrons to MeV energies [e.g., Reeves et al., 2013], but there is ongoing debate over the effect chorus may have on 100s keV electrons. Some authors expect chorus to primarily cause loss for 100s keV electrons [e.g., Shprits et al., 2008], while others have attributed 100s keV electron enhancements to acceleration by chorus [e.g., Thorne et al., 2007].

In situ measurements by CRRES, THEMIS and the Van Allen Probes have demonstrated that large-scale electric fields of up to a few mV/m can exist below L = 3 during storms [e.g., Rowland and Wygant, 1998; Califf et al., 2014, 2016a; Thaller et al., 2015]. Some of the mechanisms that can generate enhanced electric fields deep within the inner magnetosphere include penetration electric fields, subauroral ion drifts (SAID), subauroral polarization streams (SAPS), substorm injections, and interplanetary shocks. The purpose of this study is to investigate the relationship between 100s keV electron enhancements in the slot region and large-scale electric fields at low L shells.

Recently, Su et al. [2016] modeled inner belt electrons under the influence of various Kp-driven electric field models for the 17 March 2013 storm. They found that the low-L electric fields required to reproduce observed flux enhancements at L = 1.5 were stronger than any existing model. This study applied a 2-D guiding center code to electrons with $\mu = 2.5$ MeV/G, which roughly corresponds to 350 keV at L = 1.5 and 35 keV at L = 4.4. Selesnick et al. [2016] also showed that rapid injections of 100s keV electrons below L = 2 during the 22-23 June 2015 storm could be caused by a 5 mV/m convection electric field, however they were unable verify this electric field with in situ measurements due to uncertainties related to **vxB** subtraction near perigee.

We study an event on 19 February 2014 where flux enhancements for 100s keV electrons were observed below L = 3 by the Van Allen Probes. Electric field and plasmapause measurements by the Van Allen Probes and THEMIS E provide direct evidence of large-scale electric fields at low L shells during the event. We model the evolution of electron phase space density (PSD) over a range of energies using a 2-D guiding center particle tracer and a simple uniform dawn-to-dusk electric field to demonstrate that the observed electric fields are sufficient to explain the slot region electron enhancements.

6.2 Event Overview

On 18 February 2014, the interplanetary magnetic field (IMF) turned southward, initiating a geomagnetic storm with minimum Dst = -116 nT. The main phase of the storm was separated into two phases: Dst began to recover near 02 UT on 19 February 2014, and then an abrupt increase in solar wind speed and further southward turning of the IMF due to a coronal mass ejection (CME) extended the main phase until the IMF turned sharply northward at 08 UT. Large flux enhancements for 100s keV electrons were observed in the slot region at the beginning of the recovery phase. Figure 6.3 shows the solar wind data and geomagnetic indices during this storm.

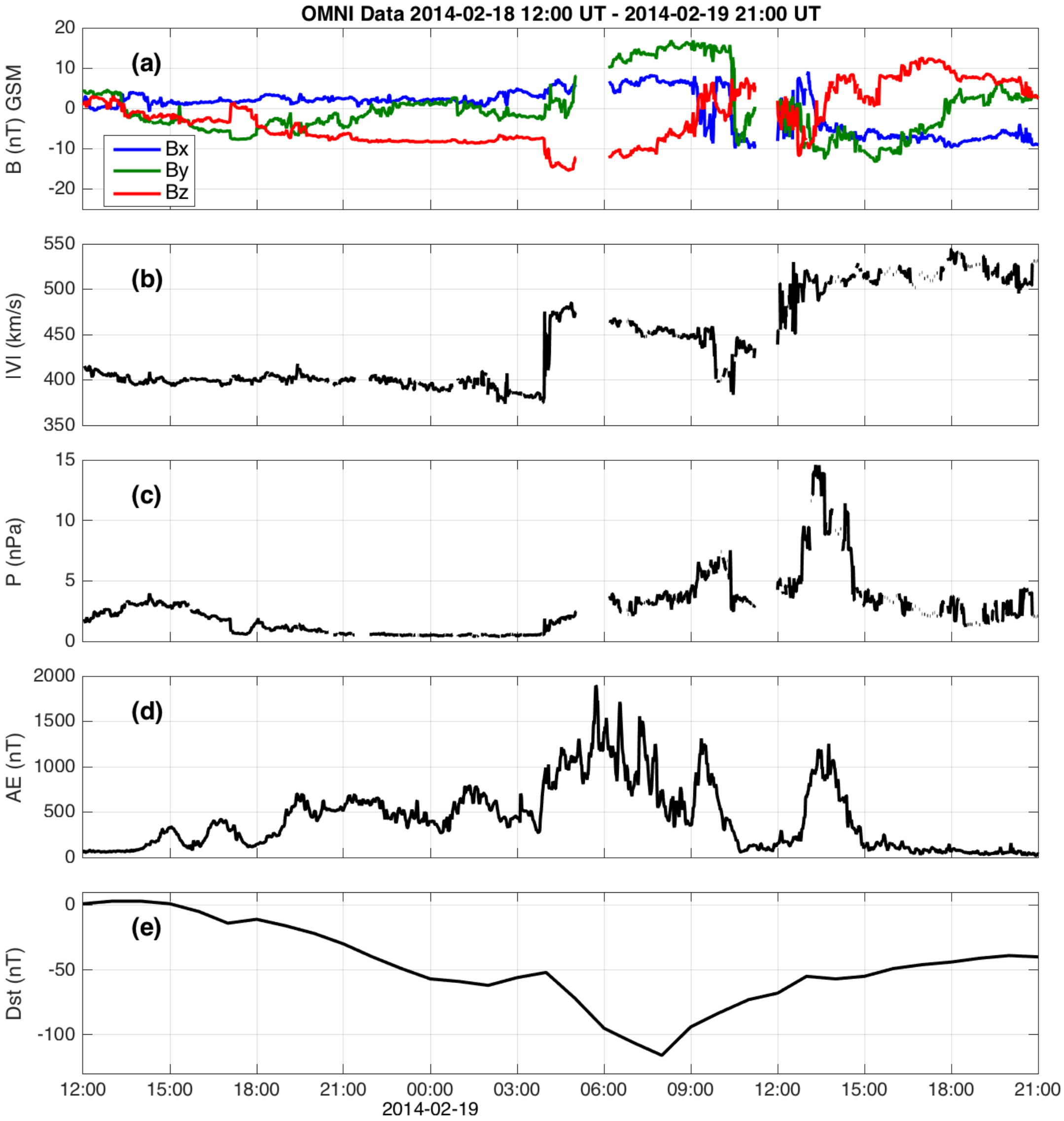

Figure 6.3: Solar wind data and geomagnetic indices for the 19 February 2014 geomagnetic storm. (a) Interplanetary magnetic field, (b) solar wind speed, (c) flow pressure, (d) AE index, and (e) Dst index.

Spin-averaged electron fluxes observed by the Van Allen Probes over the course of the event are shown in Figure 6.4. Flux is plotted against L shell, and the time of each observation is displayed in color. Flux enhancements of more than 2 orders of magnitude were observed for electrons with energies below 350 keV at L = 3, and 900 keV electrons were enhanced near L = 3.5. The initial observations (blue lines) display a typical inner belt, outer belt and slot region structure, with the outer edge of the inner belt extending to larger L shells for lower energies. During the enhancement, the inner edge of the outer belt moved earthward over the course of ~10 hours until the outer belt effectively merged with the inner belt for energies below 350 keV. The apparent gradual inward movement of the inner edge of the outer belt is common in slot filling events.

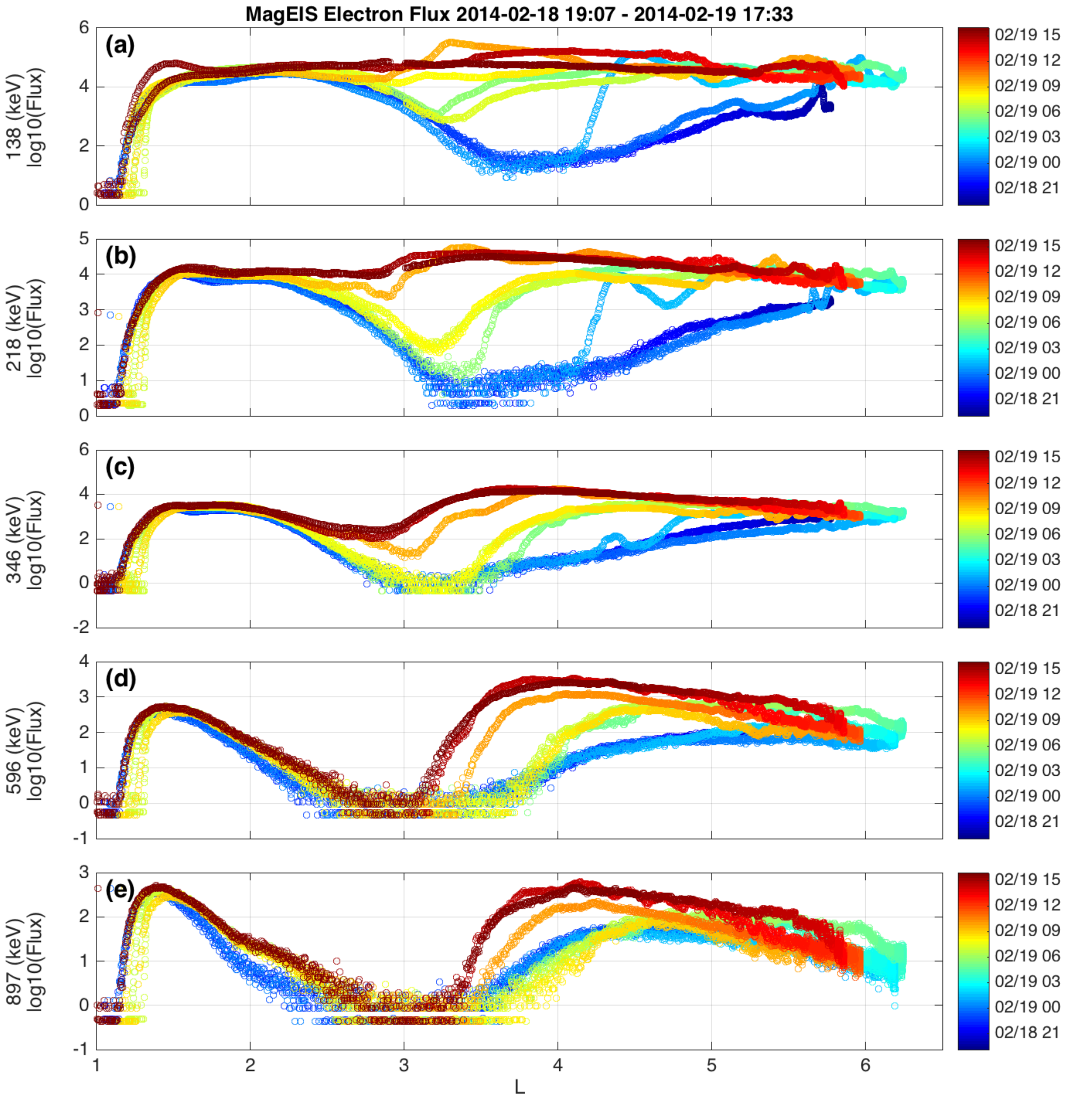

Figure 6.4: Spin-averaged electron flux profiles sorted by L shell during the 19 February 2014 geomagnetic storm for (a) 138 keV, (b) 218 keV, (c) 346 keV, (d) 596 keV and (e) 897 keV. Time is plotted in color.

6.3 Flux and Phase Space Density (PSD) Evolution

We have identified two outbound Van Allen Probes passes on 19 February 2014 where the 100s keV electron flux increased by more than an order of magnitude at low L shells over ~1.5 hours. In order to evaluate the relationship between large-scale electric fields and the electron dynamics, we converted flux to PSD as a function of the three adiabatic invariants, μ, K and L* [e.g., Green and Kivelson, 2004]. A 100 keV equatorially-mirroring electron corresponds to μ = 10 MeV/G at L = 3 in a dipole field, and if μ is conserved, the energy would be 15 keV for the same electron at L = 6. Therefore, complete radial profiles (L ~ 2-6) for lower μ values require combined data from the Helium, Oxygen, Proton, and Electron Mass Spectrometer (HOPE) (1 eV to 50 keV) [Funsten et al., 2013] and MagEIS (30 keV to 4.8 MeV).

The flux data are provided at fixed pitch angles and energies, which do not correspond to fixed μ and K. In order to create profiles for constant μ and K, multiple levels of interpolation were required. First, measured fluxes at each pitch angle were converted to PSD for each energy channel. This resulted in a PSD distribution for each pitch angle corresponding to an irregular grid in μ. Next, we interpolated the PSD to a constant μ grid at each pitch angle. This step was performed separately for HOPE and MagEIS because the level 3 data for the two instruments are provided at different pitch angle intervals. Then a set of pitch angles was calculated using the TS04 magnetic field model [Tsyganenko and Sitnov, 2005] corresponding to a fixed grid of K values, and the interpolated PSD at fixed μ was interpolated to the computed pitch angle grid.

After interpolating the PSD to constant μ and K, we chose values for μ and K that have complete coverage across L shells for both passes. K = 0 ($G^{1/2}R_E$) corresponds to equatorially mirroring particles, which cannot be measured when the spacecraft is located off the magnetic equator. We selected K = 0.1 ($G^{1/2}R_E$) to obtain complete radial PSD profiles, which corresponds to electrons with equatorial pitch angles of ~45 deg.

Figure 6.5 shows the electron flux and PSD profiles measured by the two Van Allen Probes. Flux is plotted against McIlwain L, and PSD is plotted against L*. Van Allen Probe B passed L = 3 at 07:52 UT and Van Allen Probe A passed L = 3 at 09:33 UT. The minimum hourly Dst of -116 nT was recorded at 08:00 UT, so these observations occur near the beginning of the recovery phase of the storm. The flux profiles exhibit a large increase below L = 3 for electrons up to 350 keV between the two passes.

The PSD profiles in Figure 6.5 panel (b) correspond to roughly the same energies as the fluxes in Figure 6.5 panel (a) for 90 degree pitch angle electrons at L* = 3.5. When sorted by PSD coordinates, the enhancements appear to be more organized, with a sharp gradient in PSD that moves radially inward between observations. Local peaks in PSD have been used to identify local acceleration processes [e.g., Green and Kivelson, 2004]. The absence of local peaks in Figure 6.5 suggests that the flux enhancements were caused by inward radial transport, where the first and second adiabatic invariants are conserved.

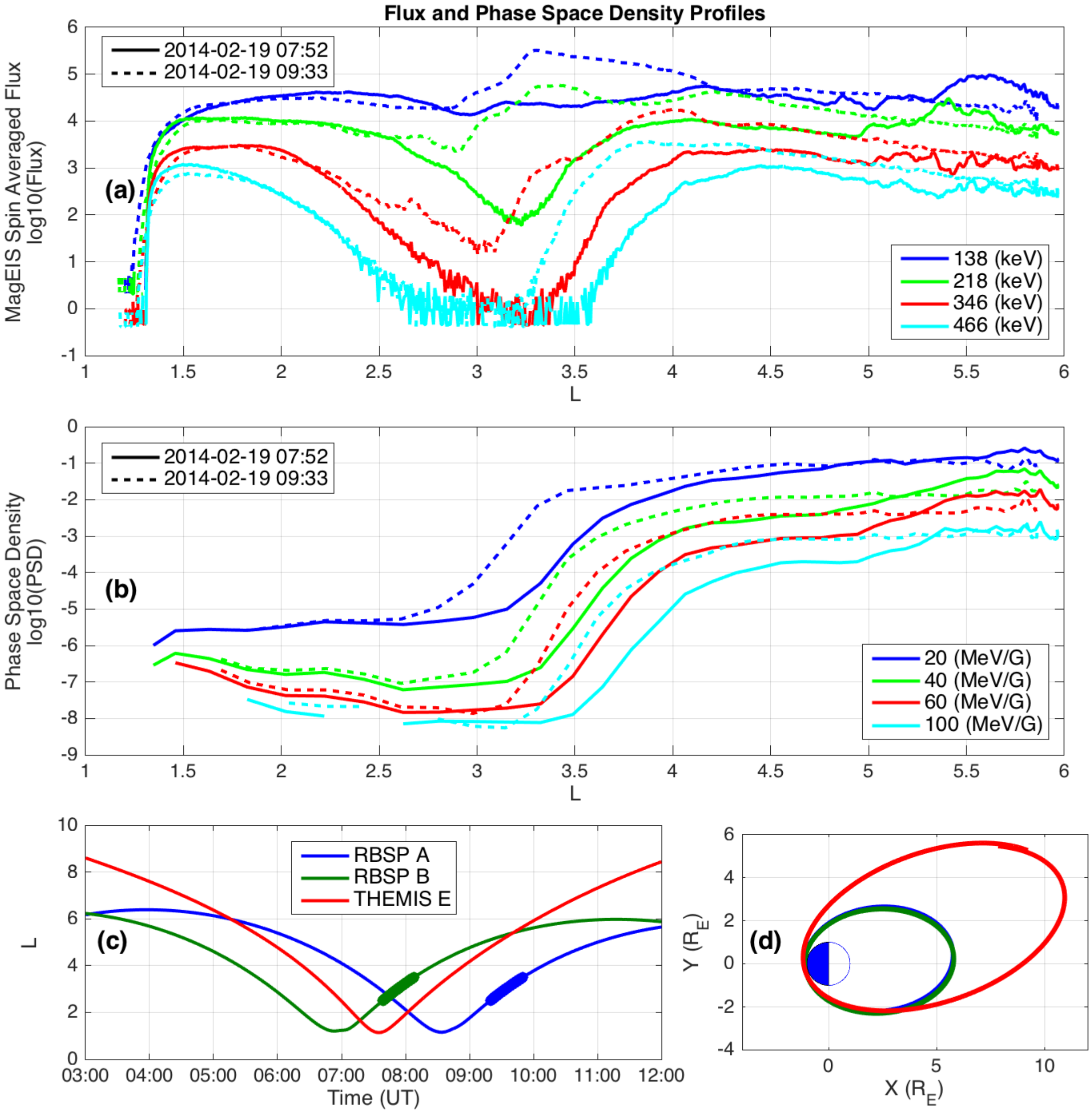

Figure 6.5: Spin-average flux (a) and PSD (b) evolution between successive outbound Van Allen Probes passes on 19 February 2014. The L sampling (c) and orbits projected into the GSE XY plane (d) for the Van Allen Probes and THEMIS E.

The PSD profiles in Figure 6.5 show a steep radial gradient that is located at higher L for higher μ. Between observations separated by ~1.5 hours, the location of the steep PSD gradient moves inward by ~0.3 L. This demonstrates that a relatively small inward displacement of the preexisting electron population can create a dramatic change in the flux profile, especially in the slot region where fluxes are initially low. The PSD profiles suggest inward transport as a mechanism, raising the question: were there enhanced electric fields in the slot region that could have transported the electrons?

6.4 Electric Field and Plasmapause Observations

The flux enhancements near L = 3 under study occurred between 07:52 UT and 09:33 UT on 19 February 2014, which correspond to an outbound Van Allen Probe B and an outbound Van Allen Probe A pass, respectively. The Van Allen Probes crossed through L = 3 near dusk on the inbound pass and dawn on the outbound pass. Between the flux enhancement observations, THEMIS E passed through the inner magnetosphere across similar local times as the Van Allen Probes, providing an additional set of electric field measurements. The Van Allen Probes and THEMIS E orbits are shown in Figure 6.5d along with the times of inbound and outbound L sampling (Figure 6.5c) for each spacecraft on 19 February 2014.

Figure 6.6 shows data from both Van Allen Probes on inbound duskside passes prior to the flux enhancement. Beginning at ~04 UT, Van Allen Probe B observed an elevated dawn-dusk (+Ey) electric field of approximately 1 mV/m spanning from L = 6 to below L = 2 on the dusk side (blue line, Figure 6.6a). Measurements from Van Allen Probe A, which was trailing Van Allen Probe B by ~1.5 hours, display similar duskside electric fields until at least 08 UT (green line, Figure 6.6a). There are variations on top of an average positive Ey, with larger variations at higher L shells. The electric field data were provided by the EFW instrument [Wygant et al., 2013], and spacecraft **vxB** and the co-rotation electric field have been subtracted, leaving the electric field in the frame co-rotating with Earth. The Modified Geocentric Solar Ecliptic (MGSE) coordinate system is defined by the spacecraft spin-configuration and is similar to Geocentric Solar Ecliptic (GSE) coordinates: MGSE Y lies in the spin plane and is approximately aligned in the dawn-to-dusk direction.

At ~04 UT, the plasmapause can be inferred to be located near L = 5.8 by both the radial gradient in spacecraft potential (and density) (blue lines, Figure 6.6b and c) and the presence of plasmaspheric hiss (Figure 6.6d) measured by Van Allen Probe B, which is identified by the broadband wave power between 100-1000 Hz [Malaspina et al., 2015]. The density (Figure 6.6c) is derived from spacecraft potential [Kurth et al., 2015], and the spectral data (Figure 6.6d) are combined from the Electric and Magnetic Field Instrument Suite and Integrated Science (EMFISIS) Waveform Receiver (WFR) (10 Hz to 12 kHz) and High Frequency Receiver (HFR) (10 to 500 kHz) [Kletzing et al., 2013].

Approximately 1.5 hours later, Van Allen Probe A passed though the duskside inner magnetosphere, and similar 1 mV/m electric fields were observed extending to low L shells with more variation at higher L shells (green line, Figure 6.6a). Also, the reduced plasmaspheric hiss amplitudes suggest that the plasmapause moved earthward inside L = 5 near 06:22 UT. Note that the data are plotted against L shell, but they are sampled from higher to lower L on the inbound pass, so the time increases from right to left on the plot. The disruption in the hiss signature near L = 5 may indicate that the plasmapause moved inward faster than the spacecraft (Figure 6.6e). The higher densities measured outside of L = 5 were sampled earlier in time, so it is possible that the actual density after 06:22 UT beyond L = 5 is lower than what is shown on the plot.

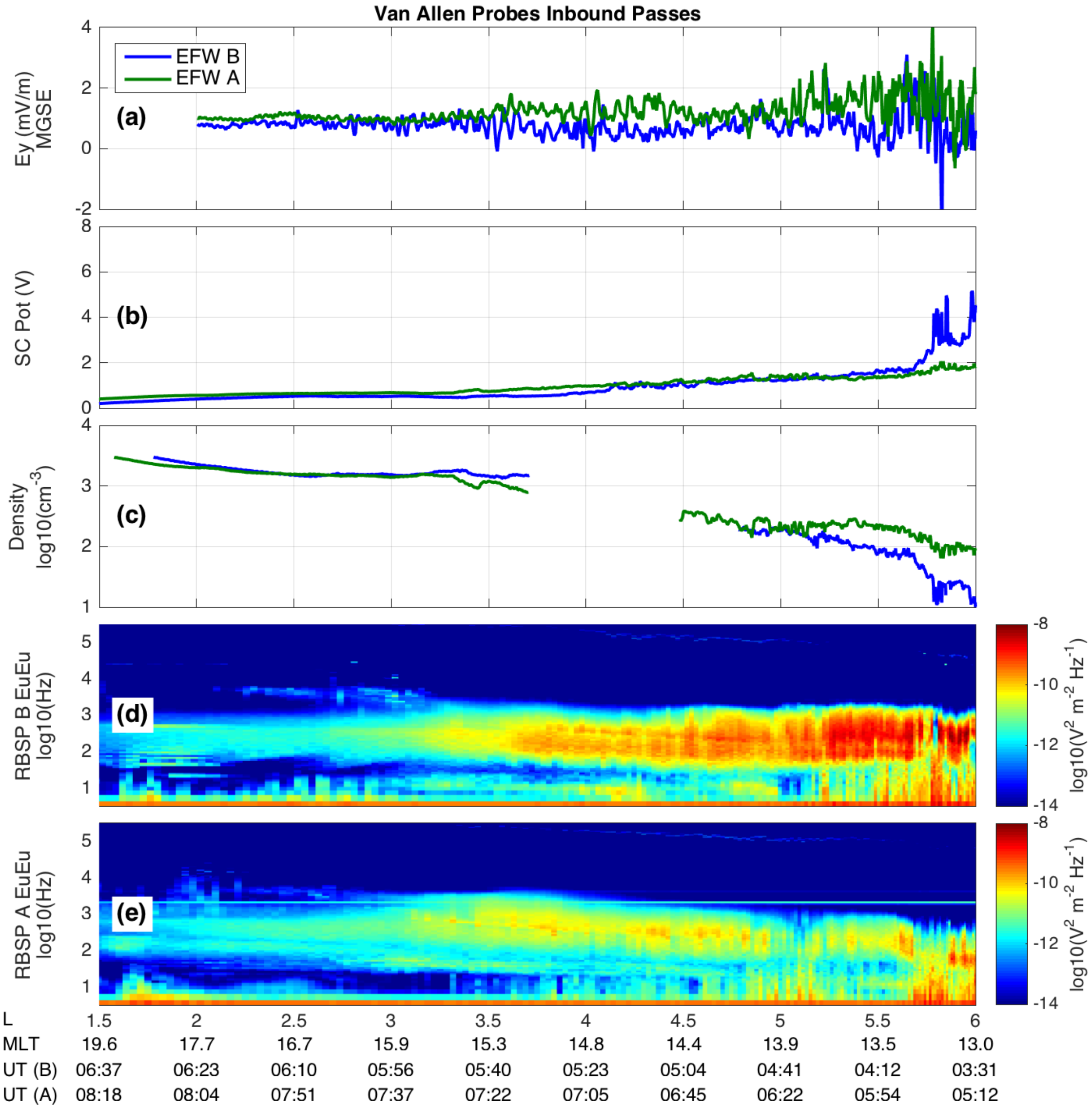

Figure 6.6: Inbound passes for both Van Allen Probes sorted by L shell (UT increases from right to left). (a) Electric field MGSE Y measurement in the frame co-rotating with Earth, (b) spacecraft potential, (c) density derived from spacecraft potential, (d) combined EMFISIS WFR and HFR electric field wave power from Van Allen Probe B, and (e) electric field wave power from Van Allen Probe A.

Figure 6.7 displays the consecutive outbound Van Allen Probes passes on the dawn side that revealed a large increase in flux for 100s keV electrons in the slot region. Both spacecraft measured small positive or possibly even negative quasi-static electric fields across most of the dawn side, in contrast to the positive 1 mV/m dawn-dusk electric fields on the dusk side. Similar dawn-dusk asymmetry in the electric field with stronger electric fields near dusk has been reported in statistical data during active times [e.g., Califf et al., 2014].

The data in Figure 6.7 show a dramatic difference in the plasmapause location compared to the previous inbound pass on the dusk side (Figure 6.6). The gradient in spacecraft potential (and density) indicates that the plasmapause was located near L = 2.2 at 07:30 UT, and was below L = 2 at 09 UT (Figure 6.7b-c). This interpretation is also supported by the lack of plasmaspheric hiss outside of L = 2, the existence of chorus (~10 kHz) starting at L = 2 and the broadband electrostatic waves below 100 Hz. Chorus waves can only propagate efficiently outside the plasmapause, and broadband electrostatic waves have been associated with the plasmapause boundary [Malaspina et al., 2015].

The dynamics of the plasmasphere are driven by large-scale electric fields [e.g., Goldstein et al., 2003], so the inward motion of the plasmapause to L < 2 provides further evidence of enhanced large-scale electric fields extending to low L shells. Electric field measurements by the spacecraft only occur at specific local times, and the radial profile is sampled over hours, so these measurements alone cannot definitively distinguish between localized and large-scale features in time and space. However, when placed in the context of statistical electric field measurements [e.g., Califf et al., 2014], the in situ measurements suggest a large-scale convection pattern across a wide range of L shells persisting for at least 1.5 hours, and the plasmapause observations add confidence to this interpretation. Inward plasmapause motion is commonly observed during slot-filling events, suggesting that the electric field responsible for eroding the plasmasphere may also be responsible for transporting 100s keV electrons into the slot region.

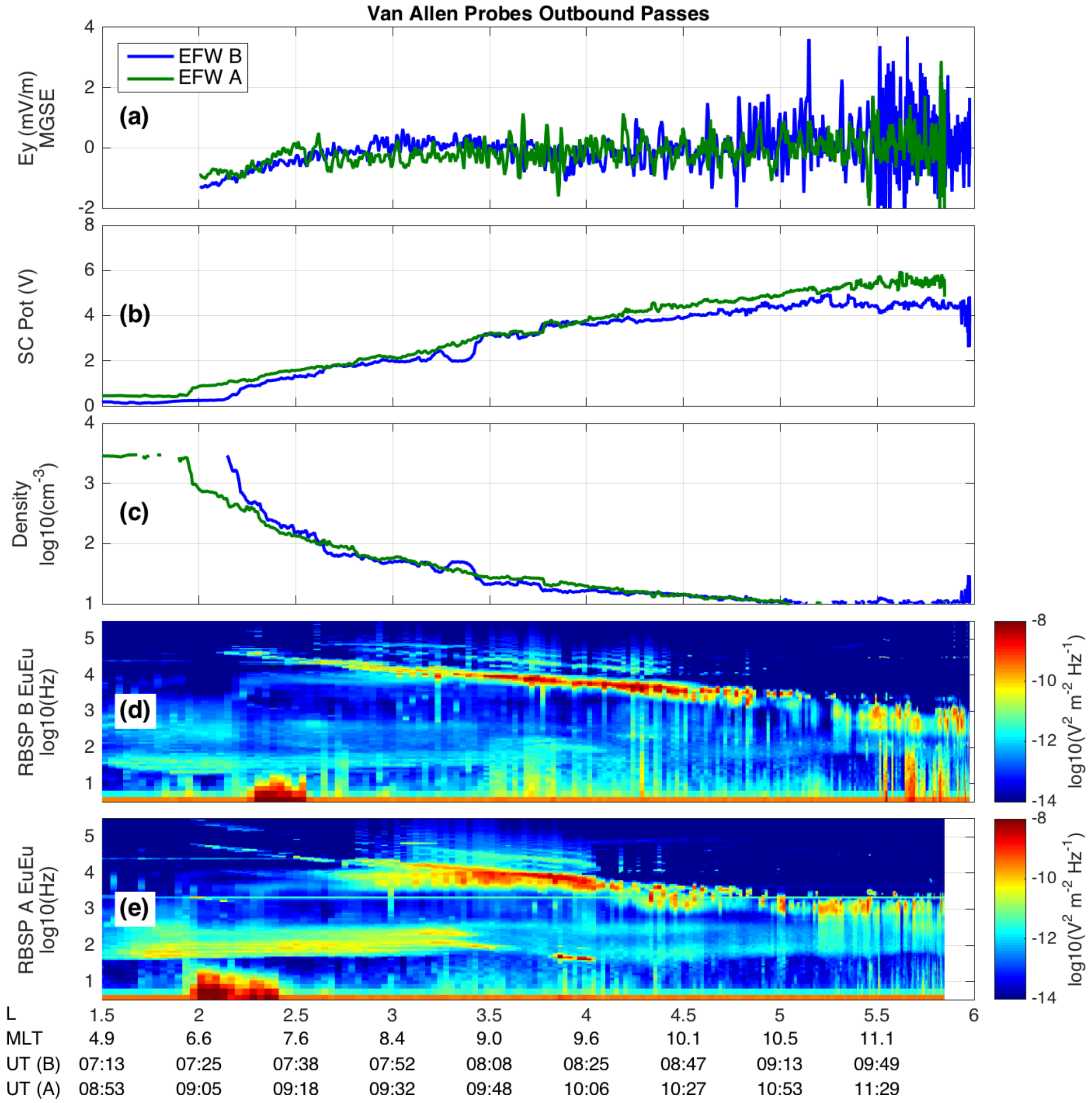

Figure 6.7: Outbound passes for both Van Allen Probes sorted by L shell in the same format as Figure 6.6.

Electric field data from THEMIS E are plotted in Figure 6.8 spanning the time period between the Van Allen Probes electron flux observations. Spin-fit data are shown from the electric field instrument (EFI) in the Despun L-vectorZ (DSL) coordinate system with spacecraft **vxB** and the co-rotation electric field subtracted [Bonnell et al., 2008]. DSL Y points in the dawn-to-dusk direction projected into the spin plane, which is within ~10 degrees of the GSE XY plane. The inbound THEMIS E pass shows a 2 mV/m dawn-dusk electric field across the duskside inner magnetosphere extending below L = 3 (Figure 6.8a) in agreement with the Van Allen Probes measurements in Figures 6 and 7. Also, the dawn-dusk asymmetry is apparent in the THEMIS E data with electric fields of ~0.5 mV/m on the dawnside outbound pass (Figure 6.8b).

A negative deviation in Ey of -1 mV/m was observed by THEMIS E and both Van Allen Probes below L = 2.5 on the dawn side. There is increased uncertainty in the electric field measurement at low L shells due to **vxB** subtraction errors. Due to the similar orbital trajectories for the Van Allen Probes and THEMIS E, it is unclear whether these measurements are real or are a result of a common **vxB** subtraction error between the three spacecraft. Above L = 3 the measurements are much more reliable: spacecraft **vxB** is only ~5 mV/m at L = 3, and a conservative 5% scale factor error would only introduce 0.25 mV/m **vxB** subtraction error, which is much smaller than the observations of 1-2 mV/m electric fields.

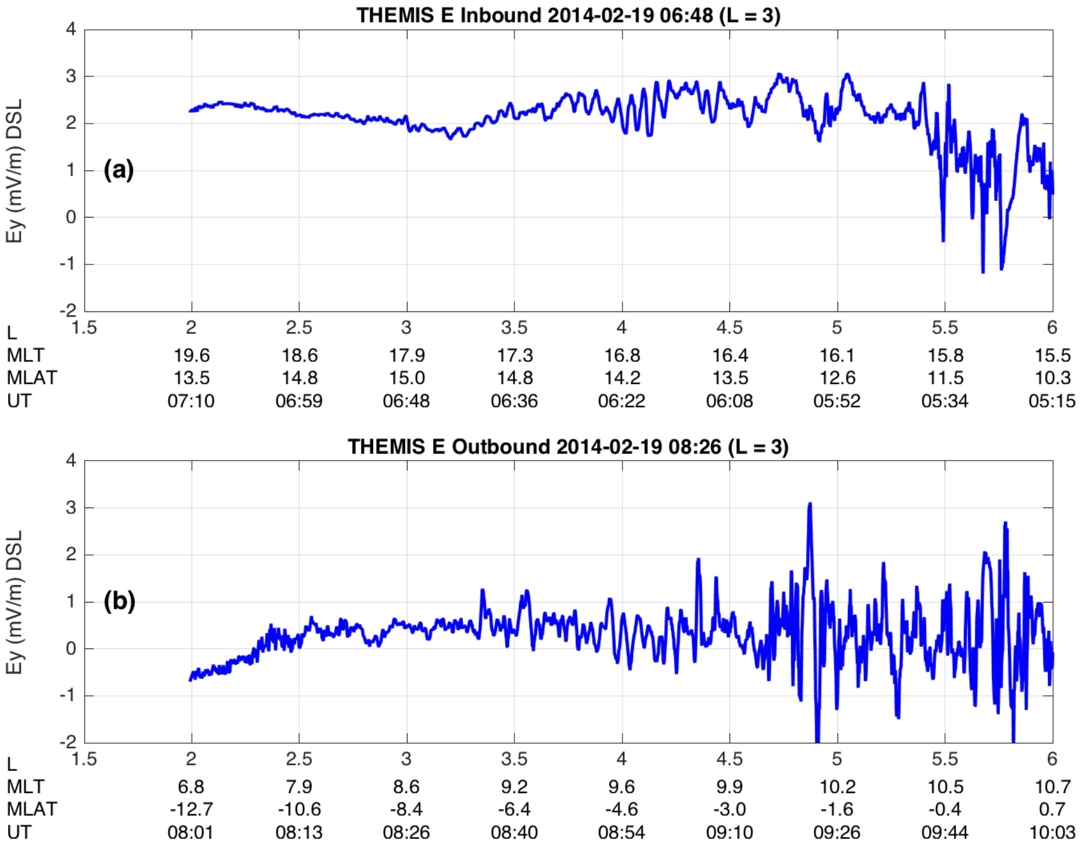

Figure 6.8: THEMIS E (a) inbound and (b) outbound electric field DSL Y measurements surrounding the flux enhancements observed by the Van Allen Probes.

6.5 Connection between the Measured Electric Fields and Electron Flux Enhancements

The PSD profiles in Figure 6.5 suggest that the slot region flux enhancements were caused by inward radial transport, and the electric field and plasmapause data in Figures 6.6-6.8 show that there were 1-2 mV/m electric fields at low L shells during the same time period. Next we evaluate the whether these electric fields are capable of transporting 100s keV electrons inward to create the observed flux enhancements.

6.5.1 Initial Assessment of the Required v. Measured Electric Fields

If we assume that the electrons moved steadily earthward during the entire 1.5-hour interval between observations, we can calculate the electric field required to transport the particles by

$$\boldsymbol{E} = -\boldsymbol{vxB}$$

(Eq. 6.1)

Assuming a dipole magnetic field and a purely azimuthal electric field, an electric field of 0.25 mV/m is needed to move the particles by 0.3 L over 1.5 hours at L = 3.5, and at L = 3, a 0.4 mV/m would be required. The in situ measurements presented in Figures 6.6-6.8 show 1-2 mV/m electric fields inside L = 3. The required electric fields are also reasonable given the typical electric field measurements during storms: statistical averages show that there can be ~0.5 mV/m below L = 3 during moderate storms, and the electric field can be as large as a few mV/m during the strongest storms [e.g., Califf et al., 2014]. It is also possible that the electron PSD profile changed more abruptly during a short interval between observations, requiring a stronger electric field.

6.5.2 Quantitative Modeling Based on a Simple Convection Electric Field Model

We developed a particle tracer to test the idea that a simple enhancement in the large-scale convection electric field could cause the observed inward transport for 100s keV electrons in the slot region. Radiation belt electrons are not normally associated with the convection electric field because high-energy electrons (> 1 MeV) drift around the Earth in only a few minutes, so slow changes in the large-scale potential structure have little net effect on the radial location. Radial transport for MeV electrons is typically related to ULF oscillations (f = 1 mHz to 1 Hz) [e.g., Elkington et al., 2003] or inductive electric fields from interplanetary shocks [e.g., Li et al., 1993]. Lower-energy electrons (100s keV) have drift periods on the order of an hour, so it is conceivable that slower changes in large-scale electric fields could play an important role in their dynamics.

The particle tracer applies a 2-D guiding center approximation under a uniform dawn-dusk electric field to model the drift paths of equatorially mirroring electrons assuming a static dipole magnetic field. The guiding-center velocity is given by

$$\boldsymbol{v}_{\boldsymbol{GC}} = \mu \frac{\boldsymbol{B} \times \boldsymbol{\nabla B}}{B^2} + \frac{\boldsymbol{E} \times \boldsymbol{B}}{B^2}$$

(Eq. 6.2)

where μ is the first adiabatic invariant. The first term is the gradient-B drift, which causes the particle to drift azimuthally about the Earth along trajectories of constant magnetic field strength, and the second term is the **ExB** drift, which allows particles to be transported to regions of stronger or weaker magnetic field. We have neglected the additional drift term related to the curvature of the magnetic field line because we are only modeling equatorially-mirroring particles.

Drift paths for two electrons with μ = 20 MeV/G under the influence of a uniform dawn-to-dusk 2 mV/m electric field for 30 minutes are shown in Figure 6.9. The electrons are initialized at L = 3 for 06 MLT and 18 MLT. In the absence of an electric field, both electrons would drift counterclockwise along the dashed line at L = 3. The dawn-to-dusk electric field introduces a sunward drift that causes the electron on the night side to move radially inward, while the electron on the day side moves radially outward. Although the electric field is uniform, the dayside electron experiences ~0.5 L outward transport, and the nightside electron moves inward by only ~0.3 L. This asymmetry is due to the $1/L^3$ dependence of the magnetic field, which causes the **ExB** drift to be faster at larger L shells for a given electric field. For a purely azimuthal electric field, the **ExB** drift velocity reduces to

$$v_{E\times B} = \frac{E}{B}$$

(Eq. 6.3)

Due to conservation of the first adiabatic invariant, the inward transport on the night side causes an increase in energy from ~190-250 keV, while the outward transport on the day side results in a loss of energy from ~190-130 keV. Under the influence of a large-scale electric field, some of the particles on a given drift shell will gain energy, and others will lose energy. However, only a fraction of the particles need to move inward and be energized to create a large increase in flux given the steep radial PSD gradients in the inner magnetosphere.

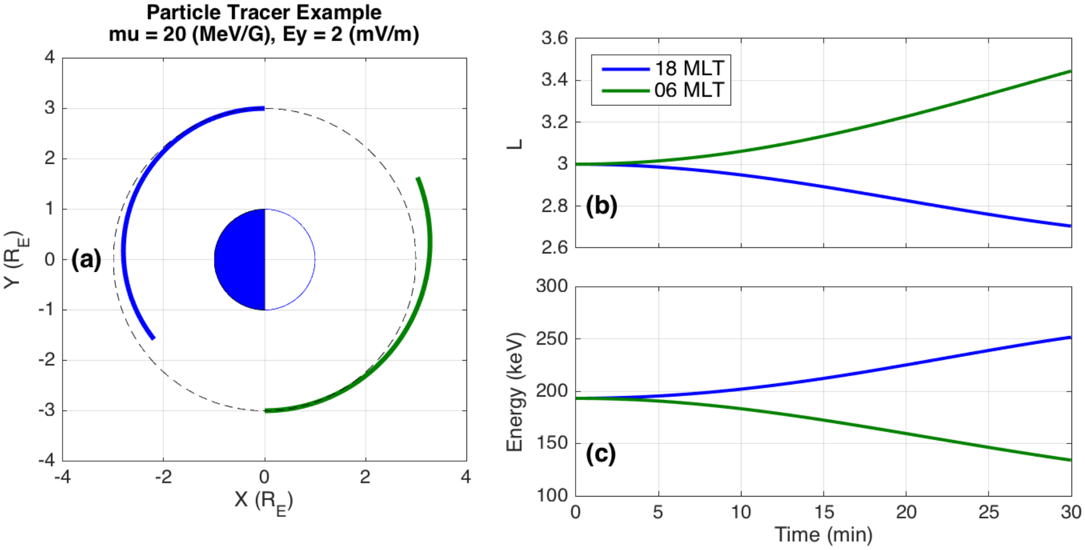

Figure 6.9: Trajectories for equatorially-mirroring electrons with μ = 20 MeV/G under the influence of a 2 mV/m uniform dawn-to-dusk electric field for 30 minutes. (a) Electron positions in the equatorial plane and time evolution of (b) L shell and (c) energy.

In order to model the evolution of PSD profiles, we simulate 5808 electrons evenly spaced by 0.05 L and 0.5 MLT between L = 2 to 8. Each simulation models electrons of constant μ, and the PSD profiles are obtained by binning simulated particles by L shell and applying a weight based on the initial PSD profile. The weighting function is given by

$$W = f_0 \frac{L_0 * dL_0 * dMLT_0}{L_f * dL_{bin} * dMLT_{bin}}$$

(Eq. 6.4)

where f_0 is the initial PSD applied to the particle, L_0 is the initial L shell, L_f is the final L shell, dL_0 and $dMLT_0$ are the initial L and MLT spacing of simulated particles, and dL_{bin} and $dMLT_{bin}$ are the widths of the L and MLT bins. The ratio of the initial to final L shell accounts for fact that simulated particles at larger radial distances represent proportionally more real particles given that the simulated particles are distributed on a uniform (L, MLT) grid.

The initial distributions are assumed to be symmetric in local time, and the final PSD profiles are averaged across all local times. We used PSD data from the two passes shown in Figure 6.5 to simulate the evolution of PSD under the influence of a uniform 2 mV/m dawn-to-dusk electric field. Figure 6.10 (left column) compares the measured PSD profiles to the simulated profiles after the electric field has been applied for 13.5 minutes. The μ values range from 20-100 MeV/G, which translates to 190-690 keV at L = 3. This simple convection model matches the inward transport for 40-100 MeV/G electrons, but it under-predicts the change in location of the steep radial gradient for 20 MeV/G electrons.

An important consideration for interpreting these results is the drift period of the electrons relative to the duration of the applied electric field. A given particle will experience no net radial transport under the influence of a large-scale electric field for exactly the drift period – the particle may move radially inward or outward during the drift orbit, but it will return to the initial position after one complete orbit if the electric field is constant. At a given L shell, higher-energy electrons drift faster due to the μ-dependence of the gradient B drift.

$$\boldsymbol{v}_{\nabla\boldsymbol{B}} = \mu\frac{\boldsymbol{B}\times\nabla\boldsymbol{B}}{B^2}$$

(Eq. 6.5)

Figure 6.11 shows drift periods for different μ values as a function of L shell. Near L = 3, 40 MeV/G electrons have a drift period of roughly 1 hour, and 100 MeV/G electrons drift in about 30 minutes. The drift periods begin to increase sharply for μ < 40 MeV/G.

A possible explanation for the discrepancy for lower μ values is that a low-amplitude electric field persisted for a long duration in addition to a shorter 2 mV/m enhancement. Due to the energy-dependent drift periods, the lower-energy electrons would be influenced by the long-duration electric field, and the faster-drifting, more energetic electrons would not be affected. Figure 6.10 (right column) shows the simulation results for a 0.5 mV/m electric field applied for 54 minutes followed by a 2 mV/m electric field for 13 minutes. The steady, low-amplitude convection electric field created net inward transport for 20 MeV/G electrons, but the shorter drift period for 40-100 MeV/G electrons led to little net transport until the 2 mV/m electric field was applied. The combination of these two effects is able to match the observed transport for μ = 20-100 MeV/G.

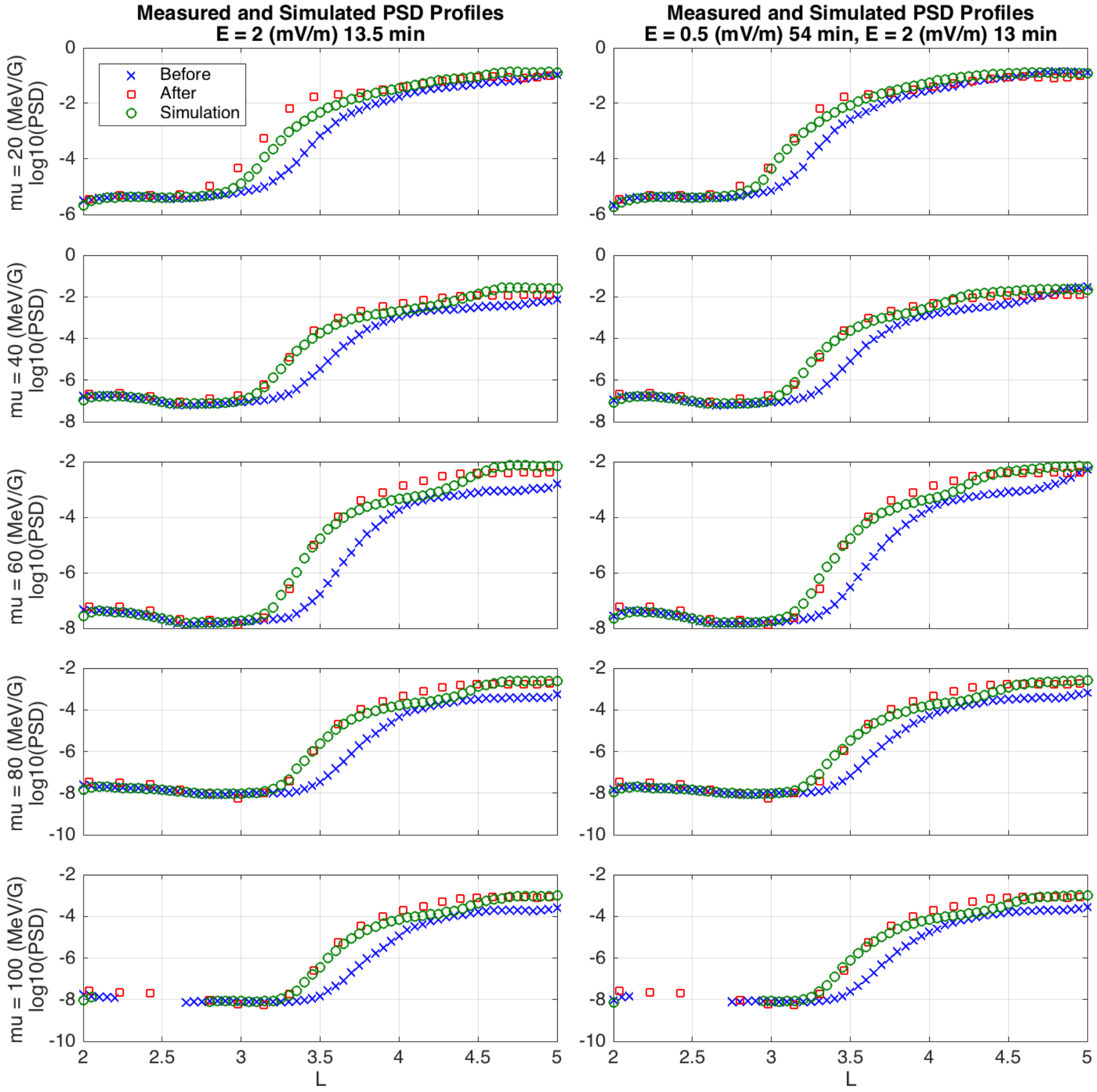

Figure 6.10: Observed PSD profiles and a simulation for a uniform 2 mV/m dawn-to-dusk electric field applied for 13.5 minutes (left column), and a 0.5 mV/m electric field applied for 54 minutes followed by a 2 mV/m electric field applied for 13 minutes (right column).

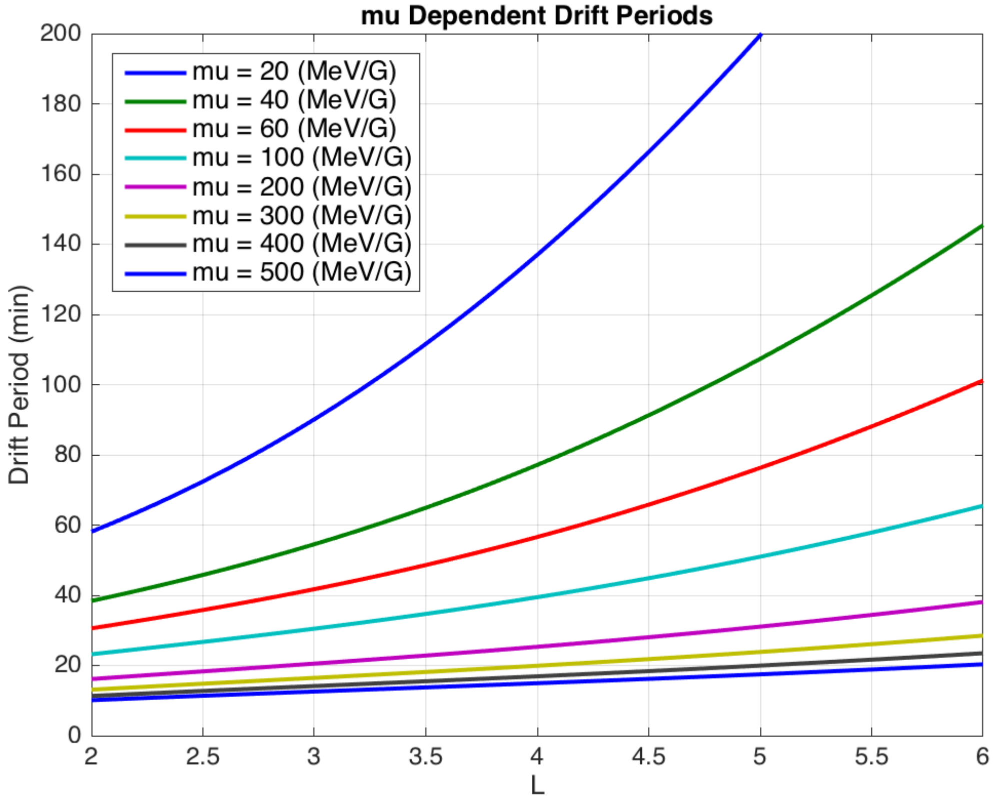

Figure 6.11: Drift periods as a function of L shell for constant μ electrons.

After achieving a solution that matched electrons with μ = 20-100 MeV/G, we extended the simulation to higher μ values to test where this simple model breaks down. Using MagEIS data only, we were able to produce PSD profiles up to 400 MeV/G that covered a large enough L range to observe the differential movement of the sharp PSD gradient between passes. μ = 400 MeV/G corresponds to 1.3 MeV at L = 3.5. The results for 100-400 MeV/G electrons are shown in Figure 6.12 under the influence of a 2 mV/m dawn-to-dusk electric field applied for 13 minutes. The previous results in Figure 6.10 show that the long-duration 0.5 mV/m electric field had little effect on electrons above μ = 40 MeV/G, so we only focus on the impact of the larger-amplitude electric field.

The results from the simple convection model begin to diverge from the observations at μ = 200 MeV/G, and the μ = 400 MeV/G electrons are barely affected by this electric field. This can be understood by the drift periods in Figure 6.11: electrons with μ greater than 200 MeV/G at L = 3 drift around the Earth in less than 25 minutes, and the electric field was applied for 13 minutes, which is a significant fraction of the drift period. Large-scale electric fields applied for an entire drift period have zero net effect on radial transport for a given particle. These results suggest that shorter-duration electric field enhancements would be required to match the observed behavior of higher-energy electrons. Close inspection of the electric field data show variations of 0.5-1 mV/m on timescales of 2-3 minutes, which may explain the observed transport for higher-energy electrons. Alternatively, the disagreement for higher-energies may indicate a transition point where ULF waves or local acceleration become important.

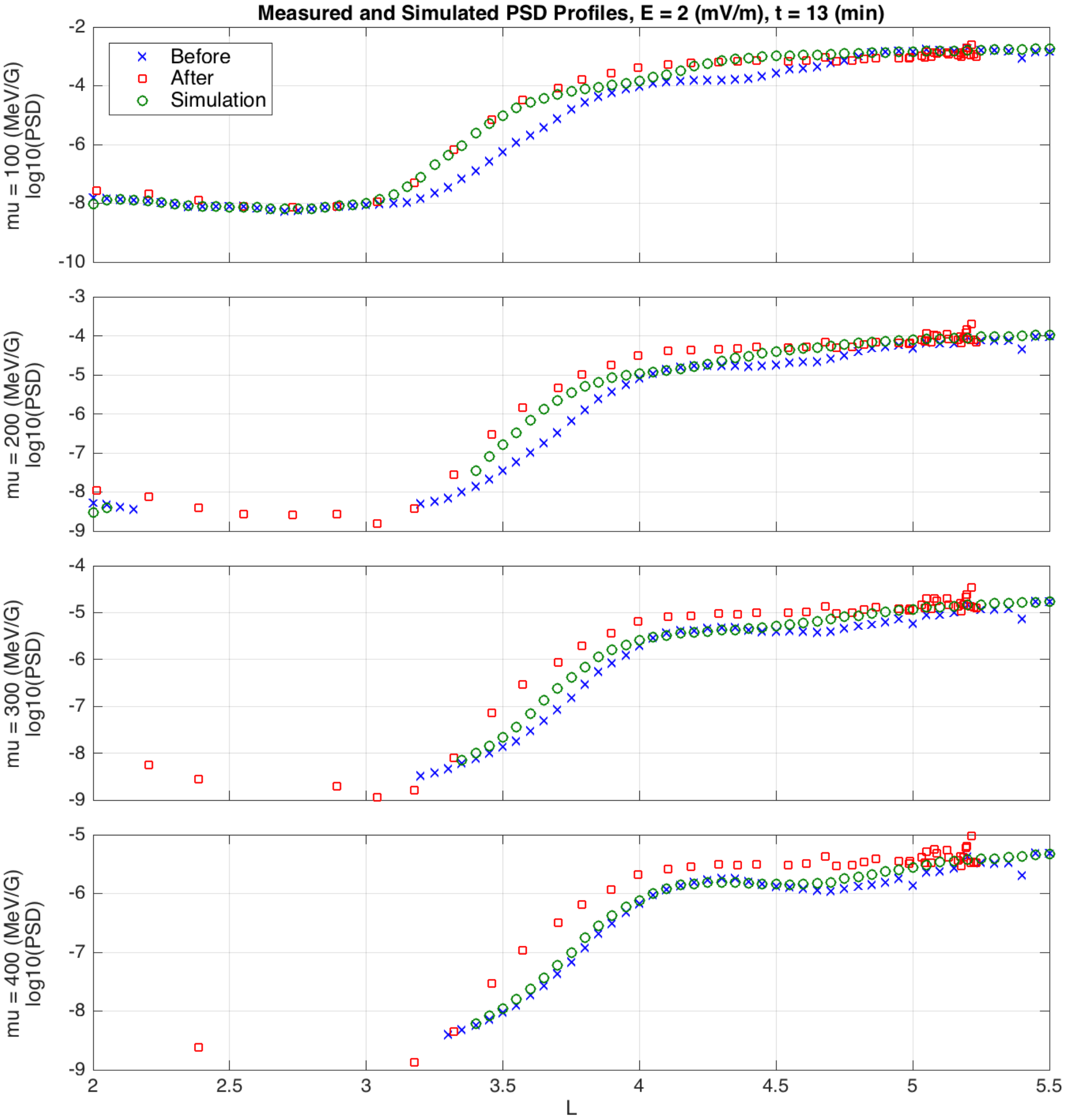

Figure 6.12: Observed PSD profiles and simulation results with a uniform 0.5 mV/m dawn-to-dusk electric field applied for 54 minutes, followed by a 2 mV/m dawn-to-dusk electric field applied for 13 minutes.

6.6 Discussion

The results in the previous section show that the evolution of electrons over a wide range of energies (~130-500 keV) at low L shells in the slot region can be explained by radial transport through a simple, uniform, large-scale convection electric field model. In situ electric field measurements by the Van Allen Probes and THEMIS E support the picture that the convection electric field penetrated to low L shells during this event. Electric fields were measured by all three spacecraft on the order of 1-2 mV/m below L = 3. Also, the plasmapause is known to be driven by large-scale electric fields, and gradients in spacecraft potential as well as boundaries for plasmaspheric hiss and chorus suggest that the plasmapause moved inward to below L = 2 during this period. The simulation demonstrates that the same large-scale electric fields responsible for altering the shape of the plasmasphere are also capable of transporting 100s keV electrons radially inward, creating the observed electron flux enhancements.

The duration of the applied electric field creates a differential effect on electrons of different energies due to the energy-dependent drift periods of the electrons. This concept is analogous to drift-resonance with ULF waves, which is used to explain radial diffusion for MeV electrons. However, the physical interpretation is fundamentally different: ULF waves are interpreted as resonant oscillations at particular frequencies determined by the magnetic field and plasma populations, but convection is a large-scale sunward flow driven by the solar wind; ULF oscillations are zero mean, but the convection electric field has a net DC component pointing from dawn to dusk. The simulated 2 mV/m electric field enhancement for 13 minutes could be viewed as a ULF wave with a frequency of 1.2 mHz, but physically it represents short-duration increase of sunward flow in the inner magnetosphere.

This model is also differentiated from radial diffusion by ULF waves because the transport occurs in a relatively large step over a short period of time. Although the complete filling of the slot region typically occurs over many hours, it is unclear based on the sparse spatial and temporal sampling from only two spacecraft whether the flux enhancements are a result of a series of impulsive steps or are due to a slow diffusive process. Our simple model using electric fields similar to the observations shows that the enhancements could be described by non-diffusive transport related to increases in the convection electric field.

The uniform convection model that matched the observed transport for 20-100 MeV/G electrons did not reproduce the behavior of the higher-energy electrons. There are several interpretations of this result. The actual large-scale electric field may vary on timescales faster than the simulated 13 minutes, which would allow the faster-drifting electrons to be affected. This may be more realistic given the 2-3 minute electric field variations present in the data.

Also, the steep PSD gradient is located at higher L shells for higher energies, so there may be fluctuations that are better described as ULF waves, rather than convection, which interact with the higher-energy electrons through conventional radial diffusion at these radial distances. The electric field measurements often exhibit more steady characteristics at lower L shells and increased variation at higher L shells (Figures 6.6-6.8).

Alternatively, the more energetic electron dynamics (> 100 MeV/G) may be driven primarily by local acceleration rather than radial transport. Chorus waves were observed in the same region as the flux enhancements, and they could have accelerated 100s keV electrons to MeV energies. In this scenario, the plasmapause erosion to low L shells and inward transport for 10s to 100s keV electrons is caused by large-scale electric fields. Inward transport preferentially accelerates electrons in the perpendicular direction, generating the anisotropy required in the lower-energy electron population (< 10 keV) to produce chorus waves, and the chorus waves simultaneously energize some of the electrons to MeV energies. Under this interpretation, the radial transport and local acceleration mechanisms are coupled and interact with electrons over a wide range of energies (keV to MeV) in the same spatial region.

While we cannot definitively distinguish between radial transport and local acceleration given the sparse spatial and temporal observations, the success of a simple convection model in matching the dynamics of 20-100 MeV/G (~190-700 keV at L = 3, ~130-500 keV at L = 3.5) electrons suggests that radial transport is the dominant energization mechanism for these energies. Also, the relative radial displacement of the steep PSD gradient was consistently ~0.3 L for electrons up to at least 400 MeV/G (Figure 6.12), and there were no peaks in PSD that would suggest local acceleration, even for the higher energies. Therefore, the PSD profiles alone do not clearly point to a transition between radial transport and local acceleration in this energy range.

6.7 Summary and Conclusions

This study focused on the relationship between large-scale electric fields and 100s keV electron enhancements in the slot region. The Van Allen Probes frequently observe slot region enhancements, and previous studies have shown that strong electric fields exist at low L shells during active times. We identified two consecutive dawnside passes by the Van Allen Probes separated by 1.5 hours that show more than 2 orders of magnitude increase in 100s keV electron flux near L = 3. Converting flux to PSD revealed a sharp radial PSD gradient that moved radially inward between the two observations, suggesting radial transport as a mechanism. In situ electric field observations by the Van Allen Probes and THEMIS E provided direct evidence of 1-2 mV/m electric fields below L = 3 during the same time period. The presence of low-L electric fields was also supported by spacecraft potential, plasmaspheric hiss and chorus observations, which indicated that the plasmapause eroded below L = 2.

A 2-D guiding center particle tracer was developed to model the evolution of PSD under the influence of a uniform dawn-to-dusk electric field. We demonstrated that a 2 mV/m uniform convection electric field applied for 13.5 minutes could reproduce the observed changes in PSD profiles for 40-100 MeV/G electrons. However, the simulation did not produce enough inward transport to match the observations for 20 MeV/G electrons. We were able to resolve this discrepancy by applying a 0.5 mV/m electric field for 54 minutes prior to the 2 mV/m enhancement. The long-duration electric field was more effective in transporting the more-slowly drifting low-energy electrons while having little effect on the higher energies, matching the observations for 20-100 MeV/G electrons.

We then applied the 2 mV/m uniform electric field to higher-energy electrons, and found that same model could not explain the behavior for μ = 200-400 MeV/G (~0.8-1.3 MeV at L = 3.5), which have drift periods of less than 25 minutes. This suggests that the actual electric field may have varied faster than the 13-minute enhancement in the model, and the in situ electric field measurements do show variations on the order of 2-3 minutes. However, the presence of chorus waves in the same spatial region as the enhancements leaves the possibility open that local acceleration was responsible for the higher-energy dynamics.

Our results show that large-scale convection at low L shells with similar magnitude to the in situ measurements is sufficient to explain slot region enhancements for 130-500 keV electrons, and it is possible that variations in convection are important for even higher-energy electrons.

Chapter 7: Summary, Conclusions and Future Work

7.1 Summary and Conclusions

This dissertation addressed electric fields and their impact on various plasma populations in the inner magnetosphere. The inner magnetosphere is a dynamic environment where coupling across a wide range of particle energies and spatial locations creates a complex response to solar activity. Unraveling the dynamics through spacecraft observations is challenging because of the limited spatial and temporal coverage provided by only a few spacecraft over such a large spatial region. A combination of long-term statistics, event specific studies and theoretical models are required to create a coherent picture, even when studying a limited aspect of the system. We contributed to this effort on multiple fronts: we investigated the behavior of double-probe instruments, studied the average characteristics of the electric field and the physical mechanisms responsible for enhanced electric fields on the dusk side, and we related in situ electric field measurements to 100s keV electron enhancements deep within the inner magnetosphere.

In Chapter 3 we discussed electric field measurements onboard spacecraft using double-probe instruments. We identified the shorting factor as a significant source of error in the inner magnetosphere when coupled with large **vxB** subtraction due to spacecraft motion in the Earth's magnetic field. The instrument is affected by variable plasma environments in the inner magnetosphere, causing the shorting factor to change by up to ~30% throughout the orbit. However, current modeling techniques of varying fidelity do not predict the observed shorting factor, especially in low-density plasmas. This discrepancy serves to motivate future work on understanding the behavior of double-probe instruments.

We presented the average structure of the large-scale electric field in the inner magnetosphere in Chapter 4. This study offers the most complete picture of the electric field based on in situ equatorial measurements to date by using multiple years of THEMIS data covering all local times and L shells in the inner magnetosphere. The data reveal strong electric fields at low L shells during storms, and a dawn-dusk asymmetry with stronger electric fields in the dusk sector. This study has already motivated others in the field to improve existing electric field models, which do not provide realistic electric fields at low L shells.

In Chapter 5 we studied particle and fields observations from the Van Allen Probes related to strong duskside electric fields at low L shells. This study was directly motivated by the statistical results from THEMIS in Chapter 4. We showed that the electric fields are associated with SAPS, which is caused by a separation between plasma sheet ions and electrons that leads to field-aligned currents closing through the ionosphere in a region of low conductivity. Data from DMSP revealed similar particle and current structures at low altitudes along the magnetic field lines that map to the equatorial magnetosphere, and the combined Van Allen Probes and DMSP observations suggest significant spatial and temporally variability within the SAPS region.

Finally, we connected in situ electric field measurements at low L shells to 100s keV electron enhancements in the slot region. There is ongoing debate over the relative importance of radial transport and local acceleration in energizing radiation belt electrons. This study showed that we can explain electron enhancements in the slot region for energies up to at least 500 keV through radial transport based on a simple convection model using electric fields with similar magnitude to the observations.

7.2 Future Work

There are many possibilities for extending the work presented in this dissertation.

7.2.1 Improving Electric Field Measurements

Double-probe instruments have improved dramatically over the past 40 years, with uncertainties of many mV/m being reduced to ~0.1 mV/m on the current Magnetospheric MultiScale (MMS) mission. However, the work in the Chapter 3 showing that current models severely under-predict the shorting factor for THEMIS demonstrates that we have room for progress in understanding the instrument. The highly accurate measurements on MMS require redundant electric field observations from the electron drift instrument to provide a hard reference for DC offsets. Ideally, we could predict the instrument response on the ground. This would be especially important for deploying constellations of low-cost satellites, where adding redundant instruments would not be feasible.

The work in Chapter 3 could be extended to other missions such as Cluster, the Van Allen Probes and MMS to determine how the shorting factor is affected by varying plasma conditions for different instrument configurations. Other methods for determining the shorting factor could be used, including comparing the double-probe data to the **vxB** from ion measurements or an electron drift instrument if available. We could also investigate the sunward offset, which limits the usefulness of the Ex measurement for THEMIS. These studies could be coordinated with modelers to uncover the missing physics and improve the current models.

7.2.2 Electric Field Spatial and Temporal Scales and Timing

The THEMIS study in Chapter 4 showed that there is a structure to the electric field in the inner magnetosphere during active times. However, sampling that structure required years of observations, and the temporal evolution during individual storms remains an open question. Individual events show features that resemble the average electric field values, such as the SAPS in Chapter 5 and the low-L electric field and dawn-dusk asymmetry in Chapter 6, but the variability in the observations is significant. The variable electric and magnetic fields in Chapter 5 could be interpreted as earthward propagating structures that are ~1 R_E wide, but this cannot be resolved with only one spacecraft.

Future work could include using THEMIS, the Van Allen Probes and MMS to study the scale sizes and propagation of electric field and current structures in the inner magnetosphere. The current understanding is that dipolarization fronts propagating Earthward from the tail slow down near geosynchronous orbit, but the data in Chapter 5 suggest that some remnant of these structures may reach L = 3.5 or below. Ground-based measurements and high-inclination spacecraft could be included in this effort to track disturbances as they propagate in radially and azimuthally.

7.2.3 Multipoint Measurements and Data Assimilation

In my opinion, there are two main factors that are limiting our progress in understanding the inner magnetosphere: sparse observations and inefficient processes for combining data from various sources. The basic physics are well understood, but the observations are either unavailable or too cumbersome to combine to answer many of the open questions unambiguously. In the case of radiation belt dynamics, the debate over the relative roles of radial transport and local acceleration has been active for over a decade. This dissertation contributed to the discussion by showing that a simple enhancement in convection can explain slot region enhancements for electrons up to 500 keV by radial transport. However, the observations simultaneously provide evidence for radial transport through large-scale electric fields and local acceleration through chorus waves.

In order to resolve the differences between these mechanisms, much more extensive measurements are required. First, the large-scale magnetic field configuration must be known in order to accurately assess adiabatic changes in the electron populations. Currently, empirical magnetic field models are used to compute phase space density, and there are discrepancies between the models and the in situ data that are usually acknowledged but not directly accounted for in the analysis. In the future, multipoint magnetic field measurements could be assimilated to provide event-specific estimates of the actual magnetic field configuration. Similarly, multipoint electric field and/or cold plasma measurements could be used to estimate the large-scale electric fields. Without realistic estimates of the large-scale magnetic and electric field configurations, we cannot isolate changes in radiation belt electron population that are due to transport conserving the first two adiabatic invariants. Distributed high-frequency fields measurements would also be useful to estimate the global distribution of waves that are thought to be important in local acceleration processes.

Infinite measurements would not be required to advance our understanding of radiation belt acceleration processes. Higher-energy particles drift around the Earth faster than lower-energy particles, so fewer local time observations would be needed for these particles in order to resolve changes along the drift orbit. For 100s keV electrons, which drift around the Earth in ~1 hour at L = 3, 6 spacecraft could provide 10 minute resolution on changes in the particle population as a function of local time. Local time asymmetries in the particle distributions are currently very difficult to measure, but they could offer important clues to the mechanisms that drive the dynamics. In order to design such a constellation, the question would have to be refined to specify the relative importance of radial transport and local acceleration over a given spatial and temporal scale. There will always be dynamics that cannot be resolved due to limited observations, but we could target specific spatial and temporal scales through clever orbit design.

If we were able to obtain a global set of observations that are mathematically sufficient to answer the relevant science questions, a large effort would be required to combine the data into a global assimilative model. Cross-calibration issues would be a major challenge – particle detectors onboard the same spacecraft with overlapping energy ranges can disagree by a factor of 3 or more. Also, many years of experience are needed to understand data issues for each type of instrument, so experts for each observational platform would need to be committed to providing "clean" data and quantifying realistic uncertainties. Other industries are advancing "big data" techniques that could be leveraged in our field to extract as much information as possible from a large set of observations.

Bibliography

Anderson, P. C., D. L. Carpenter, K. Tsuruda, T. Mukai, and F. J. Rich (2001), Multisatellite observations of rapid subauroral ion drifts (SAID), J. Geophys. Res., 106, 29,585–29,600, doi:10.1029/2001JA000128.

Angelopoulos, V., et al. (2008), First results from the THEMIS Mission, Space Sci. Rev., 141, 453–476.

Auster, H. U., et al. (2008), The THEMIS fluxgate magnetometer, Space Sci. Rev., 141, 235–264.

Bale, S. D., et al. (2008), The Electric Antennas for the STEREO/WAVES Experiment, Space Sci. Rev., 136, 529–547.

Banks, P. M., and F. Yasuhara (1978), Electric fields and conductivity in the nighttime E-region: A new magnetosphere-ionosphere-atmosphere coupling effect, Geophys. Res. Lett., 5, 1047–1050, doi:10.1029/GL005i012p01047.

Baumjohann, W., G. Paschmann, and C. A. Cattell (1989), Average plasma properties in the central plasma sheet, J. Geophys. Res., 94(A6), 6597–6606, doi:10.1029/JA094iA06p06597.

Blake, J. B., et al. (2013), The Magnetic Electron Ion Spectrometer (MagEIS) instruments aboard the Radiation Belt Storm Probes (RBSP) spacecraft, Space Sci. Rev., 179, 383–421, doi:10.1007/s11214-013-9991-8.

Blum, L. W., et al. (2015), Observations of coincident EMIC wave activity and duskside energetic electron precipitation on 18–19 January 2013, Geophys. Res. Lett., 42, 5727–5735, doi:10.1002/2015GL065245.

Bonnell, J. W., F. S. Mozer, G. T. Deloy, A. J. Hull, R. E. Ergun, C. M. Cully, V. Angelopoulos, and P. R. Harvey (2008), The Electric Field Instrument (EFI) for THEMIS, Space Sci. Rev., 141, 303–341.

Bortnik, J., R.M. Thorne, N.P. Meredith (2008), The unexpected origin of plasmaspheric hiss from discrete chorus emissions, Nature, 452 (7183) (2008), pp. 62–66, doi:10.1038/nature06741.

Burch, J. L., J. Goldstein, and B. R. Sandel (2004), Cause of plasmasphere co-rotation lag, Geophys. Res. Lett., 31, L05802, doi:10.1029/2003GL019164.

Burke, W. J., N. C. Maynard, M. P. Hagan, R. A. Wolf, G. R. Wilson, L. C. Gentile, M. S. Gussenhoven, C. Y. Huang, T. W. Garner, and F. J. Rich (1998), Electrodynamics of the inner magnetosphere observed in the dusk sector by CRRES and DMSP during the magnetic storm of June 4–6, 1991, J. Geophys. Res., 103(A12), 29,399–29,418, doi:10.1029/9 8JA02197.

Burke, W. J., A.G. Rubin, N. C. Maynard, L. C. Gentile, P. J. Sultan, F. J. Rich, O. de La Beaujardière, C. Y. Huang, G. R. Wilson (2000), Ionospheric disturbances observed by DMSP at middle to low latitudes during the magnetic storm of June 4–6, 1991. J. Geophys. Res. 105, 18391–18405.

Califf, S., and C. M. Cully (2016), Empirical estimates and theoretical predictions of the shorting factor for the THEMIS double-probe electric field instrument, J. Geophys. Res. Space Physics, 121, doi:10.1002/2016JA022589.

Califf, S., et al. (2013), DC electric field observations from THEMIS and the Van Allen Probes, AGU Poster SM51B-2180.

Califf, S., et al. (2014), THEMIS measurements of quasi-static electric fields in the inner magnetosphere, J. Geophys. Res. Space Physics, 119, 9939–9951, doi:10.1002/2014JA020360.

Califf, S., X. Li, R. A. Wolf, H. Zhao, A. N. Jaynes, F. D. Wilder, D. M. Malaspina, and R. Redmon (2016a), Large-amplitude electric fields in the inner magnetosphere: Van Allen Probes observations of subauroral polarization streams, J. Geophys. Res. Space Physics, 121, 5294–5306, doi:10.1002/2015JA022252.

Califf, S., X. Li, H. Zhao, A. Kellerman, T. E. Sarris, A. Jaynes, and D. M. Malaspina (2016b), The role of the convection electric field in filling the slot region between the inner and outer radiation belts, J. Geophys. Res. (submitted)

CCMC website, http://ccmc.gsfc.nasa.gov/educational/ MagnetosphereWebPage_clip_image002_0000.jpg

Chen, A. J. (1970), Penetration of low-energy electrons deep into the magnetosphere, J. Geophy s. Res., 75(13), 2458–2467, doi:10.1029/JA075i013p02458.

Cully, C. M., R. E. Ergun, and A. I. Eriksson (2007), Electrostatic structure around spacecraft in tenuous plasmas, J. Geophys. Res., 112, A09211, doi:10.1029/2007JA012269.

Daglis, I. A., R. M. Thorne, W. Baumjohann, and S. Orsini (1999), The terrestrial ring current: Origin, formation, and decay, Rev. Geophys., 37, 407–438, doi:10.1029/1999RG900009.

Dai, L., et al. (2013), Excitation of poloidal standing Alfven waves through drift resonance wave-particle interaction, Geophys. Res. Lett., 40, 4127–4132, doi:10.1002/grl.50800.

Darrouzet, F. et al. (2009), Plasmaspheric density structures and dynamics: properties observed by Cluster and IMAGE missions, Space Sci. Rev., 145, 55-106, doi:10.1007/s11214-008-9438-9.

Dungey, J. W. (1961), Interplanetary magnetic field and auroral zones, Phys. Rev. Letters, 6, 47.

Elkington, S. R., M. K. Hudson, and A. A. Chan (2003), Resonant acceleration and diffusion of outer zone electrons in an asymmetric geomagnetic field, J. Geophys. Res., 108(A3), 1116, doi:10.1029/2001JA009202.

Engwall, E., A. I. Eriksson, and J. Forest (2006), Wake formation behind positively charged spacecraft in flowing tenuous plasmas, Phys. Plasmas, 13, 062904, doi:10.1063/1. 2199207.

Eriksson, A. I., et al. (2006), Electric field measurements on Cluster: Comparing the double-probe and electron drift techniques, Ann. Geophys., 24, 275–289.

Fok, M.-C., et al. (2003), Global ENA IMAGE simulations, Space Sci. Rev., 109, 77–103.

Foster, J. C., and W. J. Burke (2002), SAPS: A new categorization for subauroral electric fields, Eos Trans. AGU, 83, 393–394, doi:10.1029/2002EO000289.

Foster, J. C., and H. B. Vo (2002), Average characteristics and activity dependence of the subauroral polarization stream, J. Geophys. Res., 107(A12), 1475, doi:10.1029/2002JA009409.

Foster, J. C., P. J. Erickson, A. J. Coster, S. Thaller, J. Tao, J. R. Wygant, and J. Bonnell (2014), Storm time observations of plasmasphere erosion flux in the magnetosphere and ionosphere, Geophys. Res. Lett., 41, 762–768, doi:10.1002/2013GL059124.

Funsten, H., et al. (2013), Helium, Oxygen, Proton, and Electron (HOPE) mass spectrometer for the radiation belt storm probes mission, Space Sci. Rev., 179, 1–62, doi:10.1007/s11214-013-9968-7.

Galperin, Y. I., V. N. Ponomarev, and A. G. Zosimova (1974), Plasma convection in polar ionosphere, Ann. Geophys., 30, 1–7.

Gamayunov, K. V., G. V. Khazanov, M. W. Liemohn, M.-C. Fock, and A. J. Ridley (2009), Self-consistent model of magnetospheric electric field, ring current, and electromagnetic ion cyclotron waves: Initial results, J. Geophys. Res., 114, A03221, doi:10.1029/2008JA013597.

Garner, T. W., R. A. Wolf, R. W. Spiro, W. J. Burke, B. G. Fejer, S. Sazykin, J. L. Roeder, and M. R. Hairston (2004), Magnetospheric electric fields and plasma sheet injection to low L-shells during the 4–5 June 1991 magnetic storm: Comparison between the Rice Convection Model and observations, J. Geophys. Res., 109, A02214, doi:10.1029/2003JA010208.

Gkioulidou, M., A. Y. Ukhorskiy, D. G. Mitchell, T. Sotirelis, B. H. Mauk, and L. J. Lanzerotti (2014), The role of small-scale ion injections in the buildup of Earth's ring current pressure: Van Allen Probes observations of the 17 March 2013 storm, J. Geophys. Res. Space Physics, 119, 7327–7342, doi:10.1002/2014JA020096.

Goldstein, J., B. R. Sandel, M. R. Hairston, and P. H. Reiff (2003), Control of plasmaspheric dynamics by both convection and sub-auroral polarization stream, Geophys. Res. Lett., 30(24), 2243, doi:10.1029/2003GL018390.

Green, J. C., and M. G. Kivelson (2004), Relativistic electrons in the outer radiation belt: Differentiating between acceleration mechanisms, J. Geophys. Res., 109, A03213, doi:10.1029/2003JA010153.

Greenspan, M. E., C. E. Rasmussen, W. J. Burke, and M. A. Abdu (1991), Equatorial density depletions observed at 840 km during the Great Magnetic Storm of March 1989, J. Geophys. Res., 96(A8), 13931-13942.

Harel, M., R. A. Wolf, R. W. Spiro, P. H. Reiff, C.-K. Chen, W. J. Burke, F. J. Rich, and M. Smiddy (1981), Quantitative simulation of a magnetospheric substorm 2. Comparison with observations, J. Geophys. Res., 86, 2242–2260, doi:10.1029/JA086iA04p02242.

Horne, R. B., et al. (2005), Wave acceleration of electrons in the Van Allen radiation belts, Nature, 437, 227–230.

Huang, C. S., J. C. Foster, and J. M. Holt (2001), Westward plasma drift in the midlatitude ionospheric F region in the midnight-dawn sector, J. Geophys. Res., 106(A12), 30,349–30,362, doi:10.1029/2001JA001110.

Hudson, M. K., et al. (2001), Radiation belt electron acceleration by ULF wave drift resonance: Simulation of 1997 and 1998 storms, in Space Weather, AGU Monogr., vol. 125, edited by P. Song, H. Singer, and G. Siscoe, 289 pp., AGU, Washington, D. C.

Jaynes, A. N., et al. (2015), Source and seed populations for relativistic electrons: Their roles in radiation belt changes, J. Geophys. Res. Space Physics, 120, doi:10.1002/2015JA021234.

Kataoka, R., D. Shiota, E. Kilpua, and K. Keika (2015), Pileup accident hypothesis of magnetic storm on 17 March 2015, Geophys. Res. Lett., 42, doi:10.1002/2015GL064816.

Khotyaintsev, Y. V., P.-A. Lindqvist, C. M. Cully, A. I. Eriksson, and M. Andre (2014), In-flight calibration of double-probe electric field measurements on Cluster, Geosci. Instrum. Method. Data Syst., 3, 143–151, doi: 10.5194/gi-3-143-2014.

Kletzing, C. A., et al. (2013), The Electric and Magnetic Field Instrument Suite and Integrated Science (EMFISIS) on RBSP, Space Sci. Rev., 179, 127–181, doi:10.1007/s11214-013-9993-6.

Korth, H., M. F. Thomsen, J. E. Borovsky, and D. J. McComas (1999), Plasma sheet access to geosynchronous orbit, J. Geophys. Res., 104(A11), 25,047–25,061, doi:10.1029/1999JA900292.

Kurth, W. S., S. De Pascuale, J. B. Faden, C. A. Kletzing, G. B. Hospodarsky, S. Thaller, and J. R. Wygant (2015), Electron densities inferred from plasma wave spectra obtained by the waves instrument on Van Allen Probes, J. Geophys. Res. Space Physics, 120, 904–914, doi:10.1002/2014JA020857.

Li, X., I. Roth, M. Temerin, J. R. Wygant, M. K. Hudson, and J. B. Blake (1993), Simulation of the prompt energization and transport of radiation belt particles during the March 24, 1991 SSC, Geophys. Res. Lett., 20(22), 2423–2426, doi:10.1029/93GL02701.

Li, X., R. S. Selesnick, D. N. Baker, A. N. Jaynes, S. G. Kanekal, Q. Schiller, L. Blum, J. Fennell, and J. B. Blake (2015), Upper limit on the inner radiation belt MeV electron intensity, J. Geophys. Res. Space Physics, 120, 1215–1228, doi:10.1002/2014JA020777.

Lyons, L. R., and R. M. Thorne (1973), Equilibrium structure of radiation belt electrons, J. Geophys. Res., 78(13), 2142–2149, doi:10.1029/JA078i013p02142.

Lyons, L. R. and D. J. Williams (1984), Quantitative aspects of magnetospheric physics, D. Reidel, Dordrecht-Holland.

Malaspina, D. M., J. R. Wygant, R. E. Ergun, G. D. Reeves, R. M. Skoug, and B. A. Larsen (2015), Electric field structures and waves at plasma boundaries in the inner magnetosphere, J. Geophys. Res. Space Physics, 120, doi:10.1002/2015JA021137.

Mannucci, A. J., B. T. Tsurutani, M. A. Abdu, W. D. Gonzalez, A. Komjathy, E. Echer, B. A. Iijima, G. Crowley, and D. Anderson (2008), Superposed epoch analysis of the dayside ionospheric response to four intense geomagnetic storms, J. Geophys. Res., 113, A00A02, doi:10.1029/2007JA012732.

Matsui, H., P. A. Puhl-Quinn, V. K. Jordanova, Y. Khotyaintsev, P. A. Lindqvist, and R. B. Torbert (2008), Derivation of inner magnetospheric electric field (UNH-IMEF) model using Cluster data set, Ann. Geophys., 26, 2887–2898.

Mozer, F. S. (1970), Electric field mapping in the ionosphere at the equatorial plane, Planet. Space Sci., 18, 259–263.

Nishimura, Y., et al, (2013), Structures of dayside whistler-mode waves deduced from conjugate diffuse aurora, J. Geophys. Res. Space Physics, 118, 664–673, doi:10.1029/2012JA018242.

Pedersen, A., C. A. Cattell, C.-G. Falthammar, V. Formisano, P.-A. Lindqvist, F. Mozer, and R. Torbert (1984), Quasistatic electric field measurements with spherical double probes on the GEOS and ISEE satellites, Space Science Reviews, 37, 269-312.

Pedersen, A., F. Mozer, and G. Gustafsson (1998), Electric field measurements in a tenuous plasma with spherical double probes, in Measurement Techniques in Space Plasmas Fields, Geophys. Monogr. Ser., vol. 103, edited by R. F. Pfaff, J. E. Borovsky, and D. T. Young, AGU, Washington, D. C., doi:10.1002/9781118664391.ch1.

Puhl-Quinn, P. A., H. Matsui, E. Mishin, C. Mouikis, L. Kistler, Y. Khotyaintsev, P. M. E. De´cre´au, and E. Lucek (2007), Cluster and DMSP observations of SAID electric fields, J. Geophys. Res., 112, A05219, doi:10.1029/2006JA012065.

Reeves, G. D., R. W. H. Friedel, M. G. Henderson, A. Korth, P. S. McLachlan, and R. D. Belian (1996), Radial propagation of substorm injections, International Conference on Substorms-3, Eur. Space Agency Spec. Publ., ESA SP-339, 579.

Reeves, G. D., K. L. McAdams, R. H. W. Friedel, and T. P. O'Brien (2003), Acceleration and loss of relativistic electrons during geomagnetic storms, Geophys. Res. Lett., 30(10), 1529, doi:10.1029/2002GL016513.

Reeves, G. D., et al. (2013), Electron acceleration in the heart of the Van Allen radiation belts, Science, 341(6149), 991–994, doi:10.1126/science.1237743.

Reeves, G. D., et al. (2016), Energydependent dynamics of keV to MeV electrons in the inner zone, outer zone, and slot regions, J. Geophys. Res. Space Physics, 121, 397–412, doi:10.1002/2015JA021569.

Roussel, J.-F., F. Rogier, G. Dufour , J.-C. Matéo-Vélez, J.Forest, A. Hilgers , D. Rodgers, L. Girard and D. Payan, (2008) SPIS Open-Source Code: Methods, Capabilities, Achievements, and Prospects, IEEE Trans. Plasma Sci.,36 (5), doi: 10.1109/TPS.2008.2002327.

Rowland, D. E., and J. R. Wygant (1998), Dependence of the large-scale, inner magnetospheric electric field on geomagnetic activity, J. Geophys. Res., 103, 14,959–14,964, doi:10.1029/97A03524.

Runov, A., V. Angelopoulos, X.-Z. Zhou, X.-J. Zhang, S. Li, F. Plaschke, and J. Bonnell (2011), A THEMIS multicase study of dipolarization fronts in the magnetotail plasma sheet, J. Geophys. Res., 116, A05216, doi:10.1029/2010JA016316.

Saikin, A. A., J. C. Zhang, R. C. Allen, C. W. Smith, L. M. Kistler, H. E. Spence, R. B. Torbert, C. A. Kletzing, and V. K. Jordanova (2015), The occurrence and wave properties of H+-, He+-, and O+-band EMIC waves observed by the Van Allen Probes, J. Geophys. Res. Space Physics, 120, 9, doi:10.1002/2015JA021358.

Sandel, B. R., J. Goldstein, D. L. Gallagher, and M. Spasojevic (2003), Extreme ultraviolet imager observations of the structure and dynamics of the plasmasphere, Space Sci. Rev., 109, 25–46, doi:10.1023/B:SPAC.0000007511.47727.5b.

Sarrailh P., J.C. Matéo-Vélez, S. Hess, J.F. Roussel, B. Thiébault, J. Forest, B. Jeanty-Ruard, A. Hilgers, D. Rodgers and F. Cipriani (2014) SPIS 5: new modelling capabilities and method for scientific mission. Spacecraft Charging Technology Conference 2014.

Sarris, T. E., X. Li, N. Tsaggas, and N. Paschalidis (2002), Modeling energetic particle injections in dynamic pulse fields with varying propagation speeds, J. Geophys. Res., 107(A3), 1033, doi:10.1029/2001JA900166.

Sazykin, S., R. W. Spiro, R. A. Wolf, F. R. Toffoletto, N. Tsyganenko, J. Goldstein, and M. R. Hairston (2005), Modeling inner magnetospheric electric fields: Latest self-consistent results, in The Inner Magnetosphere: Physics and Modeling, edited by T. I. Pulkkinen, N. A. Tsyganenko, and R. H. W. Friedel, pp. 263–270, AGU, Washington, D.C.

Schiller, Q., X. Li, L. Blum, W. Tu, D. L. Turner, and J. B. Blake (2014), A nonstorm time enhancement of relativistic electrons in the outer radiation belt, Geophys. Res. Lett., 41, 7–12, doi:10.1002/2013GL058485.

Schunk, R. W., P. M. Banks, and W. J. Raitt (1976), Effects of electric fields and other processes upon the nighttime high-latitude F layer, J. Geophys. Res., 81, 3271–3282, doi:10.1029/JA081i019p03271.

Selesnick, R. S., D. N. Baker, A. N. Jaynes, X. Li, S. G. Kanekal, M. K. Hudson, and B. T. Kress (2014), Observations of the inner radiation belt: CRAND and trapped solar protons, J. Geophys. Res. Space Physics, 119, 6541–6552, doi:10.1002/2014JA020188.

Selesnick, R. S., Y.-J. Su, and J. B. Blake (2016), Control of the innermost electron radiation belt by large-scale electric fields, J. Geophys. Res. Space Physics, 121, doi:10.1002/2016JA022973.

Sergeev, V. A., I. A. Chernyaev, S. V. Dubyagin, Y. Miyashita, V. Angelopoulos, P. D. Boakes, R. Nakamura, and M. G. Henderson (2012), Energetic particle injections to geostationary orbit: Relationship to flow bursts and magnetospheric state, J. Geophys. Res., 117, A10207, doi:10.1029/2012JA017773.

Shprits, Y. Y., D. A. Subbotin, N. P. Meredith, and S. R. Elkington (2008), Review of modeling of losses and sources of relativistic electrons in the outer radiation belt II: Local acceleration and loss, J. Atmos. Sol. Terr. Phys., 70(14), 1694–1713, doi:10.1016/j.jastp.2008.06.014.

Smiddy, M., M. C. Kelley, W. Burke, F. Rich, R. Sagalyn, B. Shuman, R. Hays, and S. Lai (1977), Intense poleward-directed electric fields near the ionospheric projection of the plasmapause, Geophys. Res. Lett., 4, 543–546, doi:10.1029/GL004i011p00543.

Smith, P., and R. A. Hoffman (1974), Direct observations in the dusk hours of the characteristics of the storm time ring current particles during the beginning of magnetic storms, J. Geophys. Res., 79, 966-971, doi:10.1029/JA079i007p00966.

Southwood, D. J., and R. A. Wolf (1978), An assessment of the role of precipitation in magnetospheric convection, J. Geophys. Res., 83, 5227–5232, doi:10.1029/JA083iA11p05227.

Spiro, R. W., R. A. Heelis, and W. B. Hanson (1979), Rapid subauroral ion drifts observed by Atmosphere Explorer C, Geophys. Res. Lett., 6, 657–660, doi:10.1029/GL006i008p00657.

Stern, D. P. (1977), Large-scale electric fields in the Earth's magnetosphere, Rev. Geophys., 15, 156–194, doi:10.1029/RG015i002p00156.Walsh, B. M., J. C. Foster, P. J. Erickson, and D. G. Sibeck (2014), Simultaneous ground- and space-based observations of the plasmaspheric plume and reconnection, Science, 343, 1122–1125.

Su, Y.-J., R. S. Selesnick, and J. B. Blake (2016), Formation of the inner electron radiation belt by enhanced large-scale electric fields, J. Geophys. Res. Space Physics, 121, doi:10.1002/2016JA022881.

Thaller, S. A., et al. (2015), Van Allen Probes investigation of the large-scale duskward electric field and its role in ring current formation and plasmasphere erosion in the 1 June 2013 storm, J. Geophys. Res. Space Physics, 120, doi:10.1002/2014JA020875.

Thorne, R. M., Y. Y. Shprits, N. P. Meredith, R. B. Horne, W. Li, and L. R. Lyons (2007), Refilling of the slot region between the inner and outer electron radiation belts during geomagnetic storms, J. Geophys. Res., 112, A06203, doi:10.1029/2006JA012176.

Thorne, R. M. (2010), Radiation belt dynamics: The importance of wave-particle interactions, Geophys. Res. Lett., 37, L22107, doi:10.1029/2010GL044990.

Thorne, R. M., et al. (2013), Rapid local acceleration of relativistic radiation belt electrons by magnetospheric chorus, Nature, 504, 411–414, doi:10.1038/nature12889.

Tsyganenko, N. A., and M. I. Sitnov (2005), Modeling the dynamics of the inner magnetosphere during strong geomagnetic storms, J. Geophys. Res., 110, A03208, doi:10.1029/2004JA010798.

Turner, D. L., et al. (2014), On the cause and extent of outer radiation belt losses during the 30 September 2012 dropout event, J. Geophys. Res. Space Physics, 119, 1530–1540, doi:10.1002/2013JA019446.

Turner, D. L., et al. (2015), Energetic electron injections deep into the inner magnetosphere associated with substorm activity, Geophys. Res. Lett., 42, 2079–2087, doi:10.1002/2015GL063225.

Van Allen Probes website, http://www.nasa.gov/sites/default/files/styles/full_width_feature/public/images/730056main_20130228-radiationbelts-orig_full.jpg?itok=2Uc5iovu

Volland, H. (1973), A semiempirical model of large-scale magnetospheric electric fields, J. Geophys. Res., 78, 171–180, doi:10.1029/JA078i001p00171.

Walsh, B. M., J. C. Foster, P. J. Erickson, and D. G. Sibeck (2014), Simultaneous ground- and space-based observations of the plasmaspheric plume and reconnection, Science, 343, 1122–1125.

Wolf, R. A., R. W. Spiro, S. Sazykin, and F. R. Toffoletto (2007), How the Earth's inner magnetosphere works: An evolving picture, J. Atmos. Sol. Terr. Phys., 69, 288–302.

Wygant, J., et al. (2013), The electric field and waves instruments on the radiation belt storm probes mission, Space Sci. Rev., 179(1–4), 183–220, doi:10.1007/s11214-013-0013-7.

Yang, J., F. R. Toffoletto, R. A. Wolf, and S. Sazykin (2015), On the contribution of plasma sheet bubbles to the storm time ring current, J. Geophys. Res. Space Physics, 120, doi:10.1002/2015JA021398.

Yeh, H.-C., J. C. Foster, F. J. Rich, and W. Swider (1991), Storm time electric field penetration observed at mid-latitude, J. Geophys. Res., 96(A4), 5707–5721, doi:10.1029/90JA02751.

Zhang, J., et al. (2007), Solar and interplanetary sources of major geomagnetic storms (Dst ≤ -100 nT) during 1996–2005, J. Geophys. Res., 112, A10102, doi:10.1029/2007JA012321.

Zhao, H., X. Li, J. B. Blake, J. F. Fennell, S. G. Claudepierre, D. N. Baker, A. N. Jaynes, and D. M. Malaspina (2014), Characteristics of pitch angle distributions of hundreds of keV electrons in the slot region and inner radiation belt, J. Geophys. Res. Space Physics, 119, 9543–9557, doi:10.1002/2014JA020386.

Zhao, H., et al. (2015), The evolution of ring current ion energy density and energy content during geomagnetic storms based on Van Allen Probes measurements, J. Geophys. Res. Space Physics, 120, 7493–7511, doi:10.1002/2015JA021533.